Rapid vapor deposition of micrometer-thick silicon-base porous anodes for lithium secondary batteries

博士論文

Rapid vapor deposition of micrometer-thick silicon-base porous anodes for lithium secondary batteries

(リチウム二次電池に向けたマイクロメータ厚さのシリコン系多孔質負極の急速蒸着技術の開発)

Jungho LEE

李　重昊

A thesis presented in partial fulfilment of

the requirements for the degree of

DOCTOR OF PHILASOPHY

東京大学大学院工学系研究科化学システム工学専攻

Department of Chemical System Engineering

The University of Tokyo

April 2015

Rapid vapor deposition of micrometer-thick silicon-base porous anodes for lithium secondary batteries

(リチウム二次電池に向けたマイクロメータ厚さのシリコン系多孔質負極の急速蒸着技術の開発)

By Jungho LEE

李　重昊

A thesis presented in partial fulfilment of

the requirements for the degree of

DOCTOR OF PHILASOPHY

東京大学大学院工学系研究科化学システム工学専攻

Department of Chemical System Engineering

The University of Tokyo

April 2015

*This thesis entitled "Rapid vapor deposition of micromter-thick silicon-base porous anodes for lithium secondary batteries," submitted by **Jungho Lee**, is approved by the members of this committee:*

Yukio Yamaguchi, Professor

Thesis Advisor
Department of Chemical System Engineering
The University of Tokyo

Suguru Noda, Professor

Thesis Advisor and Committee Member
Department of Applied Chemistry
Waseda University

Atsuo Yamada, Professor

Committee Chair
Department of Chemical System Engineering
The University of Tokyo

Kazunari Domen, Professor

Committee Member
Department of Chemical System Engineering
The University of Tokyo

Yoshiko Tsuji, Associate Professor

Committee Member
Environmental Science Center
The University of Tokyo

Masashi Okubo, Associate Professor

Committee Member
Department of Chemical System Engineering
The University of Tokyo

Toshiyuki Momma, Professor

Committee Member
Department of Applied Chemistry
Waseda University

I understand that my thesis will become part of the permanent collection of The University of Tokyo Library. My signature below authorizes release of my thesis to any reader upon request.

Jungho Lee, Author

Dedication

This thesis is dedicated to all my dearly beloved family.

For their endless love, support and encouragement

Content

Chapter 1 – Introduction

1.1 Electrical energy storage

Over the past decades, current manufacturing and transportation activities has been derived from the discovery and exploitation of primary fossil fuels, such as coals, oils and natural gases. The Energy Information Administration (EIA) recently reported that world's energy consumption will increase by 56% between 2010 and 2040, from 524 quadrillion British thermal units (Btu) to 820 quadrillion Btu [1]. However, global warming, caused by CO_2 emission of burning carbonaceous fuels, and exhaustion of resources have demanded alternative renewable energies like solar and wind power [2-4]. The development of new renewable resources, such as wind and solar power, brought out the research of energy storage because they inherently fluctuate over time [5]. Moreover, new technologies for suppressing emission of CO_2, offer a huge potential of commercializing plug-in-hybrid electric vehicles (PHEV) and electric vehicles (EVs) as new transportation methods [6-8], together with energy storage system (ESS) [9]. Electrochemical energy storage in the form of batteries is fundamental in those energy systems and devices, used as not only national electric smart grids [10], but also the power source from portable devices to medical and aerospace applications. Batteries and electrochemical capacitors are representative of common electrical energy storages in meeting growing electricity demand in large scale market [11, 12]. Among them, the electrochemical capacitors, also known as ultracapacitors, with high specific power, long cycle stability and life time

can be a good choice for applications [13], but suffer from low specific energy [14, 15]. In contrast, batteries with high energy densities attract public attention of realizing a global electric transportation industry due to their great specific energy in spite of low specific power and cycle degradation issues [16, 17]. Therefore, improvement of energy and power densities of batteries for long cycles with low cost is needed for penetration into the global market.

1.2 Rechargeable batteries

A rechargeable battery, also called secondary battery, is a type of batteries, which consists of one or more electrochemical cells operating reversible electrochemical reactions. The first electrochemical cell was discovered by Alessandro Volta in 1800. He repeated and checked Galvani's experiment using dead frogs' legs [18], and demonstrated that electrical energy was derived from spontaneous redox reaction occurring on two different metals, zinc and copper, dipped in an acidic electrolyte. The discovery brought about innovation of development of rechargeable batteries, composed of lead-acid with aqueous electrolytes in 1859, and nickel-cadmium in a potassium hydroxide solution, known as first alkaline battery, was invented by Waldemar Jungner in 1899, and further Thomas Edison patented nickel-iron battery design in 1903. He also tried to commercialize electric vehicles, but the era of electric car came to an end soon because of short battery life and appearance of inexpensive gasoline automobiles [19]. However, his achievements were followed about a century later by introducing first commercial hybrid-electric vehicle (HEV, Prius, Toyota, Aichi, Japan) in 1989, which uses nickel-metal hydride batteries (NH-MH; nickel oxyhydroxide (NiOOH) as cathode and hydrogen-absorbing alloy (MH) as anode) [20]. Moreover, two sodium-base batteries, operated at high temperature, were developed for meeting higher voltage and energy densities in 1970s, but were at a risk of safety concern, and thus limited stationary energy storages [21, 22]. On the other hand, it was reported that the lithium metal would be theoretical ideal material for batteries due to the

highest specific capacity per weight and the highest oxidation electrochemical potential of all known elements, and rechargeable lithium batteries was firstly introduced by G.N. Lewis in 1912, followed by launching first generation Lithium ion batteries (LiBs) by Sony corporation (Tokyo, Japan) in 1991[23]. Figure 1-1 shows that LiBs offer high energy and power densities among various batteries. LiBs have a good balance among the energy density, long cycle life, and stability, thus are promising cell for electric devices [24].

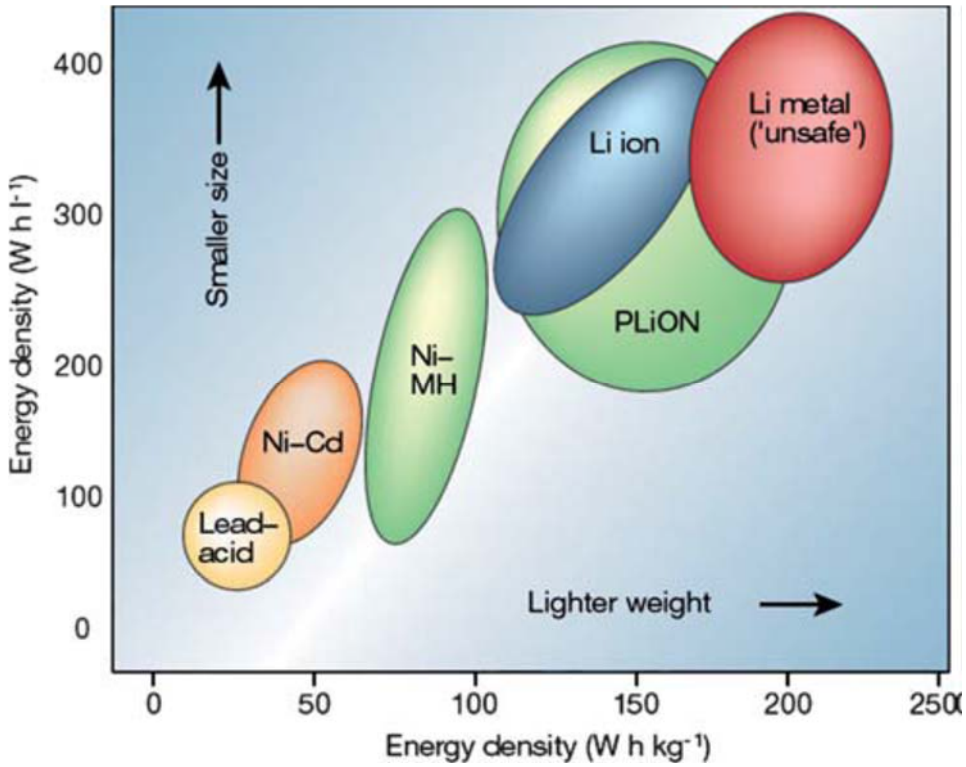

Figure 1-1 Comparison of the different type of batteries in terms of volumetric and gravimetric energy density. Currently, the market share of Ni-Cd, Ni-MH and LiBs is 23, 14 and 63%, respectively *[24].

* Reprinted from Nature, 414, M. Tarascon and M. Armand, Issues and challenges facing rechargeable lithium batteries, 2001, Copyright (2001), with permission from Nature Publishing Group (see Appendix).

1.3 Lithium ion batteries (LiBs)

1.3.1 Fundamentals of LiBs

Lithium ion batteries (LiBs) are one of the rechargeable batteries, base in redox reaction including the intercalation of lithium ions between the cathode and anode as shown in Figure 1-2 [25]. The performance of LiBs can be determined by energy storage density, lithium ion diffusion rate and cycle ability. Energy storage density of LiBs, E, is proportional to the lithium ion storage capacity, C and the difference of electrochemical potential, V, as below [26];

$$E = \int CV \tag{1-1}$$

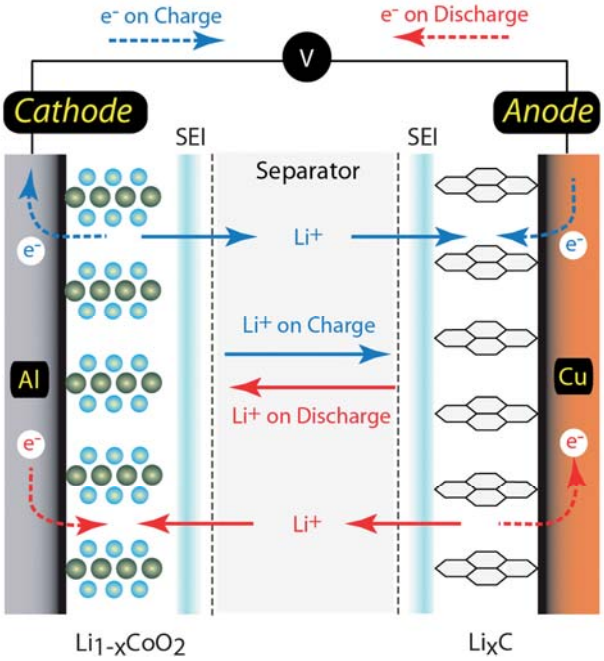

Figure 1-2 Schematic illustration of charge/discharge reaction mechanisms in a conventional lithium ion battery between lithium metal oxide as cathode and graphite as anode. Electron and Li^+ transport during charge/discharge was stated by blue and red arrows, respectively. The electrons travel through the external circuit *[25].

* Reprinted from Energy & Environmental Science, 2, B. J. Landi, M. J. Ganter, C. D. Cress, R. A. DiLeo and R. P. Raffaelle, Carbon nanotubes for lithium ion batteries, 2009, Copyright (2009), with permission from Royal Society of Chemistry (see Appendix)

From the equation (1-1), it is clear that high energy storage density can be achieved by either increasing storage capacity or electrochemical potential difference of electrodes, which demands developing next generation electrode materials. Electrochemical potential as a function of storage capacities of Li-base cells is plotted in Figure 1-3 [25]. The anode materials have been explored having a wide range of theoretical capacities depending on materials from conventional Li^+ intercalated graphite LiC_6 of ~372 mAh g^{-1} to silicon of ~4200 mAh g^{-1}, while the highest capacity of oxides cathode materials is below 500 mAh g^{-1}. Therefore, new generation LiBs with enhanced energy density demand more research effort of the cathode compounds mixture as well as practical use of anode materials with high theoretical capacities. Rate capability of LiBs can also be achieved

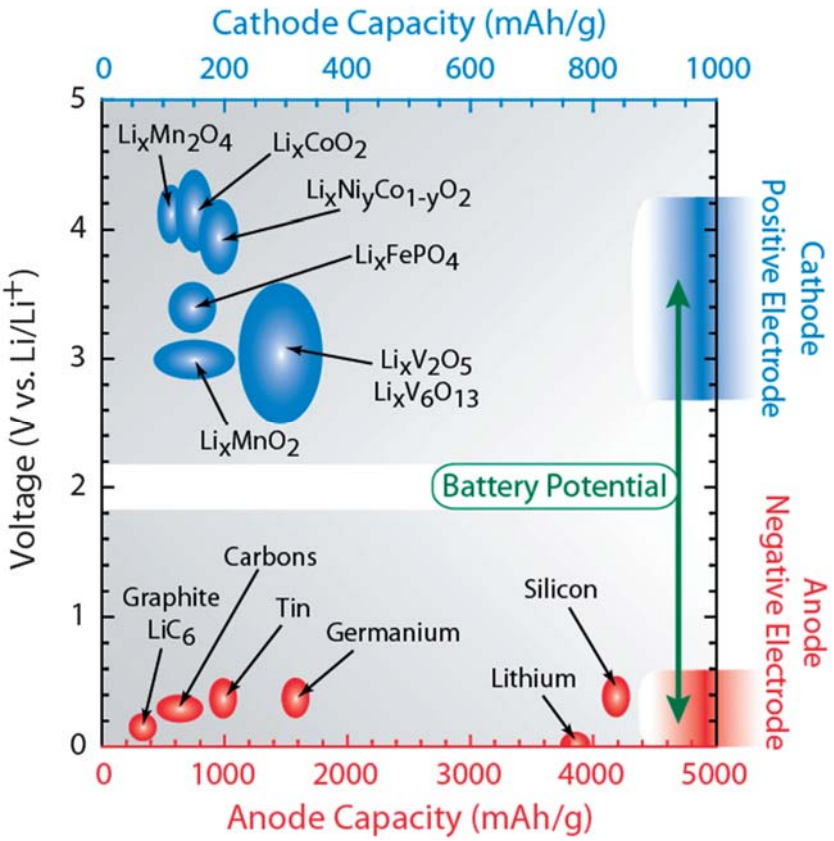

Figure 1-3 Schematic illustration of electrochemical potentials of conventional cathode (blue) and anode (red) as a function of storage capacities presently used for under consideration of Li-based cells *[25].

* Reprinted from Energy & Environmental Science, 2, B. J. Landi, M. J. Ganter, C. D. Cress, R. A. DiLeo and R. P. Raffaelle, Carbon nanotubes for lithium ion batteries, 2009, Copyright (2009), with permission from Royal Society of Chemistry (see Appendix).

by increasing lithium ion diffusion rate to electrode during intercalation process, corresponding with conductivity and structure of electrodes [27, 28]. And cycle ability is also highly connected with the structure of electrode material because lithium intercalation process accompanies with a huge volume change, which motivated researchers to study various micro- and nano-structures for electrodes.

1.3.2 Current status of LiBs

The breakthrough in lithium ion battery technology is that lithium metal with safety concern as an anode was substituted by graphite, which accommodates one lithium per three C_6 hexagons, and formed LiC_6 without forming dendrite. The discovery of $LiCoO_2$ [29, 30] as a cathode and stable liquid organic carbonate solvent enabled the reversible operation at high voltage of ~4.2 V by Sony corporation in 1991 [23]. More recently, several cathode materials, such as $LiNiO_2$, $LiMnO_2$ [31], spinel $LiMn_2O_4$ [32] and $LiFePO_4$ [33], have been investigated, but even though individual advantages, such as improved safety, reduced cost, and enhanced power density, the energy density has not been improved compared with $LiCoO_2$ yet. The chemical reaction of typical $LiCoO_2$ cathodes is described as below;

$$LiCoO_2 \leftrightarrow Li_{1-x}CoO_2 + xLi^+ + xe^- \quad (1\text{-}2)$$

In case of the anode material, the various carbonaceous materials with a low potential versus lithium were introduced, and graphite, carbon fibers and mesocarbon microbeads (MCMB) were a commercial success in LiBs market [34]. Graphite provides several advantages in the view point of cost, abundance, non-toxicity and structural stability for repeated cycles [35]. In addition, lithium intercalation to graphite causes small volume change (9–10%), with the typical reaction expressed as;

$$6C + xLi^+ + xe^- \leftrightarrow Li_xC_6 \quad (x \le 1) \quad (1\text{-}3)$$

However, graphite anodes possess the disadvantages of low capacity (~375 mAh g^{-1}) with a maximum configuration of one lithium atom to every six carbon atoms of LiC_6 and safety issues related to Li deposition [36, 37], which has limited its feasibility meeting with the growing demand in high power technology for electric vehicles (EVs) or hybrid electric vehicles (HEVs). Moreover, a low operating voltage around 100 mV (vs. Li^+/Li) causes the reaction of graphite with electrolyte, resulting in reducing battery performances as well as serious safety concerns such as thermal runaway.

Carbonaceous materials have been extensively researched, such as one-dimensional (1-D), two-dimensional (2-D) and porous carbon, trying to create more surface areas for lithium storage and to increase the energy and power densities [38]. One-dimensional structured carbon materials were well known as carbon nanotubes (CNTs) and carbon nanofibers (CNFs). The anode of CNTs achieved ~1116 mAh g^{-1} of reversible capacity using various treatments, such as ball-milling [39], acid oxidation [16], and metal oxide cutting [40], while the reversible capacities of CNFs-anodes by electrospinning/carbonization process combined with chemical treatments was found to be ~430 mAh g^{-1} at 50 mA g^{-1}.[41-43]

Graphene, on the other hand, is representative 2-D structured carbonaceous material with high surface area including electrical and thermal conductivity. Graphene or graphene-base composited material with active metal (Sn [44], Sn-Sb [45] and Si [46]) and/or metal oxide (Co_3O_4 [47, 48], TiO_2 [49], Fe_3O_4 [50, 51], Mn_3O_4 [52], CuO [53] and SnO_2 [54, 55]) has been researched. The graphene as anode material was currently reported having ~500 mAh g^{-1} after 30 cycles [56], and SnO_2/graphene anodes showed more enhanced performance high reversible capacity of ~800 mAh g^{-1} at 50mA g^{-1}, and ~570 mAh g^{-1} after 30 cycles with 70% capacity retention, while high irreversible capacity and unstable performance still existed [57], which needs to further researches. Meso-porous carbon anodes with different pore sizes from nano- to micro-scale have been also researched with advantages of suppressing volume change by high surface area, which achieved reversible capacity of ~800 mAh

g^{-1} at 100 mA g^{-1} after 20 cycles because of minimized ion transport resistance around the pores with ordered porous structures [58, 59].

In summary, carbonaceous anode materials with different nanostructure, such as 1-D, 2-D and ordered porous carbon) exhibited a good electrochemical performance with individual their advantages, but poor rate performance (except for graphene), low volumetric energy density by SEI, and low capacity was still in common challenge for practical usage suitable for high-powered-applications.

1.4 Silicon (Si) anodes in LiBs

1.4.1 Advantages of Si for anode material

Silicon (Si) has been currently considered to be a promising anode material, substituted for conventional carbonaceous materials like graphite, and thus probably most studied anode material. Silicon exhibits low lithiation potential (*vs*. Li/Li^+) below ~300 mV, which makes it relatively stable and safe as an anode material compared to graphite with a high energy density material (up to 120

Table 1-1 Different properties of various anode materials (Th. Sp. Cap. Indicated theoretical specific capacity) [64]

Materials	Li	C	$Li_4Ti_5O_{12}$	Si	Sn	Sb	Al	Mg
Density (g cm^{-3})	0.53	2.25	3.5	2.3	7.3	6.7	2.7	1.3
Lithiated phase	Li	LiC_6	$Li_7Ti_5O_{12}$	$Li_{4.4}Si$	$Li_{4.4}Sn$	Li_3Sb	LiAl	Li_3Mg
Th.Sp.Cap. (mAh g^{-1})	3862	372	175	4200	994	660	993	3350
Volume change (%)	100	12	1	420	260	200	96	100
Potential *vs.* Li (V)	0	0.05	1.6	0.4	0.6	0.9	0.3	0.2

Wh kg^{-1} [60]), Besides, Si can accommodate up to 4.4 lithium ions per unit (the stoichiometry of the lithiated to $Li_{4.4}Si$ alloy), corresponding with the highest theoretical gravimetric capacity of 4200 mAh g^{-1}, which is ten times larger than that of conventional graphite [61-63], and high volumetric capacity of 9786 mAh cm^{-3}, derived from the calculation on the initial volume of Si [64]. Because of this, Si anodes possess an enough potential to apply high-powered storage system, such as electric vehicles (EVs). In addition, Si is abundant material on earth with a low cost and environment-friendly, and thus has been used for semiconductor devices, and also the delithiation potential of Si occurs at a relatively low voltage of ~0.4 V [65], as shown in Table 1-1 [64]. When lithium is inserted into Si anode, Si experiences a series of phase transformations from electrochemical lithiation/delithiation

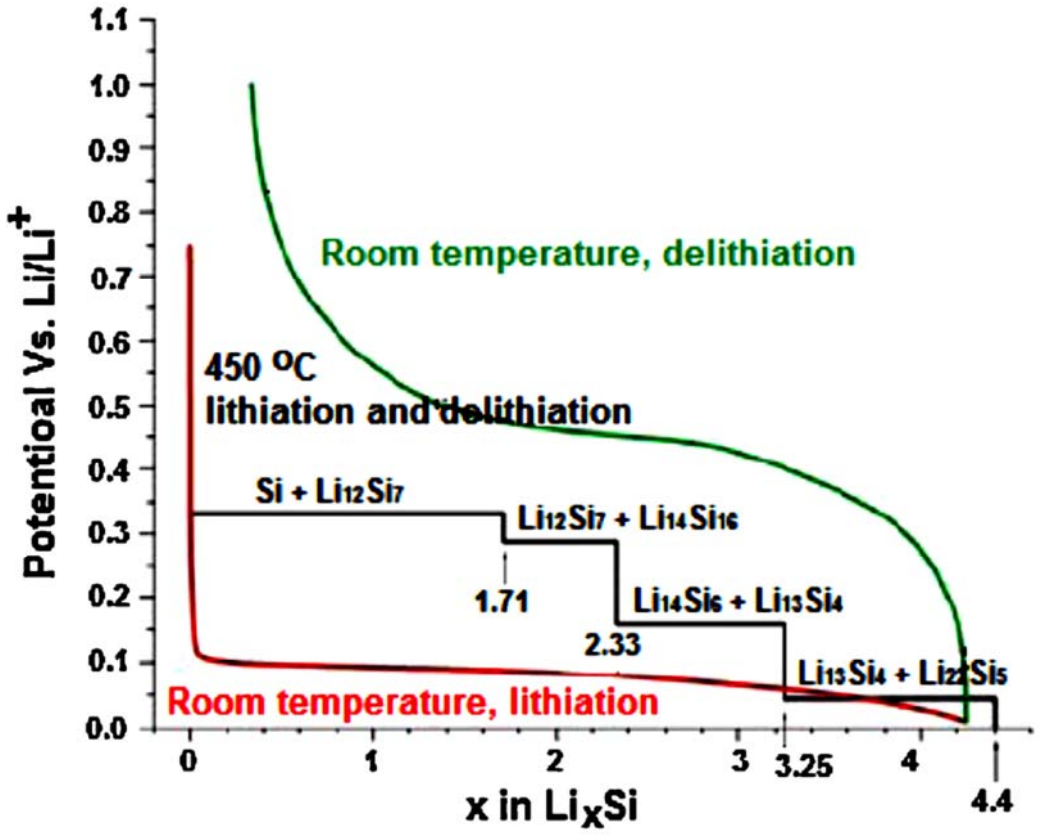

Figure 1-4 Electrochemical lithiation/delithiation curves of Si anodes at high temperature of 450 °C and room temperature. Multiple step curves (black) indicated at 450 °C, while lithiation/delithiation of crystalline Si at room temperature is plotted, as red and green line, respectively *[64].

* Reprinted from Nano Today, 7, H. Wu and Y. Cui, Designing nanostructured Si anodes for high energy lithium ion batteries, 2012, Copyright (2012), with permission from Elsevier (see Appendix).

diagram of Si, as shown in Figure 1-4 [64], which is reported multiple step curve of voltage plateau at high temperature of 450 °C [65], but crystalline Si (cr-Si) transformed into amorphous phase, and further amorphous or crystalline lithium silicide phase depending on lithiated potential at initial lithium insertion, while amorphous Si (a-Si) goes through amorphous or crystalline lithium silicide phase at room temperature.

1.4.2 Challenges for Si anodes

As I stated above, Si is more attractive material than any other materials as anode for LiBs. However, this high specific capacity is realized by inserting a large amount of Li^+ into Si materials, which accompanied with large volume change (300–400%, depending on the state of Li_xSi), supported by various microstructural analysis methods, such as X-ray diffraction [66, 67] and nuclear magnetic resonance [68], and subsequently Si electrodes do not withstand the heavy strain of such volumetric expansion and break down, resulting in pulverization and delamination of the whole structure [69-71]. Further capacity losses are caused by solid electrolyte interphase (SEI) formation, while delamination results in loss of electrical contact with the current collector. The fundamental three issues of Si failure phenomena, as an anode for LiBs, were summarized in illustrated Figure 1-5 [64]. The large volume change induces large stress and strain, which causes cracking and pulverization of the Si anode, results in loss of electrical contact. Moreover, such a large volume change causes disconnection of Si nano- or micro-particles in case of nanostructured Si materials or assembled materials of Si nanoparticles. Another issue is the formation of passivating film before lithium insertion to Si at the surface, called to SEI, induced by decomposition of the organic electrolyte because the potential of lithium insertion is lower than reduction potential ≥1 (versus Li/Li^+) of

organic solvent in commercial electrolyte [72], such as ethylene carbonate (EC), propylene carbonate (PC), dimethyl carbonate (DMC), diethyl carbonate (DEC), and so on. The SEI films were reported to consist of lithium carbonate (Li_2O_3), various lithium alkylcarbonates ($ROCO_2Li$), mainly, including Li_2O, LiF or LiCl, and nonconductive polymers [73-78].

Consequently, various approaches based on control of Si-base material structure or composition as well as on the operation control of lithiation/delithiation cutoff voltage, were carried out to accommodate and buffer the effects of volume change. Moreover, conductive materials for enhanced lithium diffusion rate, electrolyte additives for improvement of SEI and polymer binder for enhanced adhesion between electrodes and current collectors have been researched continuously.

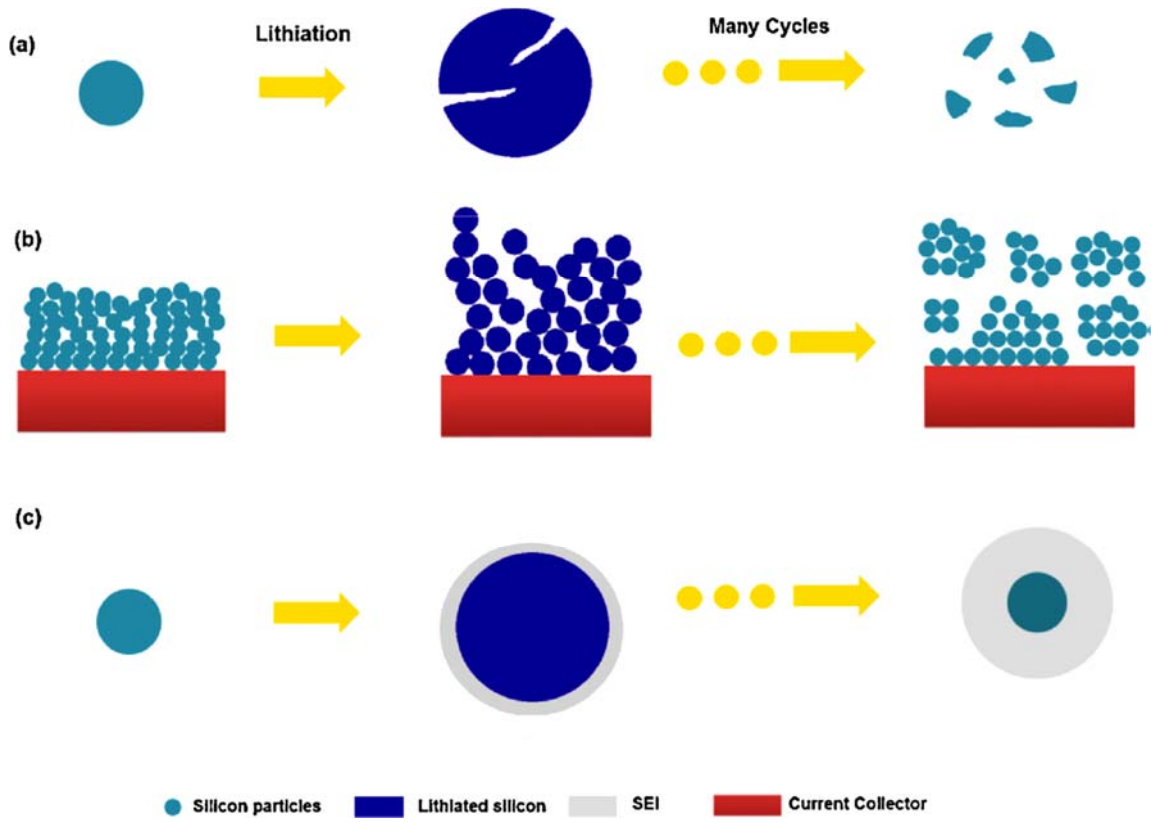

Figure 1-5 Illustration of Si-electrode failure mechanism (a) Material pulverization. (b) Disconncetion of Si nano- and micro-particles. (c) SEI regeneration *[64].

* Reprinted from Nano Today, 7, H. Wu and Y. Cui, Designing nanostructured Si anodes for high energy lithium ion batteries, 2012, Copyright (2012), with permission from Elsevier (see Appendix).

The various structures of Si-base materials, such as thin film, micro-/nano-particles, nanowires (SiNWs), and composite materials of Si with carbon and/or silicides, were introduced and charged issues. One-dimensional SiNWs with various structures, introduced by Yi Cui group [79], were currently charged issues, achieving excellent electrochemical performance for long cycles. They suggested one dimensional structure of SiNWs relax the stress during volume change, and hollow structured double-walled Si nanotubes with outside SiO*x* surface layer also make stronger surface film, resulting in no significant capacity fade [80]. Another issue of Si-base materials is composite of Si with carbon and/or silicides, such as electrodeposited Si-O-C composite film [81, 82] and metal silicide-coated Si films [83], which enhanced electrochemical performance for long cycles because of their unique structure and control of SEI.

1.5 Research scope and objectives

The previously presented studies mainly focused on the electrochemical performance of Si materials, and thus various structures and compositions, focusing on realizing accommodates stresses induced by volume change, were reported. As a result, high gravimetric capacities of Si-base anode materials were achieved successfully, but the weight of heavy current collector was, sometimes, neglected for very thin active layers. Commercialized graphite anode, Sony 18650 cell as currently reported, consists of $LiCoO_2$ as cathode and graphite as anode. The physical properties of the graphite anode of the cell were the mass of 5.7 g, 11 mg cm^{-2} of areal density, 193 μm in thickness (including current collector), and dimensions of the anode is 52.9 × 5.7 cm, and areal capacity is ~4 mAh cm_{anode}^{-2}. Even though theoretical capacity of Si is ten times higher than graphite, the thickness of Si has to approach ~10 μm for practical use in LiBs market, supposing that conventional Cu current collector has ~100 μm in thickenss. However, previously reported Si nanomaterials have still low areal density of ~250–300 μg cm_{anode}^{-2}, showing low areal capacity of 0.2–0.4 mAh cm_{anode}^{-2}, even though high

gravimetric capacity of 4000 mAh g_{si}^{-1}. Furthermore, various fabrication methods of Si anode were reported, such as high-energy mechanical milling as top-down approach, and chemical vapour deposition (CVD), sol-gel synthesis, hydrothermal synthesis and electron-beam deposition (EB) as bottom-up approach. Especially, silane (SiH_4) gas and silicon tetrachloride ($SiCl_4$) have been used as a precursor by CVD and EB method, which was time-consuming process with low yield.

In summary, the researches of various structured Si-base materials have successfully demonstrated the possibility of Si for usage of next generation anode material in LiBs, while further researches are also needed in some respects. The structure design of Si was the most progressive in qualitative level, but quantitative understanding, such as size-dependence of particles and pores, has been still investigated quantitatively. Furthermore, although various approaches were reported to understand and improve of passivating surface film (SEI), high irreversible capacity of Si anodes demands further studies. Finally, the development of large-scale, low-cost fabrication and enhanced mass production for Si materials with desirable electrochemical performance is the most important challenge of all to commercialize Si anode for LiBs.

Chapter 2 – Micrometer-thick porous Si films by rapid vapour deposition (RVD)

2.1 Introduction

The current anode material of commercial LiBs is usually graphite because of its long cycle life, abundance and relatively low cost [84]. However, graphite anodes possess the disadvantages of low capacity (375 mAh g_C^{-1}) and safety issues related to Li deposition [37]. Thus, there has been a growing interest in developing alternative anode materials with low cost, good safety, high energy density and long cycle life. Si is an attractive alloy-type anode material with a theoretical specific capacity (4200 mAh g_{Si}^{-1}) based on the stoichiometry of the alloy $Li_{22}Si_5$ [61-63] . However, this high specific capacity is realized by inserting a large amount of Li^+ into the active material, causing volume expansion of ~300–400%. Si electrodes easily break down by the heavy strain of such volumetric expansion, which triggers pulverization and delamination of the whole structure [69-71], resulting in a loss of electrical contact with the current collector.

To overcome pulverization of electrodes during expansion and shrinkage, many groups, starting with the study by Huggins and coworkers [61], have developed various approaches to control electrode structures, initially thin films [85, 86], micro-particles [87], nanowires [79, 88-91], nanoparticles [92, 93], pillar formation [94], NiSi*x*-Si core-shell nanowires [83], and other structures [95, 96]. Full cells containing cr-Si core-shell nanowires [97] have been reported. High capacities were reported for such

structures; however, sometimes the weight of heavy current collectors was neglected for very thin active layers, and the studies about large-scale, mass production and low-cost fabrication are currently insufficient compared with structure design reports.

In this chapter, I rapidly deposited 3–14 μm-thick porous Si films in 1 min or less by a physical vapour deposition method called rapid vapour deposition (RVD), focusing on developing low-cost fabrication method of Si films with large-scale. Such a high deposition rate is achieved by heating the source Si to 2000–2400 °C, well above its melting point of 1414 °C. Control over the amorphous/crystalline structure, film porosity, structure, surface roughness, and Si/Cu interface is realized by maintaining the temperature of the Cu substrate at 100–500 °C during and after deposition. In particular, control over the roughness of the growing Si films caused by the shadowing effect [98, 99], is important to tailor the film microstructure. The electrochemical behavior of the Si films was investigated by a half-cell test using Li as the counter electrode and discussed in relation to their microstructure.

2.2 Materials and methods

2.2.1 Si film fabrication

Circular Cu plates (15 mm in diameter, 0.5 mm in thickness) instead of thin Cu foils were used as substrates for porous Si films to make the handling (adjusting the size to fit the coin cells) easier. Before Si deposition, the Cu plates were sonicated in isopropanol for 10 min and then exposed to UV-O_3 for 3 min to remove organic contaminants on their surface. Then, the Cu plates were annealed under hydrogen (5 vol% H_2/ Ar, 1 atm) at 800 °C for 10 min to reduce the oxide layer on the Cu surface. Finally, Si was deposited on the Cu substrates by RVD.

Figure 2-1a shows a schematic diagram of the RVD system. The Si source for RVD was prepared by first immersing a Si wafer (CZ p-type, resistivity of 10–20 Ω cm) in 5 wt% hydrogen fluoride (HF) solution for 1 min, and then rinsing it with purified water for 1 min. The wafer was ground into Si powder using mortar and pestle and then loaded into a carbon boat. The Si source was heated by resistive heating of the carbon boat under 0.1 Torr Ar to 2000–2400 °C (boat temperature, T_{boat}) to increase its vapor pressure and thus the deposition rate. A Cu substrate was positioned in the chamber and kept at 100–500 °C (substrate temperature, T_{sub}) during RVD to suppress the surface diffusion of

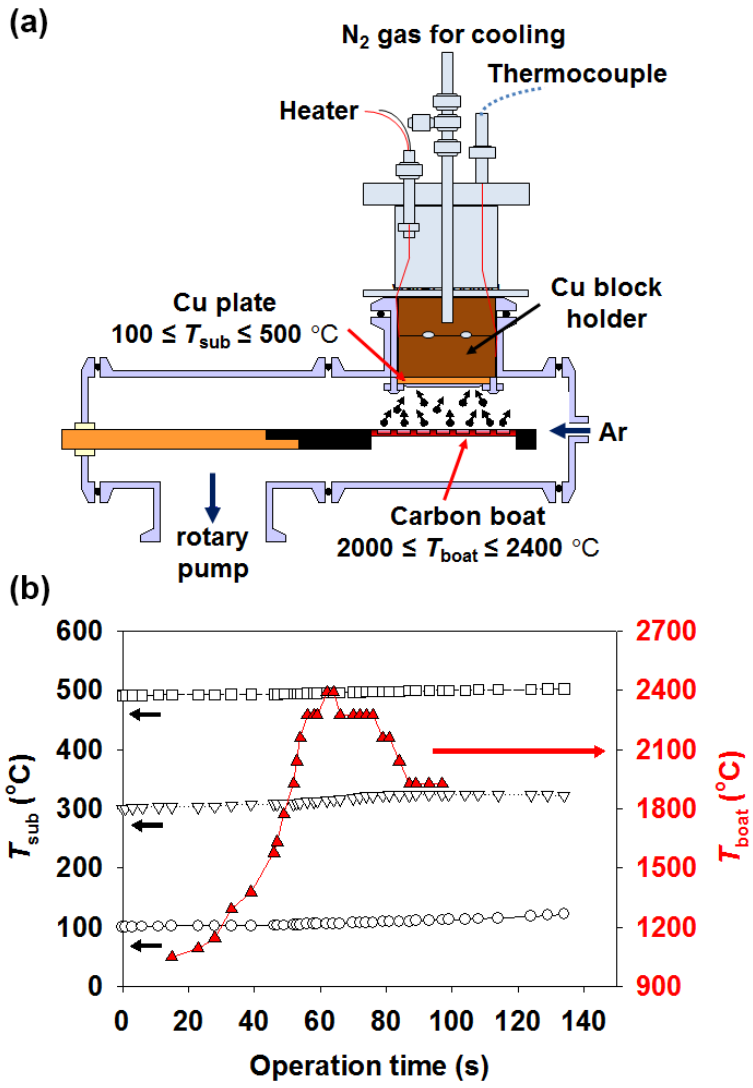

Figure 2-1 (a) Schematic diagram of the RVD system. (b) Typical time profiles of the temperatures of the Si source and Cu plate during RVD at P_{boat} = 1600 W. T_{boat} is shown for a run with T_{sub} = 300 °C and is similar for different T_{sub}.

Si, which induces rough and porous structure in the deposited Si films [83, 98]. To maintain the Cu substrate at constant temperature under the strong thermal radiation from the Si source, we designed a substrate holder made of a block of Cu with a large heat capacity that contained an embedded ceramic heater and cooling line for N_2 gas. After removing the sample from the RVD system, some of the samples were further annealed under 4 vol% H_2/Ar at ambient pressure at 200–600 °C (annealing temperature, T_{an}) for 10 min to form a copper silicide ($CuSi_x$) intermixed layer to improve the adhesion between the Cu substrate and Si film.

Figure 2-1b shows temperature profiles of the Si source and Cu substrate as a function of operation time during deposition. The boat heating power, P_{boat}, was increased manually, and when the source temperature was well above the melting point of Si, deposition began and was then completed after about 1 min. Because of the Cu block holder, the substrate temperature was able to be held at 100, 300 or 500 °C as desired (Figure 2-1b). Before and after Si deposition, each sample was weighed by a microbalance with a sensitivity and precision of 10 μg. Effective thickness t_{eff} was calculated using a value of 2.33 g cm^{-3} for bulk Si crystal. By changing the substrate temperature, a series of Si films with different morphology and electrochemical performance were fabricated.

2.2.2 Characterization

X-ray photoelectron spectroscopy (XPS; JPS9010 TR; JEOL, Akishima, Japan) with a monochromatised Mg Kα X-ray source was used to investigate the surface condition of treated and untreated Cu substrates. Microstructural analysis of the fabricated Si films was carried out using X-ray diffraction (XRD; ATX-G; Rigaku, Akishima, Japan) and laser micro-Raman spectroscopy (HR-800; Horiba, Kyoto, Japan). The microstructure and composition distribution of the Si/Cu samples were analyzed by scanning electron microscopy (SEM; S-4800; Hitachi, Tokyo, Japan) with energy-

dispersive X-ray spectroscopy (EDS, EDAX Genesis; AMETEK, Elancourt, France).

2.2.3 Electrochemical characterization

Capacity and cycle performance measurements were performed by collaborative researchers, Mr. Kenji Nakane and Mr. Shingo Matsumoto at Sumitomo Chemical Co. Ltd., using the Si films on Cu substrates as a working electrode with Li metal (0.5-mm-thick foil) as the counter electrode for R2032-type coin-shaped half cells. $LiPF_6$ solution (1 M) in a 1:1:1 (v/v) mixture of ethylene carbonate (EC), dimethyl carbonate (DMC), and ethyl methyl carbonate (EMC) was used as the electrolyte. Half-cell tests were carried out in the range from 0.005 to 1.000, 1.5000 or 2.000 V *vs.* Li/Li^+ with different charge rates of 0.05*C*–0.2*C* at a constant temperature of 25 °C. *C*-rate was determined using the weight of Si and a theoretical capacity of 4200 mAh g_{Si}^{-1}. After different numbers of cycles, electrochemical impedance spectroscopy (EIS) measurements were performed using a Solartron®1287 electrochemical interface coupled to a Solartron®1260 frequency response analyzer (Ametek, Elancourt, France) in the 10^6 to 10^{-2} Hz frequency range.

2.3 Structure on Si film deposited on Cu substrate by RVD

Figure 2-2a shows a top-view SEM image of an as-purchased Cu plate, which clearly contains lines patterned at intervals of about 2 μm on its surface. Figure 2-2b and c show top-view and cross-sectional SEM images of a 14-μm-thick Si film deposited on a Cu substrate. The Si film contained

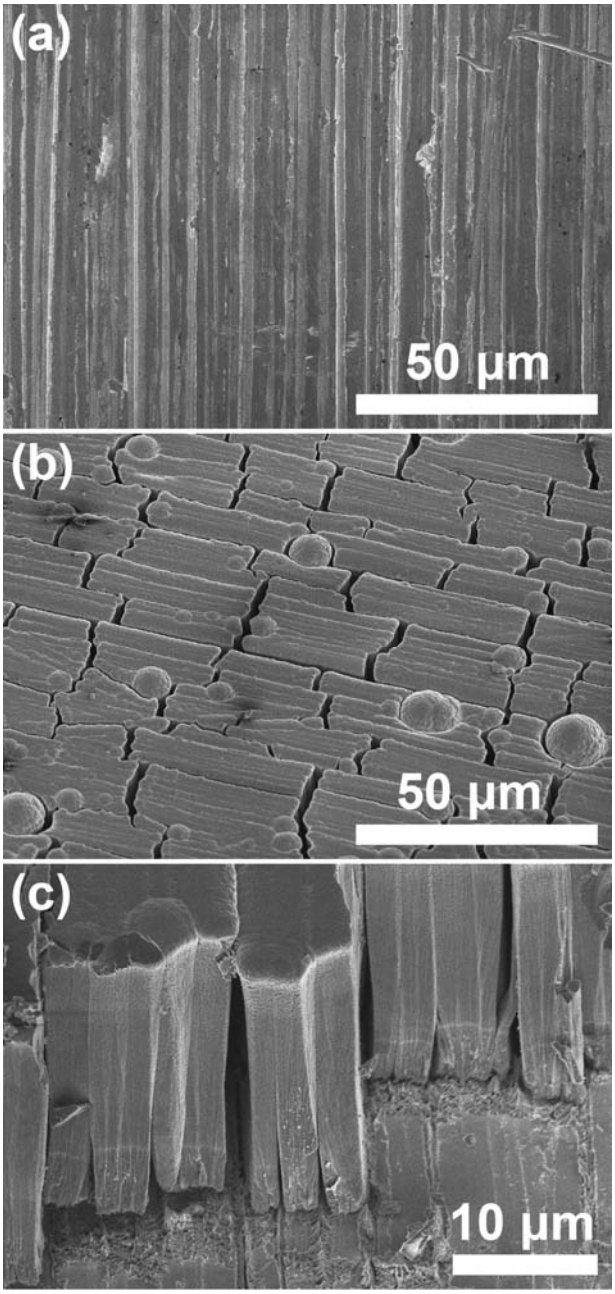

Figure 2-2 (a) A top-view SEM image of an as-purchased Cu plate. (b) Top-view and (c) tilted-view SEM images of a typical Si film (t_{act} = 14 μm) prepared by RVD in 10 s at a high P_{boat} of 1600 W.

many 2-μm-thick stripes that were aligned in one direction. It is clear that the striped structure originates from the line patterns of the as-purchased Cu plates. The Si film also contained cracks in the in-plane and vertical directions to the alignment of the stripes. These cracks were at rather random positions but appeared at intervals of around 20 μm. The surface of the Si film formed with a high P_{boat} of 1600 W contained numerous protrusions with a height of a few μm. If the source heating power was too high, although Si deposition occurred within 10 s, it caused the Si source to boil and spread Si droplets on the Cu substrate, resulting in protrusions in the Si film (Figure 2-3a and c). The cycle performance of such films was very poor regardless of T_{an} for post-annealing treatment; maximum initial charge and discharge capacities were ~2000 and ~600 mAh g_{Si}^{-1}, respectively, and

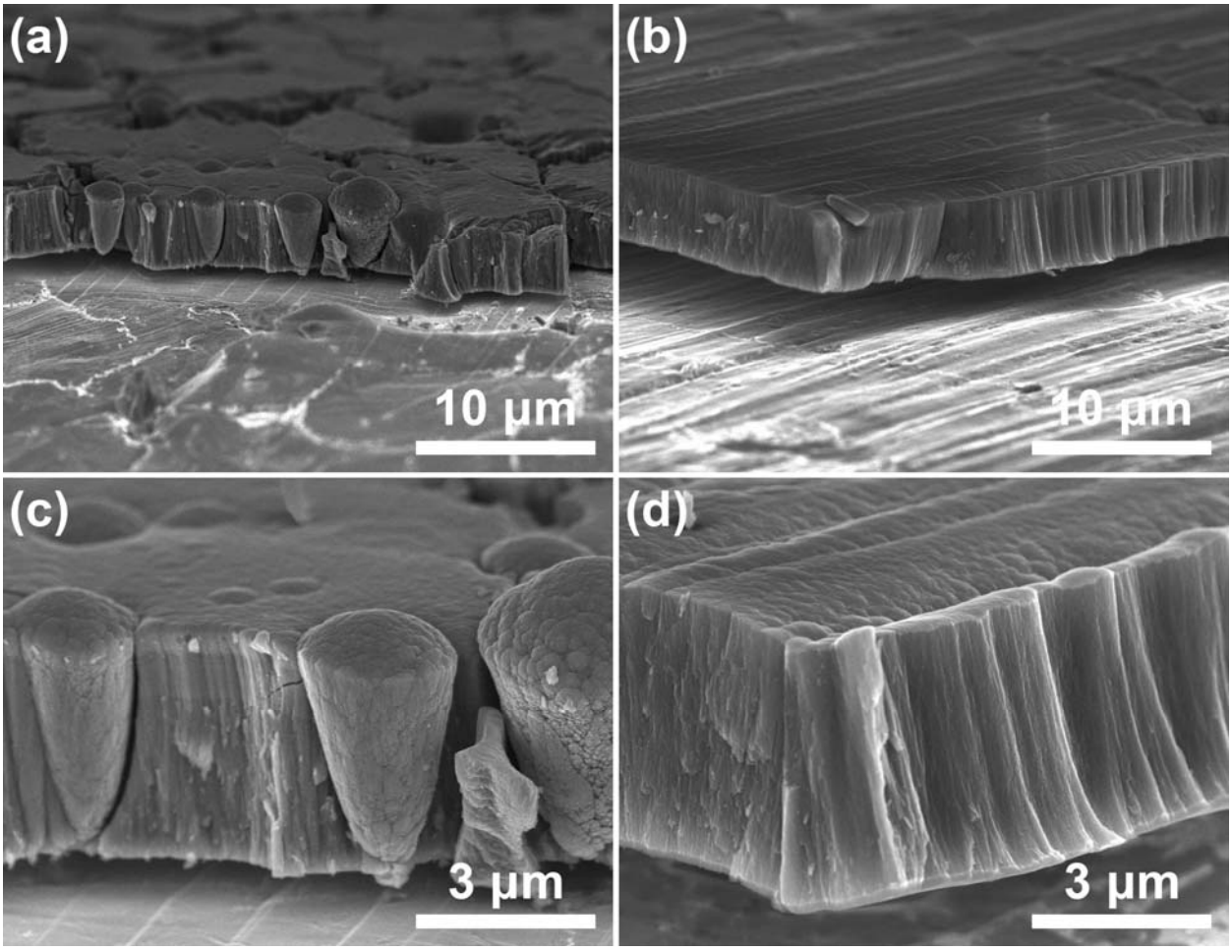

Figure 2-3 Low-magnification cross-sectional SEM images of Si films (t_{act} = 3–5 μm) deposited with (a) high P_{boat} of 1600 W and (b) moderate P_{boat} of 1300 W. (c, d) High-magnification cross-sectional SEM images of (a) and (b), respectively.

capacity decreased within a few cycles (Figure 2-4). At a moderate P_{boat} of 1300 W, porous Si films without protrusions were formed although the deposition time was a little longer (1 min) (Figure 2-3b and d). The weight of Si deposited at P_{boat} = 1300 W was about 1 mg on average for a circular film with a diameter of 14 mm. This areal weight (0.6–0.7 g cm^{-2}) corresponds to t_{eff} ~ 3 μm if the film has the same mass density as bulk crystalline Si (2.33 g cm^{-3}), and the actual thickness t_{act} is larger because of the porous structure of the film. Such films were showed some improvement of cycle performance compared with those deposited at higher P_{boat}; maximum initial charge and discharge capacities were ~2800 and ~1300 mAh $g\text{-}Si^{-1}$, respectively, but capacity reduced within a few cycles

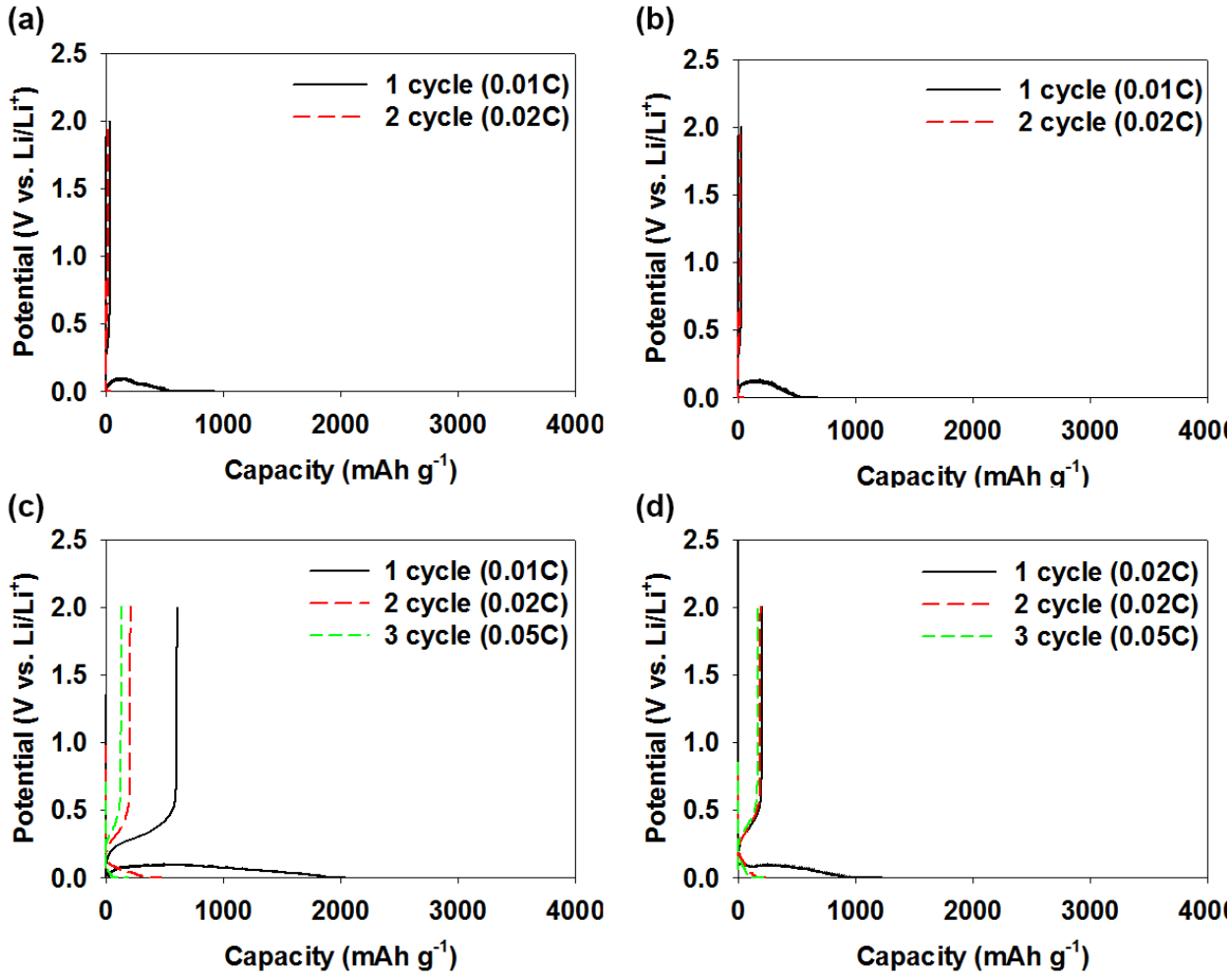

Figure 2-4 Voltage-capacity curves of thick Si films (~10 μm) deposited at high P_{boat} = 1600 W and low T_{sub} = *RT* on as-purchased Cu substrates. (a) An as-deposited Si film, and Si films post-annealed at (b) 200, (c) 400, and (d) 600 °C. Effective Si thicknesses were t_{eff} = (a) 9.6, (b) 11.0, (c) 10.8 and (d) 10.3 μm.

(Figure 2-5). Such rapid capacity fade can be attributed to the insufficient adhesion of the Si films to the Cu substrates, as can be seen in the SEM image (Figure 2-3) that show the Si films detaching from the Cu substrates (note that the cross-sections were prepared by vending the 0.5-mm-thick Cu substrate, resulting in such detachment). Post-annealing treatment was used to improve electrode performance by forming a CuSi*x* intermixed layer to prevent detachment of the Si film from the Cu substrate. Because it is known that solid-state crystallisation of amorphous Si takes about 10 min at 700 °C [100], we annealed the samples for 10 min at T_{an} = 200, 400, and 600 °C to avoid crystallization of the Si films (Figure 2-5b–d). The Si film post-annealed at T_{an} = 600 °C (Figure 2-

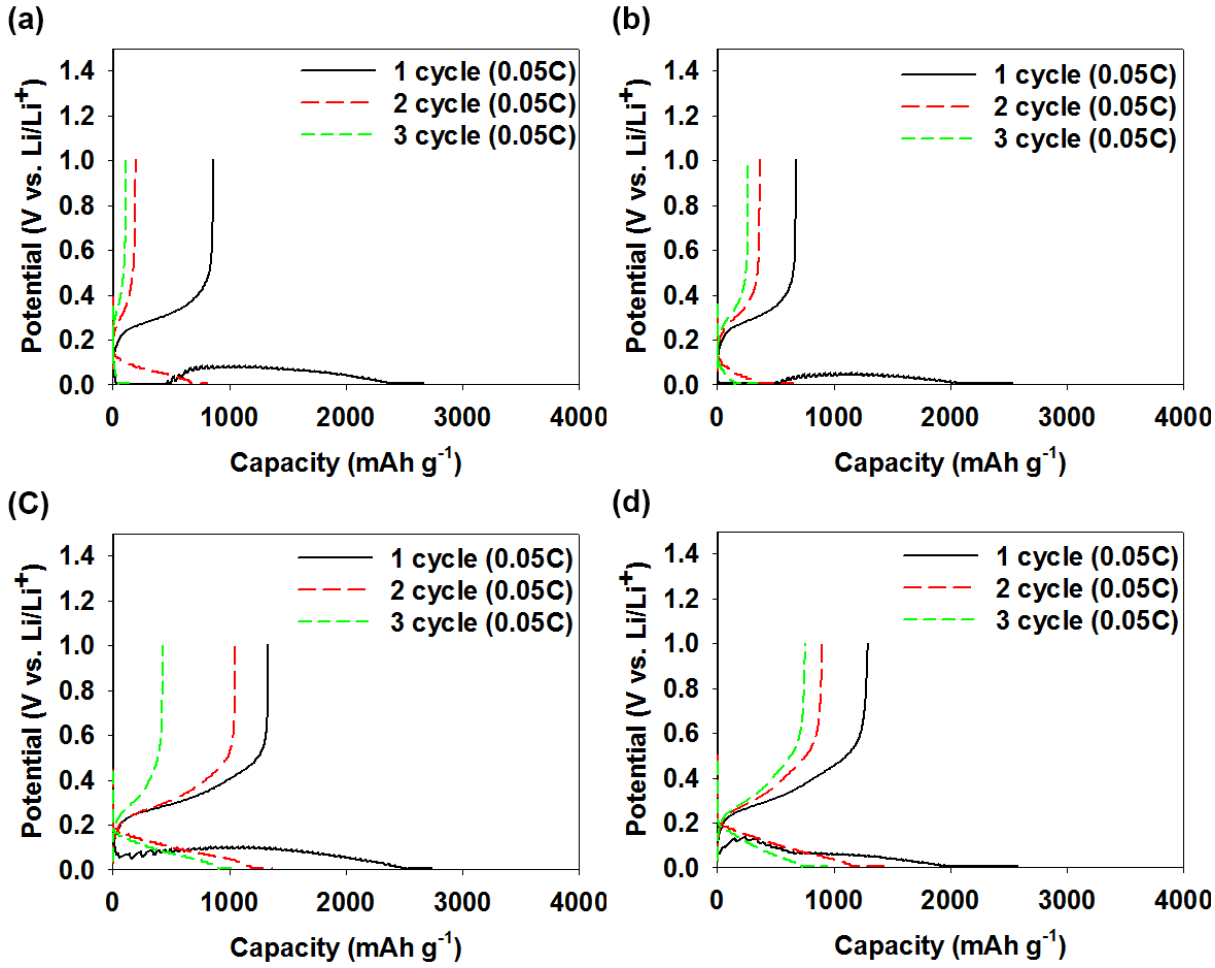

Figure 2-5 Voltage-capacity curves of thick Si films (t_{eff} of ~3 µm) deposited at high P_{boat} = 1300 W and low T_{sub} = *RT* on as-purchased Cu substrates. (a) An as-deposited Si film, and Si films post-annealed at (b) 200, (c) 400, and (d) 600 °C. Effective Si thicknesses were t_{eff} = (a) 3.2, (b) 3.1 (c) 2.8 and (d) 3.4 µm.

5d) showed the best initial capacity and capacity retention, so we used T_{an} = 600 °C as the standard post-annealing temperature.

Figure 2-6a shows a top-view SEM image of a Si film with t_{eff} of ~3 μm deposited at a moderate P_{boat} of 1300 W. Compared with the 14 μm-thick Si film deposited at a high P_{boat} of 1600 W (Figure 2-2), a similar striped structure was realized but it did not contain any Si protrusions. The morphology of the Si films with t_{eff} of ~3 μm depended on T_{sub} during deposition (Figure 2-6b–d). A low T_{sub} of 100 °C suppressed the surface diffusion of deposited Si atoms on the surface of the Cu substrate and growing Si film, which made Si film have a porous structure. These Si films were composed of

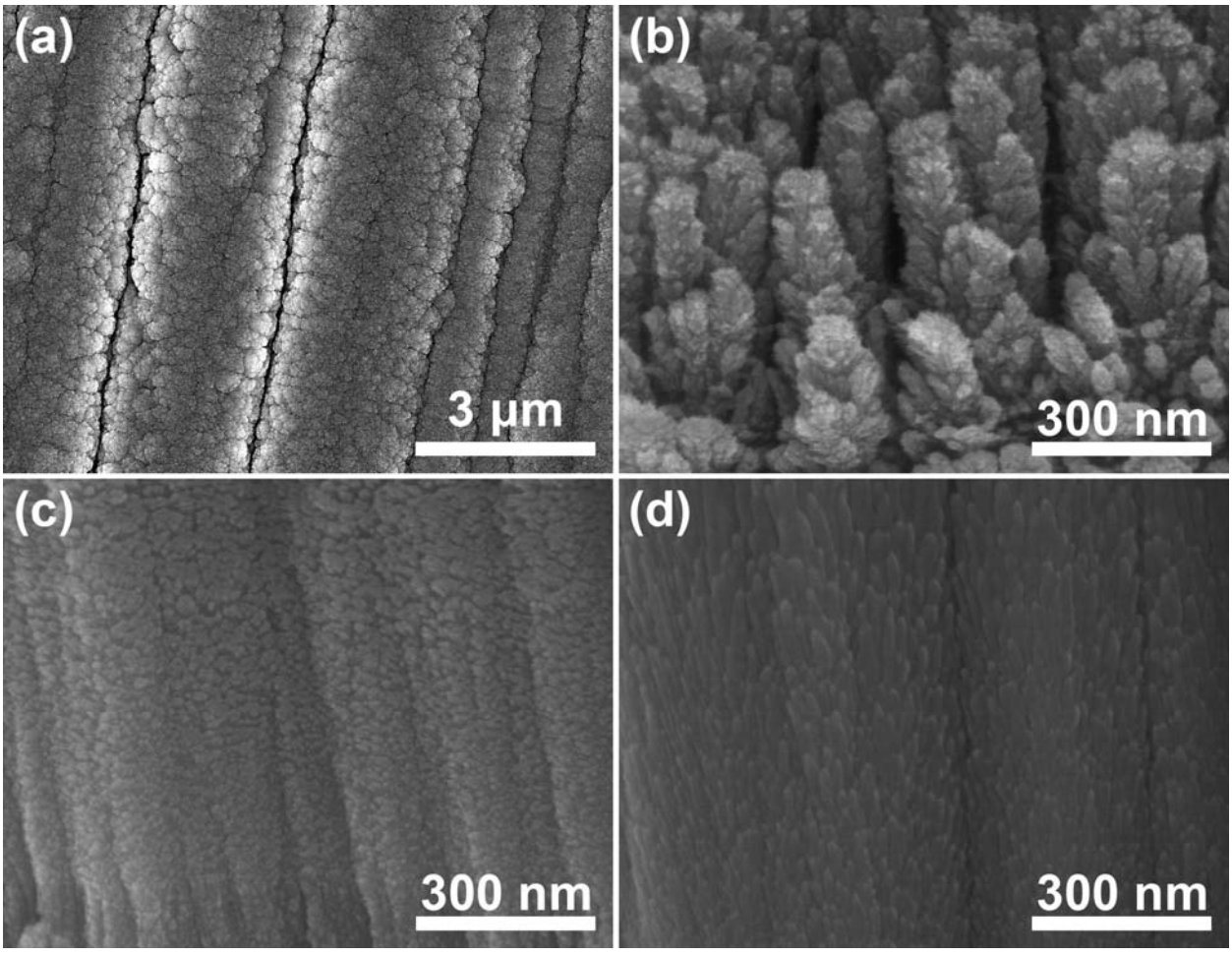

Figure 2-6 (a) Top-view SEM image of a Si film deposited at T_{sub} = 300 °C. Cross-sectional SEM images of Si films deposited at T_{sub} of (b) 100, (c) 300, and (d) 500 °C. All of the films were deposited by RVD in 1 min at a moderate P_{boat} of 1300 W.

numerous Si pillars with a lateral size ~50 nm and many pores between Si pillars, which were obviously induced by a shadowing effect (Figure 2-6b). In contrast, T_{sub} of 300 and 500 °C during deposition yielded denser porous Si films (Figure 2-6c and d, respectively). The striped, porous structures will not only facilitate rapid diffusion of Li^+, but also relax the stress caused by volume changes during cycling. The electrochemical performance of these Si films should be modulated by their different porous structure.

We next evaluated the film density by measuring the weight and volume of the films. Typical thickness distribution is shown in Figure 2-7, from which we determined film volumes. The film density and porosity obtained using different conditions are summarized in Table 2-1. Here we define the porosity p_{film} as (1),

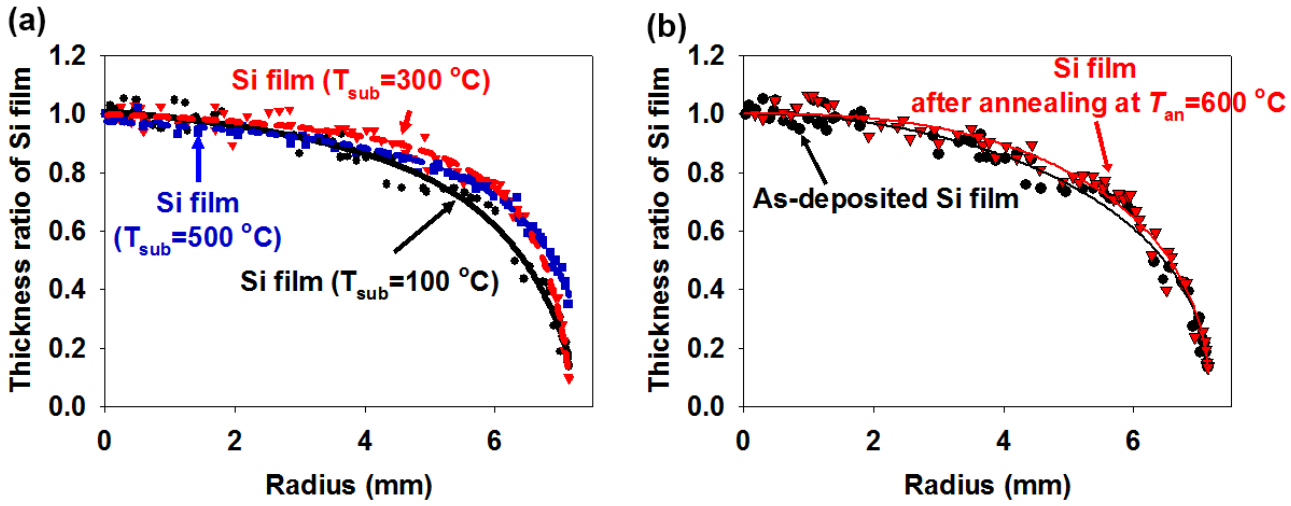

Figure 2-7 Thickness profiles of typical porous Si films deposited on Cu substrates by RVD. (a) As-deposited films at different T_{sub}. (b) As-deposited and post-annealed films with T_{sub} = 300 °C.

Table 2-1 Mass density and porosity of Si films formed at different temperatures

Sample conditions	ρ_{film} (g cm^{-3})	p_{film} (a.u.)
As-deposited at T_{sub} = 100 °C	1.54	0.34
Deposited at T_{sub} = 100 °C and annealed at T_{an} = 600 °C	1.57	0.33
As-deposited at T_{sub} = 300 °C	1.74	0.25
As-deposited at T_{sub} = 500 °C	1.98	0.15

$$p_{\text{film}} \equiv \frac{\rho_{\text{Si}} - \rho_{\text{film}}}{\rho_{\text{Si}}} \quad (1)$$

where ρ_{Si} and ρ_{film} are the mass densities of bulk Si and porous Si film, respectively. The Si film showed the lowest ρfilm = 1.54 g cm^{-3} and highest p_{film} = 0.34 when deposited at T_{sub} = 100 °C, moderate ρ_{film} = 1.74 g cm^{-3} and p_{film} = 0.25 when deposited at T_{sub} = 300 °C, and highest ρ_{film} = 1.98 g cm^{-3} and lowest p_{film} = 0.15 when deposited at T_{sub} = 500 °C. In contrast, post-annealing at T_{an} = 600 °C, had little influence on the density and porosity of the films.

2.4 Effects of the surface condition of the Cu substrates on the cycle performance

The surface condition of the Cu substrate strongly affects the adhesion between the Si films and Cu substrates, and thus was evaluated by XPS. Only O and C were observed as contaminants in addition to Cu, as shown in Figure 2-8 and Table 2-2. The as-purchased Cu substrate contained a large amount of C (69.9 at%) on its surface, possibly from an oily contaminant used during mechanical processing, which resulted in Si films being easily detached from the Cu substrate in a "Scotch-tape" test. Sonication in isopropanol followed by UV-O_3 treatment reduced the surface C content to 29.8 at%, but increased the O content to 50.9 at%. The Cu 2p peaks became evident with the $2p_{3/2}$ peak centred

Table 2-2 Elemental compositions of Cu plate surfaces after different treatments

Surface conditions	Cu ($2p_{3/2}$) (at%)	O (1s) (at%)	C (1s) (at%)
As-purchased	6.5	23.6	69.9
UV-O_3 treated	19.3	50.9	29.8
UV-O_3 & H_2 annealed	63.6	24.6	11.8

at 933.8 eV (Figure 2-8b), which is chemically shifted to higher binding energy from the Cu^0 position (932.4 eV) because of surface oxidation. The full-width at half maximum (FWHM) of the Cu $2p_{3/2}$ peak was large (3.84 eV), which was attributed to multiplet splitting caused by Cu^{2+} [101, 102]. The UV-O_3-treated surface improved the adhesion between Cu and as-deposited Si (stable against the Scotch-tape test), but corrosion of CuO occurred at the Cu-Si interface during Li^+ intercalation [103-105], resulting in detachment of the Si film. H_2 annealing following UV-O_3 exposure resulted in considerable reductions in both C (11.8 at%) and O (24.6 at%) surface contents (Table 2-2). The Cu 2p peaks were more intense, sharper (FWHM = 1.31 eV for Cu $2p_{3/2}$), and the binding energy of the Cu $2p_{3/2}$ peak was centred at 932.4 eV, consistent with the Cu substrate having a metallic surface.

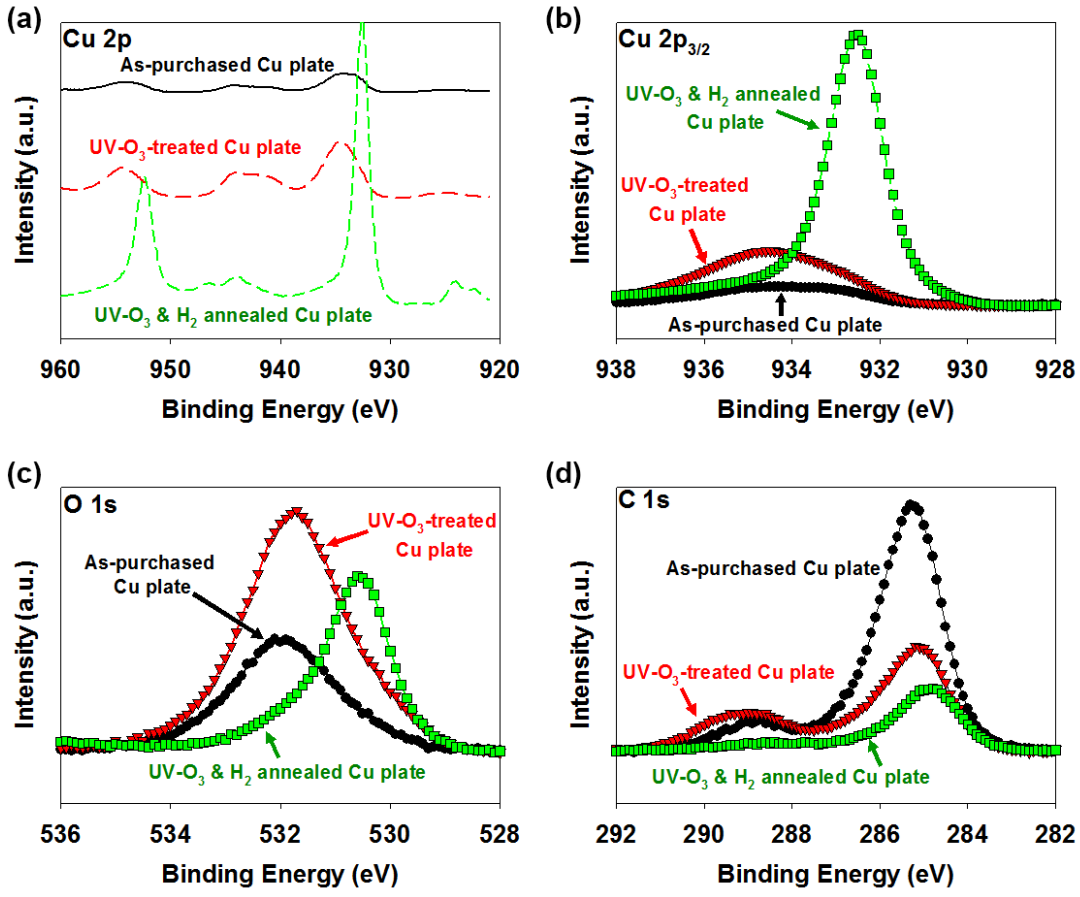

Figure 2-8 XPS analysis of the surfaces of Cu plates after different treatments; as purchased, after UV-O_3 treatment for 3 min, and after UV-O_3 treatment for 3 min followed by annealing under 5 vol% H_2 at 1 atm and 800 °C for 10 min. (a) Cu 2p, (b) Cu $2p_{3/2}$, (c) O 1s, and (d) C 1s.

Such a metallic surface allowed good adhesion of the Si films to the Cu substrates without the problem of corrosion at the Cu-Si interface during Li^+ insertion, as shown later. Thus, we used UV-O_3 and H_2 annealing as the standard procedure for treating the Cu substrates in the following experiments.

2.5 Heat treatment to enhance interfacial adhesion while retaining porous structure

The temperatures of the Cu substrate during RVD (T_{sub}) and post-annealing (T_{an}) are the most important factors that determine the crystallinity of deposited Si films as well as the thickness of the intermixed layer between the Si film and Cu substrate. With regard to the crystallinity of Si films, the amorphous phase is preferred because of its isotropic expansion behavior rather than the crystalline phase, which shows anisotropic expansion during Li^+ insertion [106]. Moreover, the diffusion of Li^+ into amorphous Si is much faster than that into crystalline Si [107]. Figure 2-9a shows the Raman spectra of a series of Si films formed at different Cu substrate temperatures. These films possess different degrees of crystallinity from a pure amorphous phase to a mixture of amorphous and microcrystalline phases depending on the temperature of the Cu substrate. The crystal structure of Si is diamond cubic, which is characterized by one intense sharp peak around 520 cm^{-1} in Raman spectra. This peak broadens and/or shifts to lower frequency when the crystal size is ≤ several tens of nanometers. T_{sub} = 500 °C resulted in a mixture of microcrystalline and amorphous phases, while lower T_{sub} (100–300 °C) gave the pure amorphous phase with a broad band at around 480 cm^{-1}. Intermixing between Cu and Si is also important to enhance the adhesion between Si films and Cu substrates and suppress the lifting of the Si films from the Cu substrates. In addition to the effect of T_{sub} during Si deposition, we examined the effect of T_{an} on the depth profile of the elemental composition of the films. SEM-EDS analysis showed little intermixing in the as-deposited Si film

prepared at low T_{sub} = 100 °C, and more intermixing for higher T_{sub} of 300–500 °C (Figure 2-9b). Intermixing was also enhanced by post-annealing at T_{an} = 600 °C the Si films deposited at T_{sub} = 300 °C. Deposition at high Cu substrate temperature (T_{sub}) increased both the crystallisation of Si films

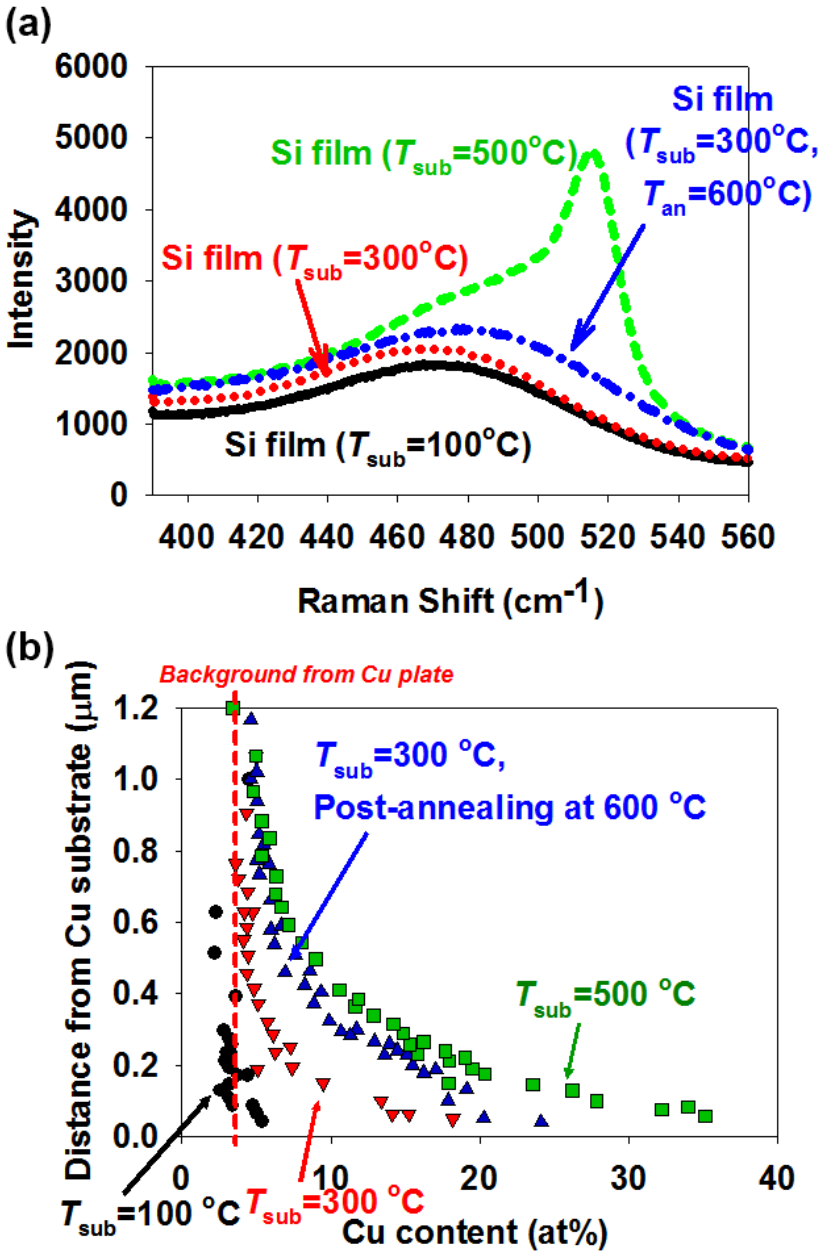

Figure 2-9 (a) Raman spectra of Si films (t_{eff} = 3–4 µm) deposited at T_{sub} = 100, 300, and 500 °C on Cu plates. (b) Depth profiles of the elemental compositions of Si films (t_{eff} = 3–4 µm) deposited at T_{sub} = 100, 300, and 500 °C without post annealing and that deposited at T_{sub} = 300 °C with post-annealing at T_{an} = 600 °C measured by SEM-EDS. The Cu signal of ~3 at% is a background signal from the Cu plate for all measurements.

and intermixing between the Si films and Cu substrates while post-annealing at an appropriate temperature (T_{an} = 600 °C) enhanced intermixing only. Through such temperature control, we can obtain 3–4-μm-thick Si films that contain both amorphous and microcrystalline phases with an intermixed layer that is 10% of the total thickness of the Si films.

2.6 Cycle performance and impedance analysis of porous Si films

The electrochemical behavior of Si films (t_{eff} = 3–4 μm) deposited at different T_{sub} on Cu substrates was investigated by galvanostatic charge-discharge measurements using half cells (Figure 2-10). Figure 2-10a shows the initial charge/discharge capacities of the Si films. In the initial lithiation process, the voltage profile of all films coincided with that of previous Si films with a plateau region at a potential below 0.2 V *vs.* Li/Li^+, which indicates that amorphous Si reacted with Li^+ to form amorphous Li_xSi alloy [61]. In the case of lower T_{sub} of 100 and 300 °C, charge capacities reached 2759 and 2471 mAh g_{Si}^{-1} while discharge capacities were 1151 and 1494 mAh g_{Si}^{-1}, for 0.05C for T_{sub} = 100 °C and 0.1*C* for T_{sub} = 300 °C, respectively. The large irreversible capacity is mainly attributed to the consumption of Li^+ in the formation of an SEI layer [108]. In particular, the large exposed surface area of the porous structure formed at low T_{sub} (Figure 2-6b, c) consumed a large amount of Li^+ during SEI formation, resulting in low first Coulombic efficiencies of 41% (T_{sub} = 100 °C) and 60% (T_{sub} = 300 °C). Moreover, the Si films are vulnerable to oxidation, particularly amorphous Si compared with crystalline Si. Oxidation of the Si films during the time (2 days or more) between Si deposition and electrochemical testing should have a considerable effect on cycling performance. In contrast, the Si film deposited on a Cu substrate at T_{sub} = 500 °C exhibited the highest initial charging (Li^+ insertion) capacity of 4045 mAh g_{Si}^{-1} at a rate of 0.05*C* with a discharge capacity

of 3328 mAh g_{Si}^{-1}. The charge capacity is nearly equivalent to the theoretical value for $Li_{22}Si_5$ alloy (4200 mAh g_{Si}^{-1}) [61]. This is because the high T_{sub} yielded dense Si films with reduced surface area (Figure 2-6d) and partial crystallization of the Si film (Figure 2-9a), which can reduce SEI formation

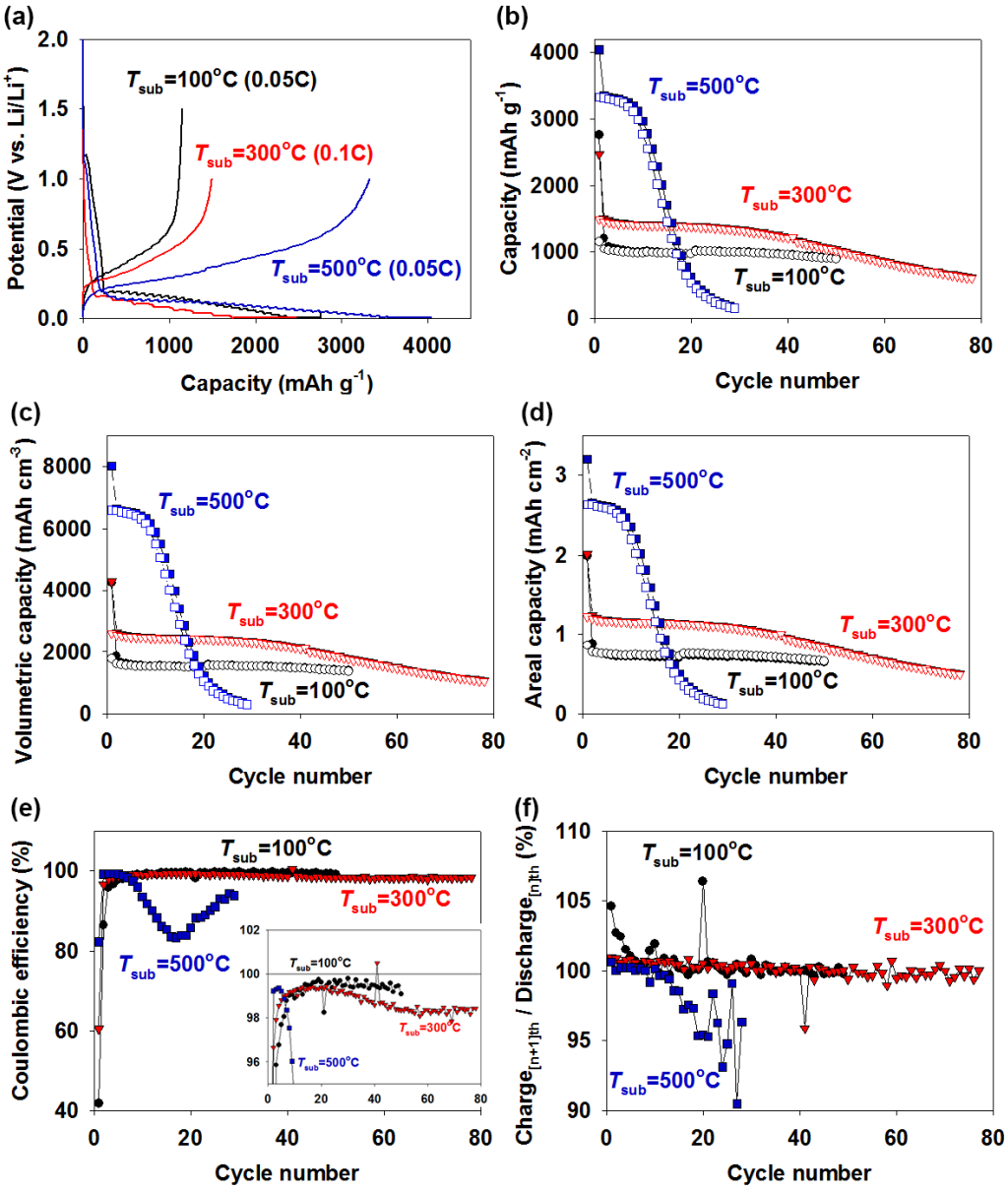

Figure 2-10 Electrochemical performance of Si films deposited at T_{sub} = 100, 300, and 500 °C on Cu plates (t_{eff} = 3.1, 3.5, and 3.4 μm respectively). (a) Voltage-capacity curves for the first charge/discharge cycles. Cycle performance at 0.1*C* expressed as (b) gravimetric capacity, (c) volumetric capacity, and (d) areal capacity. (e) Coulombic efficiency. (f) The capacity ratio of charge at the $[n+1]^{th}$ cycle to discharge at the $[n]^{th}$ cycle, which provides information about the reaction of the newly used Si through cycles. The cycle test was made at 0.1*C* for all cycles (1–80) for T_{sub} = 300 °C, and at 0.05*C* for the first cycle and 0.1*C* for later cycles (≥2) for T_{sub} = 100 and 500 °C.

and oxidation of the Si film, compared with the films formed at lower T_{sub}. However, the Si film deposited at T_{sub} = 500 °C showed more rapid degradation than those deposited at lower T_{sub}, resulting in a poor capacity retention of 15% after 20 cycles (Figure 2-10b). This is possibly because of the small porosity (p_{film} = 0.15, Table 2-1) and mixed amorphous and microcrystalline phases (Figure 2-9a) in this film, which resulted in large stress upon volume change during cycling. Another possible explanation is that Li^+ reached the Si/Cu interface at around the 10th cycle and corroded the interface for this film having the thickest $CuSi_x$ intermixed layer (Figure 2-9b). The previous works reported the absence at room temperature [109] but existence at ~120 °C [110] of the reaction of Cu_3Si alloy with Li^+. When we consider that the Si film deposited at T_{sub} = 300 °C had a similarly thick Cu_3Si intermixed layer but did not show such abrupt capacity fade, the latter explanation seems less probable. In contrast, the Si film deposited at T_{sub} = 300 °C showed much higher capacity retention of 81% with a discharge capacity of 1210 mAh g_{Si}^{-1} after 40 cycles, which decreased to 40% and ~600 mAh g_{Si}^{-1}, respectively, after 80 cycles.

The Si film deposited at T_{sub} = 100 °C showed interesting behavior; it exhibited the smallest discharge capacity of the films of 1151 mAh g_{Si}^{-1} for the first cycle but a good capacity retention of 70% after 50 cycles. The high porosity of this film of p_{film} = 0.34 (Table 2-1) as well as the thick SEI layer formed in the first cycle should contribute to the stable charge/discharge capacity. The volumetric capacity (mAh cm_{film}^{-3}) and areal capacity (mAh cm_{anode}^{-2}) of films are critically important for practical battery devices. Thus, the cycle performance based on gravimetric capacity (mAh g_{Si}^{-1}) in Figure 2-10b is plotted as volumetric capacity and areal capacity in Figure 2-10c and d, respectively. The volumetric capacity of the Si film formed at T_{sub} = 100 °C (Figure 2-10c) was about 1500 mAh cm^{-3} after 50 cycles, which is nearly four times the capacity of commercial graphite anodes [111]. It should be noted that there is still potential to increase the capacity of later cycles by optimising the Si film porosity and operating conditions such as electrolyte additives and cut-off potential. The areal

capacity of the Si film formed at T_{sub} = 100 °C (Figure 2-10d) was also higher (0.66 mAh cm^{-2}) than the previous values reported for Si nanomaterials (0.2–0.4 mAh cm^{-2}) [79, 88] and approaching that of commercial graphite anodes (~4 mAh cm^{-2}, 18650 Li-ion cells, Sony, Japan) [112] and the recent Si-base hybrid materials (2 mAh cm^{-2}) [113].

The films deposited at T_{sub} = 100 and 300 °C also showed rather good Coulombic efficiency (Figure 2-10e). After the 5th cycle, Coulombic efficiency was above 98%, and remained at ~99.5% for 50 cycles for T_{sub} = 100 °C and 98–99.5% for 80 cycles for T_{sub} = 300 °C. The capacity ratio of the [n+1]th charge over the [n]th discharge for the films is plotted in Figure 2-10f. The ratio was above 100% for the initial 30 cycles, suggesting that the Si anode did not fully react initially and unreacted Si gradually contributed to the reaction with increasing cycle number, compensating for the decrease in discharge capacity (99% Coulombic efficiency corresponds to 1% loss in effective Si for each cycle) and maintaining the capacity retention. The quick capacity fade observed for the Si film with T_{sub} = 300 °C after the 30th cycle (Figure 2-10b) suggests the depletion of the unreacted Si. The Si film deposited at T_{sub} = 300 °C and post-annealed at T_{an} = 600 °C (t_{eff} = 3.5 μm) was investigated by EIS after charging for different numbers of cycles. In the Nyquist plot (Figure 2-11), a pronounced

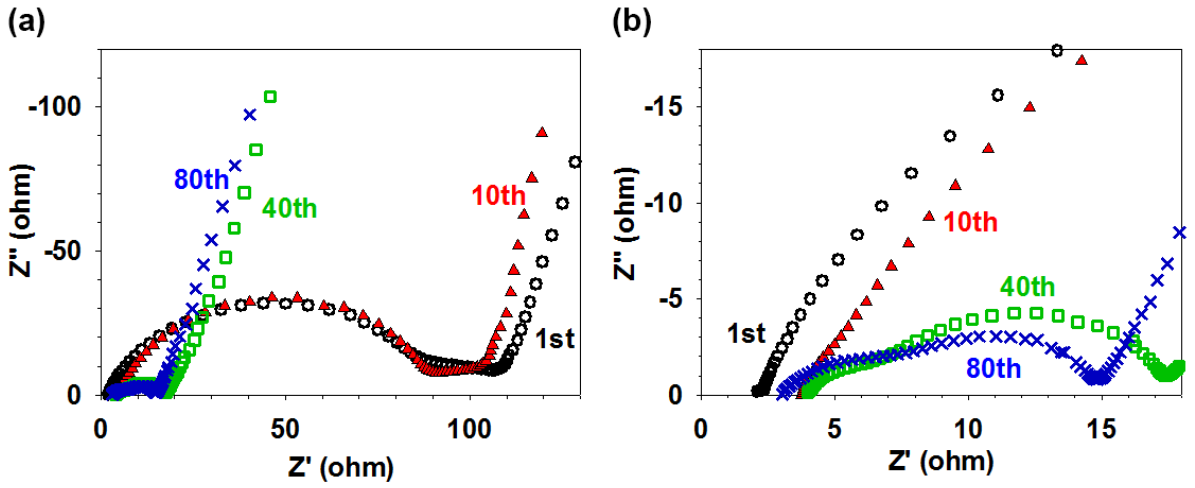

Figure 2-11 Nyquist plots of a thick Si film anode (t_{eff} = 3.5 μm) deposited at T_{sub} = 300 °C and post-annealed at T_{an} = 600 °C after charging for different numbers of cycles.

semicircle appeared at the 1st cycle and this semicircle did not change for the 10th cycle. We attribute this to the large reaction resistance for the unreacted Si remaining in the charged Si film, which was evidenced by the capacity ratio of the [n+1]th charge over the [n]th discharge exceeding 100% for the initial 30 cycles (Figure 2-10f). This semicircle got much smaller after the 40th cycle (Figure 2-11), which we attribute to the depletion of the unreacted Si in the charged Si film, which was observed in the capacity ratio of the [n+1]th charge over the [n]th discharge of less than 100% for >30 cycles

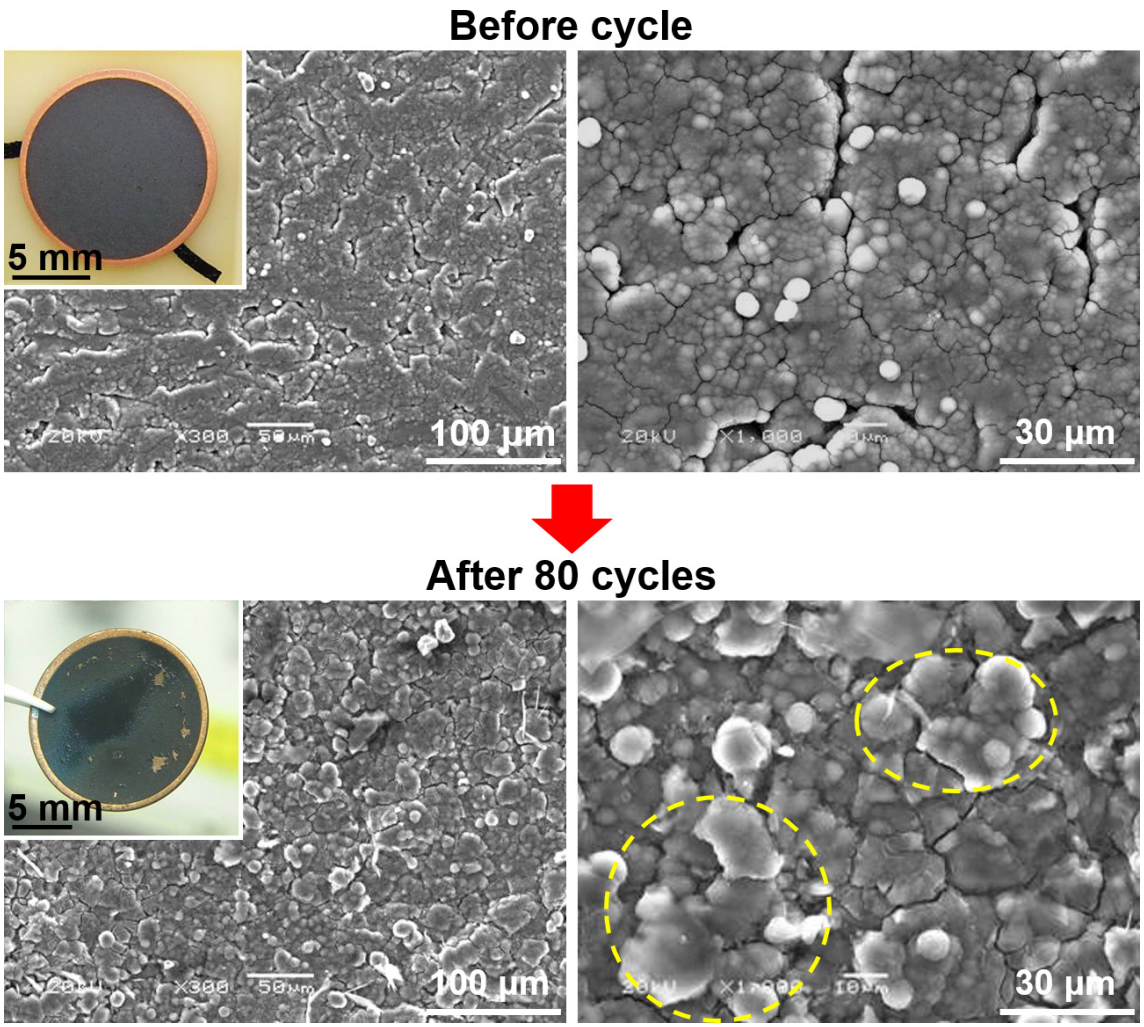

Figure 2-12 Photographs and SEM images of the Si film deposited at T_{sub} = 300 °C and post-annealed at T_{an} = 600 °C before and after the charge-discharge cycle. The sample is the same as that in Fig. 7. Before the cycle, the Si film was uniform over the Cu substrate and show porous surface structure. While it was detached from the substrate at some regions to show the Cu surface in the photograph and had several-tens-µm large protrusions in the SEM images after 80 cycles.

(Figure 2-10f). It is reasonable to consider that the reaction resistance became much smaller once the porous Si film was lithiated [114]. We also see a slight increase of contact resistance between the 1st and 10th cycles (Figure 2-11). We attribute this to some detachment of the Si film from the Cu substrate despite the improved Si/Cu interface with a composition gradient fabricated by thermal treatment at T_{sub} = 300 °C and post-annealing at T_{an} = 600 °C. We also characterized the same Si film

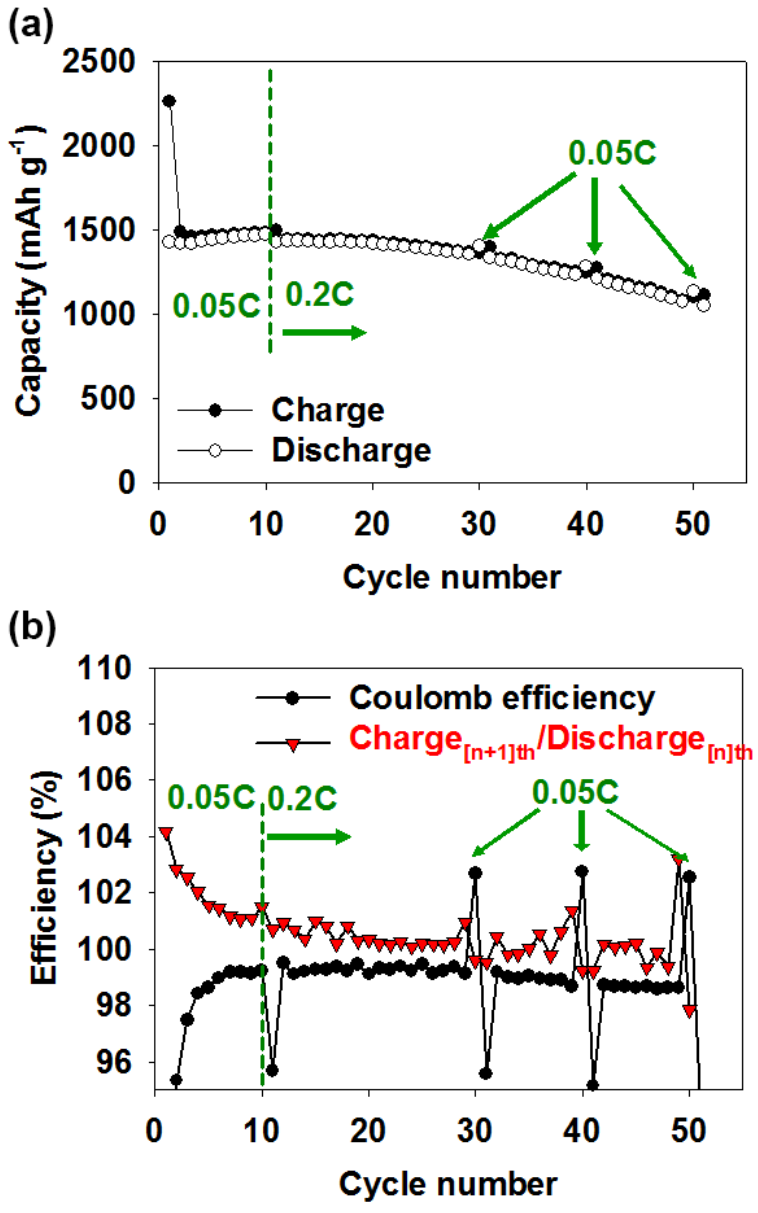

Figure 2-13 (a) Rate capability of a thick Si film (t_{eff} = 3.1 µm) deposited on a Cu plate at T_{sub} = 300 °C and post-annealed at T_{an} = 600 °C for 50 cycles. (b) Coulombic efficiency and the capacity ratio of charge at the $(n+1)^{th}$ cycle to discharge at the $(n)^{th}$ cycle as a function of cycle number n of the same film as in (a).

before and after the cycles. The photographs and SEM images (Figure 2-12) shows the uniform Si film over the Cu substrate with porous surface structure before the cycle. On the other hand, the Si film was detached from the substrate at some regions to show the Cu surface in the photograph and had several-tens-μm large protrusions in the SEM images after 80 cycles. Some countermeasure such as using nano-/micro-structured substrate would be needed to enhance the interfacial adhesion further.

The rate capability of a representative 3.1-μm-thick Si anode deposited at T_{sub} = 300 °C and post-annealed at T_{an} = 600 °C is shown in Figure 2-13. Starting from 0.05C at the 1st cycle, the Si film achieved a discharge capacity of 1426 mAh g_{Si}^{-1}, which increased to 1472 mAh g_{Si}^{-1} after 10 cycles. This increase is because unreacted Si gradually reacted with Li^+ and contributed to the discharge capacity as can be seen in the $charge_{[n+1]th}/discharge_{[n]th}$ capacity ratio of > 100% with smaller loss of reacted Si, which is evidenced by the Coulombic efficiency approaching 100% (Figure 2-13b). When the current density was quadrupled to 0.2*C* from the 11th cycle, Coulombic efficiency dropped from above 99% to 95%, but recovered immediately at the 12th cycle. Moreover, the discharge capacity showed only a slight decrease to 1428 mAh g_{Si}^{-1} at 0.2*C*. After the 20th cycle, both the charge and discharge capacity of the film started to decrease gradually. When the charge/discharge rate were set back to 0.05*C* at the 30th, 40th and 50th cycles, both the charge and discharge capacity increased slightly by a few tens of mAh g_{Si}^{-1}. This small capacity difference of a few percent confirms the sufficient rate performance of the Si anode for 0.05*C*–0.2*C*. At the 50th cycle, a reversible capacity of 1050 mAh g_{Si}^{-1} was achieved at 0.05*C*. The Coulombic efficiency was above 98% for cycle 5–50 regardless of the current density (0.05*C* or 0.2*C*).

2.7 Conclusions

We developed the RVD method, in which a Si source is heated to well above its melting point (T_{boat}

= 2000−2400 °C) while a Cu substrate is kept at much lower temperature (T_{sub} = 100–500 °C), and rapidly deposited 3–14-μm-thick porous Si films directly on Cu substrates in 10 s to 1 min. Such deposition is several orders of magnitude faster than the conventional physical vapour deposition methods using Si source near its melting point (6–90 nm min^{-1} by thermal evaporation) or the sputtering (8.6 nm and 2.8–6.1 nm min^{-1} by radio frequency magnetron sputtering). And such fast deposition eliminates the need for ultra-high vacuum systems because the contaminant oxygen is diluted by the rapidly depositing Si. Compared with chemical vapour deposition methods, RVD uses the safe source instead of the explosive/toxic silane/chlorosilane sources, and moreover the Si vapour enables deposition at low temperatures, leading to the spontaneous roughening of the Si film. The Si films had striped, porous structure, with different porosity (p_{film} = 0.15–0.34) and ratio of amorphous to microcrystalline phases depending on T_{sub}. Rapid deposition of 14 μm of Si in 10 s resulted in protrusions in the films, while moderately rapid deposition of 3–4 μm in 1 min gave films without protrusions. Pretreatment of the Cu substrates by sonication in isopropanol followed by UV-O_3 treatment and finally annealing in H_2/Ar at 800 °C was effective to remove C and O contaminants from their surfaces. The as-deposited porous Si films showed very poor charge-discharge cycle performance that was improved considerably once the films were annealed at 600 °C for 10 min because a sub-micrometer-thick $CuSi_x$ intermixed layer formed at the Si/Cu interface without the Si films crystallizing. The rather dense (p_{film} = 0.15), thick Si films (t_{eff} = 3.4 μm) of mixed amorphous-microcrystalline phase deposited at T_{sub} = 500 °C showed fairly high initial charge/discharge capacities of 4045 and 3328 mAh g_{Si}^{-1} at 0.05*C*, respectively, and kept a high capacity of >3000 mAh g_{Si}^{-1} for the first 10 cycles but their capacity decreased to below 500 mAh g_{Si}^{-1} after 20 cycles. The dense structure of these films possibly suppressed their oxidation in air and excess SEI layer formation, resulting in good initial performance but large stress caused by volume changes during cycling, resulting in the rapid capacity fade within 20 cycles. In contrast, the low-density (p_{film} = 0.33) thick amorphous Si films (t_{eff} = 3.1 μm) deposited at T_{sub} = 100 °C showed a rather small discharge

capacity of 1151 mAh g_{Si}^{-1} for the first cycle but good capacity retention of 70% after 50 cycles. The porous structure of these films possibly facilitated their oxidation in air and excess SEI layer formation, resulting in a small initial discharge capacity but suppressed the stress caused by volume changes during cycling and yielded a stable SEI layer, resulting in rather good cycle stability. The reversible capacity of ~1000 mAh g_{Si}^{-1} after 50 cycles of the Si film deposited at low T_{sub} (100 °C) corresponds to a high volumetric capacity of ~1500 mAh cm_{film}^{-3} and areal capacity of ~0.5 mAh cm_{anode}^{-2}, which suggest Si anodes may be suited for practical use. Toward the future goal having porous Si films of t_{eff}~10 μm on both sides of a 15-μm -thick Cu foil and operating it for longer cycles of ~1,000 or more, we are now examining the charge limitation to reduce the volume expansion and additives to electrolyte to make more stable SEI. Although further improvement is needed in thickness and cycle performance, the RVD method yielding micrometer-thick Si films rapidly from an inexpensive, safe Si source, and that allows control over porosity, crystallinity, and interface with the Cu collector, and that can be applied to various substrates including nano-/micro-structured substrates, is a promising route to fabricate practical Si anodes for LiBs.

Chapter 3 – Rapidly deposited, porous Si–Cu anodes with compositional gradients

3.1 Introduction

For the efficient use of electrical energy and particularly renewable energy, electrical energy storage systems are very important. Rechargeable lithium ion batteries have been used successfully in portable electronic device and electric vehicle applications, but there is considerable demand for further enhancements of the energy and power densities of these batteries, along with the need for cost reduction. Si is considered to be a promising anode material for lithium secondary batteries [65]. Si can accommodate up to 4.4 lithium atoms per Si atom ($Li_{4.4}Si$ alloy), thus yielding huge theoretical gravimetric and volumetric capacities of 4200 mAh g_{Si}^{-1} and 9786 mAh cm_{si}^{-3}, respectively, which are approximately ten times larger than the corresponding values for conventional graphite [61-64]. However, this high specific capacity is realized by holding large amounts of Li with Si, and is accompanied by large volume changes (300–400%, depending on the state of Li_xSi [66-68]). Si anodes cannot withstand the heavy strain of this expansion and thus break down, resulting in the pulverization and delamination of entire structures [69-71]. Various structures, including porous thin films [85, 86], hollow-structured double-walled Si nanotubes [80] and composites of Si with carbon [82, 115], carbon fibres [60], and silicides [83], have previously been reported that can accommodate the volume changes. As a result, the high gravimetric capacities of Si-base anode materials were achieved successfully, but sometimes with small Si loads compared with the heavy current collectors,

and also required complicated and time-consuming processing using expensive raw materials. Large-scale and low-cost fabrication of Si anodes with stable electrochemical performance is essential for practical use of these anodes in lithium secondary batteries.

We recently reported a rapid vapour deposition (RVD) method that enables simple fabrication of 3–14-μm-thick porous Si films rapidly in 10–60 s that are deposited directly on the Cu current collectors using inexpensive Si powder sources [116]. Rapid vapour deposition is a physical vapour deposition method in which a source material is heated to much higher temperatures than the melting point of the source (2000–2400 °C for the case of Si), leading to deposition rates that are several orders of magnitude higher than conventional physical vapour deposition methods [85]. Post-annealing at 600 °C enhanced the adhesion of the Si films to the Cu current collectors by yielding a sub-μm-thick intermixed layer, and produced anode capacitances of 1000 mAh g_{Si}^{-1} and 0.66 mAh cm_{anode}^{-2} for the 50th cycle of a moderately thick Si film. The film had an effective thickness of 3–4 μm (t_{eff}, calculated by dividing the areal Si mass by the bulk Si density of ρ_{Si} = 2.33 g cm^{-3}) and porosity of 15–30%. However, delamination failures ultimately occurred because of the high stress at the Si/Cu interface. Strain-graded C-Al-Si multilayers (C, Al and Si experience volume changes of 10, 100 and 400%, respectively, upon lithiation) produced by sputter deposition [94] and Si-base nanowall arrays fabricated by oblique angle deposition [117] are effective approaches for stress relaxation during lithiation/delithiation. Furthermore, well-aligned CuSi nanorod arrays with gradient profiles in Cu and Si compositions were realized by co-deposing Cu and Si with independent dynamic tuning of their deposition rates at 0–0.5 nm s^{-1} (0–0.03 μm min^{-1}) at an oblique angle of 88° with respect to substrate normal although their electrochemical performance was not reported [118]. These processes are attractive in engineering the Si anode structure, however, require high vacuums and long processing times.

Here we propose porous and amorphous Si–Cu films with gradient composition profiles that change

continuously from Cu to Si as ideal structures for defocusing stress during lithiation/delithiation processes. This type of structure corresponds to a strain-graded multilayer with an infinite number of layers, and can be fabricated easily and spontaneously by RVD in 1 min. Si and Cu are co-deposited on the Cu current collector by heating Si and Cu powders together in a carbon boat to ~2000 °C. Cu has a lower melting point (1085 °C) and a higher vapour pressure than Si (melting point of 1414 °C), and vaporizes and is deposited preferentially at the initial stage, whereas Si vaporizes and is deposited preferentially at the later stage. Also, the porous and amorphous structures of the films are realized by keeping the Cu current collector at a low temperature of ~100 °C. I compared the microstructures and electrochemical performances of the Si–Cu films with pure Si films and discussed the effects of the composition gradient and diffuse interface in the Si–Cu films in enhancing the cycle performances.

3.2 Materials and methods

3.2.1 Si–Cu film fabrication

Circular Cu plates (15-mm diameter, 0.5-mm thickness) were used as substrates for the Si–Cu films. The Cu substrates were pretreated by bath sonication in isopropanol for 10 min followed by UV-O_3 exposure for 3 min to remove organic contaminants from their surfaces. The Cu substrates were then annealed under a 4 vol% H_2/Ar flow at ambient pressure and 800 °C for 10 min to remove any organic contaminants and reduce the Cu surface [116]. The Si wafer (p-type, resistivity of 10–20 Ω cm) was immersed in 5 wt% hydrofluoric acid for 1 min and then ground into powder using a mortar and pestle. The Cu powder was used as purchased (~75-μm diameter, 99.9%, Wako Pure Chemicals, Osaka, Japan). These Si and Cu powders were loaded together (with weight ratios of 100:0, 95:5, 90:10, and 80:20) in a carbon boat, heated in the resistively heated carbon boat to ~2000 °C (boat temperature, T_{boat}) in a 0.1-Torr Ar atmosphere, and vaporized rapidly in 1 min. A Cu substrate was

held ~40 mm from the boat and was kept at 100–500 °C (substrate temperature, T_{sub}, 100 °C in most experiments) during deposition to suppress the surface diffusion of the Si and Cu adatoms and yield rough and porous films through the shadowing effect [98, 99]. The Cu substrate was maintained at constant temperature under the strong thermal radiation from the carbon boat by using a substrate holder made of a block of Cu with a large heat capacity that contained an embedded ceramic heater and N_2-gas cooling line [116]. The co-deposited Si–Cu films were post-annealed under a 4 vol% H_2/Ar flow at ambient pressure at 600 °C (annealing temperature, T_{an}) for 10 min to improve the adhesion between the Cu substrate and the Si–Cu film. The areal weight of the Si–Cu film for electrochemical measurements was in the 0.7–0.8 mg cm^{-2} range, corresponding to t_{eff} = 3–3.5 μm. Note that the Si content of the Si–Cu films is less than 100% and thus the actual Si content in the films is lower than that in bulk Si films with the same t_{eff}.

3.2.2 Characterization

The microstructures and the elemental composition distributions of the Si–Cu films were characterized by scanning electron microscopy (SEM; Hitachi S-4800, Tokyo, Japan) equipped with energy-dispersive X-ray spectroscopy (EDX; EDAX Genesis, AMETEK, Elancourt, France). The specific surface area and pore volume of the Si–Cu films were obtained by Brunauer-Emmett-Teller (BET) analysis of nitrogen adsorption isotherms measured at 77 K (Quantachrome Instruments Autosorb 1C, Boynton Beach, FL, USA). The crystal structures of the Si–Cu films were characterized by X-ray diffraction (XRD; Rigaku RINT Ultima III, Akishima, Japan) using Cu Kα radiation (λ = 1.54 Å). Following the charge–discharge cycles, some samples were also characterized after delithiation and rinsing with dimethyl carbonate (DMC).

3.2.3 Electrochemical characterization

Electrochemical measurements were performed using three-electrode beaker cells. Either a Si film or a Si–Cu film on a Cu substrate as a working electrode, Li metal (15 mm × 30 mm) as the counter electrode, and a Li reference electrode was set up in an Ar glove box with a dew point that was lower than −90 °C. Lithium perchlorate ($LiClO_4$, 1 M) in a 1:1 (v/v) mixture of ethylene carbonate (EC) and propylene carbonate (PC) with H_2O content of less than 20 ppm (Kishida Chemical, Osaka, Japan) was used as the electrolyte. Charge/discharge measurements were carried out in a potential range of 0.005–1.200 V *vs.* Li/Li^+ in constant-current (CC) mode with different rates of 0.1*C*–1*C* using a battery charge/discharge system (Hokuto denko HJ1020mSD8, Tokyo, Japan). The *C*-rate was determined using the sum weight of Si and Cu and a value of 4200 mAh g_{film}^{-1} for the theoretical capacity regardless of the Cu content. For the Si–Cu films, the Cu contributes to the weight but not to the capacity, making the theoretical capacity smaller than this value, and thus the actual *C*-rate should be higher. In this work, I define lithiation as "charge" and delithiation as "discharge". Three-electrode cells were also used to perform electrochemical impedance spectroscopy with a potentiostat (Bio-Logic VMP3, Claix, France).

3.3 Microstructure and composition profile of Si–Cu films

Figure 3-1 shows a typical Si–Cu film with actual thickness of 2.7 μm (t_{act}). The film had a wall-shaped structure that was induced by stripe patterns on the Cu substrate surface (Figure 3-1a), which was quite similar to the pure Si films in our previous report [116]. The porous structure is visible in the high-resolution cross-sectional images (Figure 3-1b and c), and is induced by suppressed surface diffusion of the deposited Si and Cu at the low T_{sub} of 100 °C. The Si–Cu films deposited at higher T_{sub} are also shown in Figure 3-1d and e. The film got denser for the higher T_{sub}. Among the Si–Cu

films deposited at T_{sub} = 100, 300, and 500 °C, those deposited at 100 °C showed the best electrochemical performance (Figure 3-2), and thus T_{sub} was fixed at 100 °C in the following

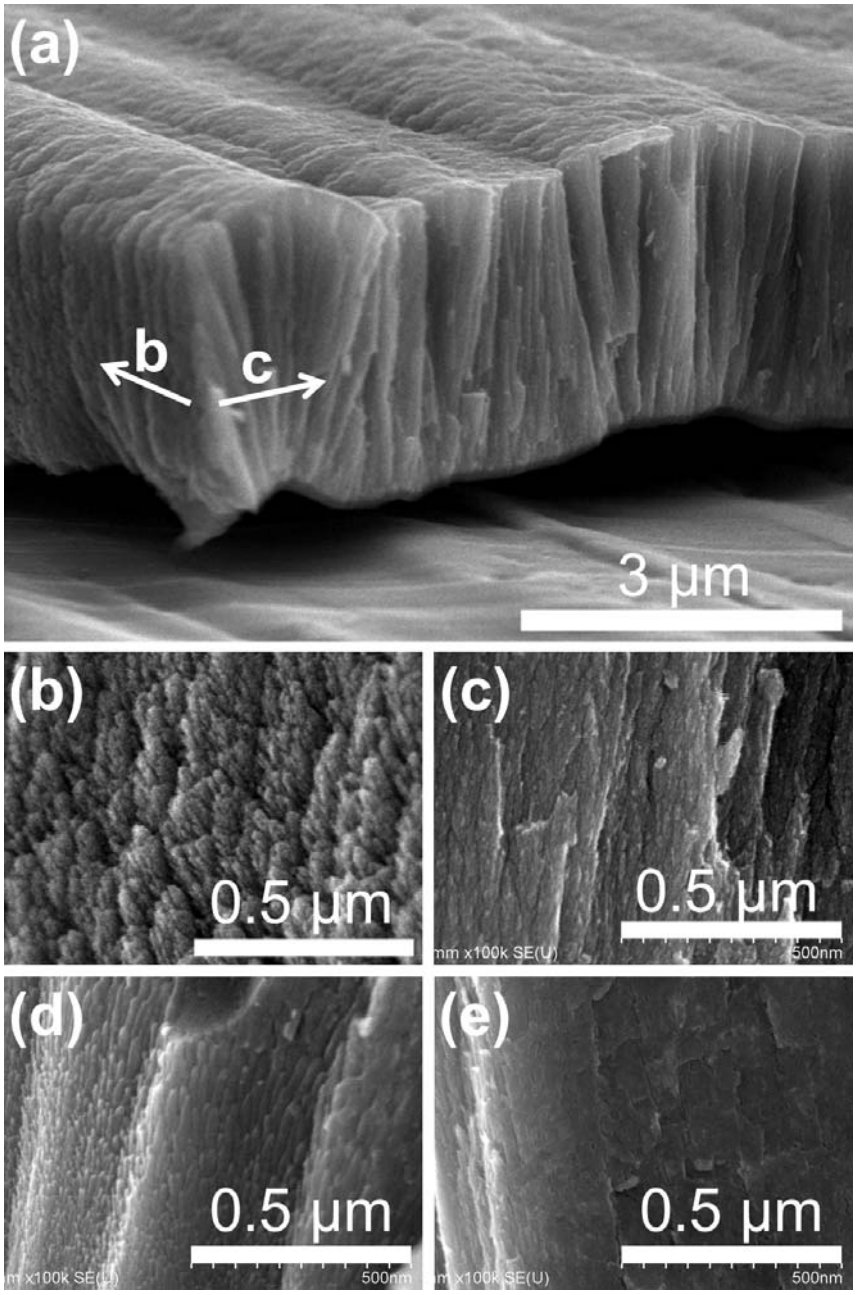

Figure 3-1 SEM images of typical Si–Cu films prepared by RVD using a 5 wt% Cu source in 1 min without post-annealing. The Si–Cu film deposited at T_{sub} = 100 °C (t_{act} ≈ 2.7 μm, ρ_{film} ≈ 1.54 g cm^{-3}); (a) the tilted view, (b) the cross-sectional view in the longitudinal direction, and (c) the cross-sectional view in the transverse direction of the stripe patterns on the Cu substrate surface. The Si–Cu films deposited at T_{sub} = 300 °C (d) (t_{act} ≈ 2.8 μm, ρ_{film} ≈ 1.87 g cm-^{3}) and at T_{sub} = 500 °C (e) (t_{act} ≈ 2.6 μm, ρ_{film} ≈ 2.01 g cm^{-3})

experiments. The cross-sectional images were acquired by bending the 0.5-mm-thick Cu substrate, which resulted in detachment of the Si–Cu film. Post-annealing at T_{an} = 600 °C for 10 min was thus performed on the films that were used for electrochemical measurements to enhance the adhesion of these films to the Cu substrates.

Cross-sectional SEM images of the pure Si and Si–Cu films that were deposited using Si sources with various Cu contents are shown in Figure 3-3a–d. The films that were deposited in 1 min had t_{act} of 2.3–6.7 µm, showing that such rapid deposition is possible, regardless of the Cu content of the source. The pure Si film showed no contrast in its cross-section from bottom to top (Figure 3-3a), while the Si–Cu film showed a clear change in brightness from bottom to top (Figure 3-3b–d). This change in

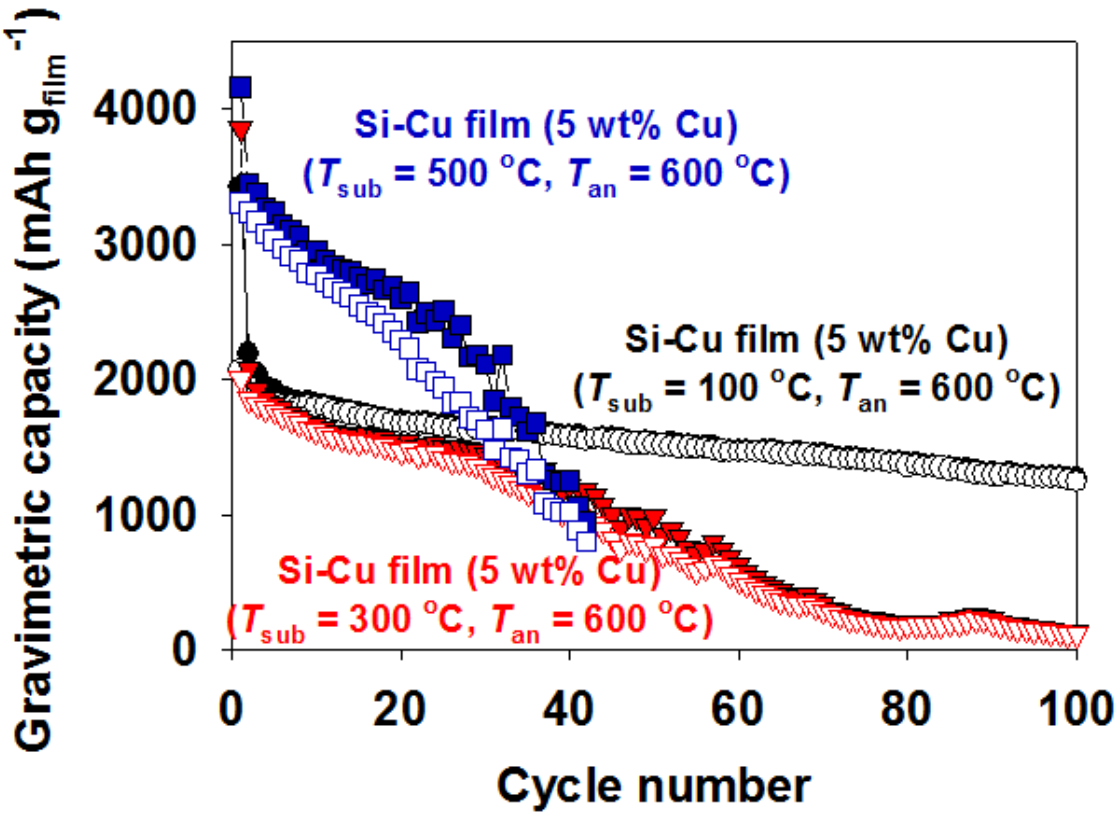

Figure 3-2 Electrochemical performance of the Si–Cu films deposited using the 5 wt% Cu source at various T_{sub} of 100, 300, and 500 °C. All samples were post-annealed at Tan = 600 °C and measurements were carried out using 1 M LiClO4 in a 1:1 (v/v) mixture of EC and PC as the electrolyte

brightness indicates the change in the Cu content of the film. I also evaluated the mass densities of the Si and Si–Cu films by measuring the masses and volumes of these films [116]. The pure Si film

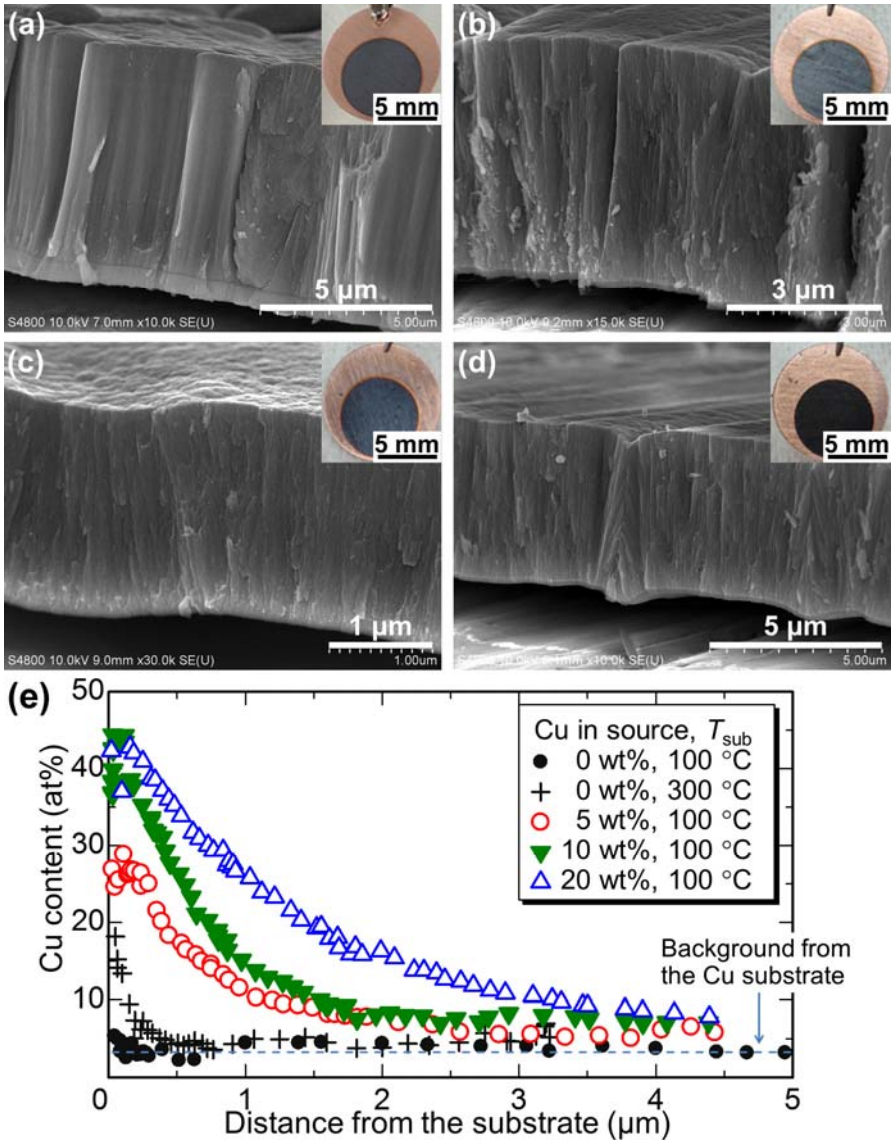

Figure 3-3 Cross-sectional SEM images and photographs (inset) of (a) a Si film (t_{act} ≈ 6.7 μm at the centre of the film, ρ_{film} ≈ 1.54 g cm^{-3}) prepared with a pure Si source, and of Si–Cu films prepared using Si sources containing (b) 5 wt% Cu (t_{act} ≈ 4.9 μm, ρ_{film} ≈ 1.60 g cm^{-3}), (c) 10 wt% Cu (t_{act} ≈ 2.3 μm, ρ_{film} ≈ 1.67 g cm^{-3}), and (d) 20 wt% Cu (t_{act} ≈ 4.5 μm, ρ_{film} ≈ 1.82 g cm^{-3}). All samples were prepared at T_{sub} = 100 °C without post-annealing. (e) Depth profiles of the elemental compositions of the pure Si films and the Si–Cu films as measured by SEM-EDX. The standard deviation was 1–3% of the intensity (Cu content value) and 0.2–0.4 at% as the Cu content value (see Figure 3-4). These films showed detachment from the Cu substrate upon bending because post-annealing treatments were not applied to the samples. The ~3 at% Cu signal is a background signal from the Cu plate for all measurements (see Figure 3-5).

had a mass density (ρ_{film}) of 1.54 g cm^{-3}, and its porosity (P_{film}) was calculated to be 0.33 using the following equation: $P_{film} = 1 - \rho_{film}/\rho_{Si}$. The mass densities of the films increased from 1.60, to 1.67, to 1.82 g cm^{-3} with increasing Cu content (5, 10, and 20 wt%, respectively) in the Si source. Using the mass density of bulk Si (ρ_{Si} = 2.33 g cm^{-3}), the respective porosities of these films were calculated to be 0.31, 0.28, and 0.21; however, their actual porosities should be higher because the bulk Si–Cu alloys have increasing mass densities with increasing Cu content.

Elemental composition of these films were analysed by SEM-EDX at ~50 points for each sample as shown in Figure 3-4 and summarized in a graph of the composition profiles (Figure 3-3e). The graph

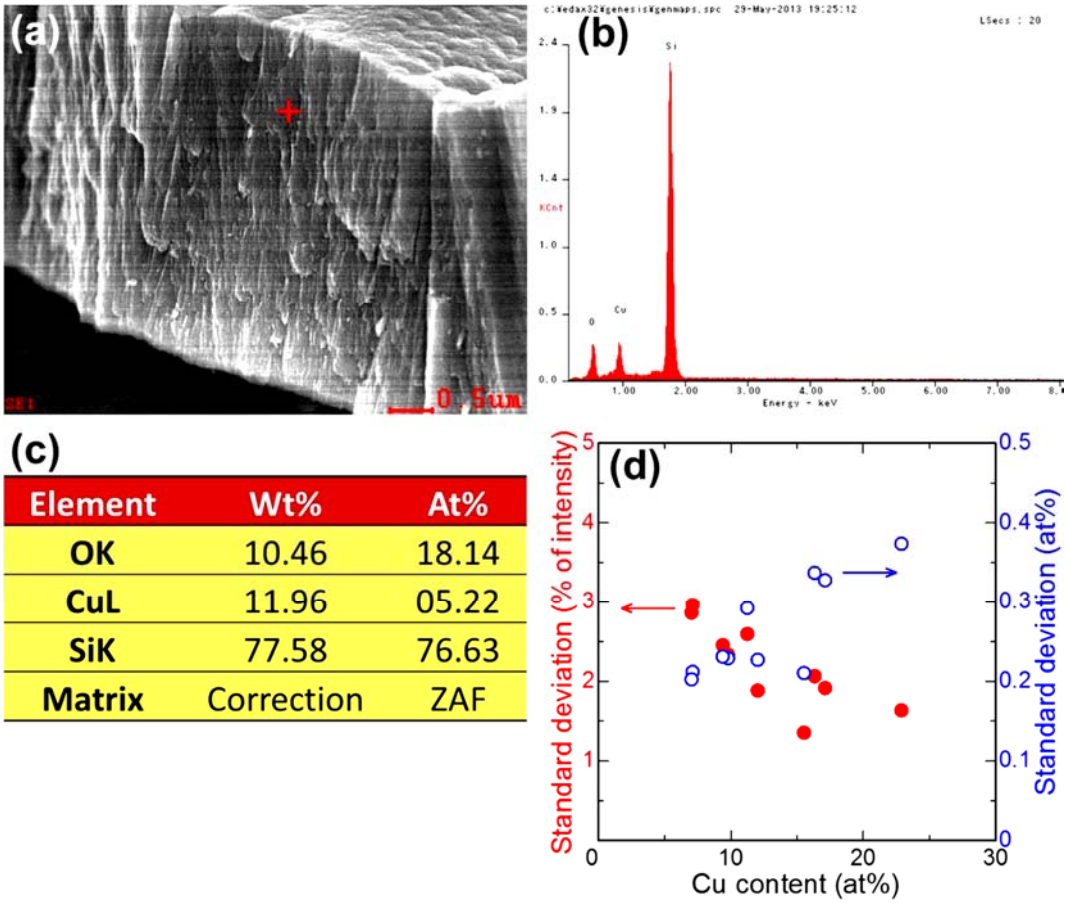

Figure 3-4 Typical SEM-EDX result for a point-measurement of the cross-section of the Si–Cu film (5 wt% cu source, T_{sub} = 100 °C, without post-annealing). This kind of measurement was made for ~50 different points at various distances from the interface to make a profile for each sample in Figure 3-3e. Standard deviation of the Cu content values is shown in (d) for the film from 5 wt% Cu source.

clearly demonstrated the Cu concentration gradient in the direction perpendicular to the Cu substrate. The Si film that was deposited at T_{sub} = 100 °C showed minimal intermixing of Si with Cu, while the

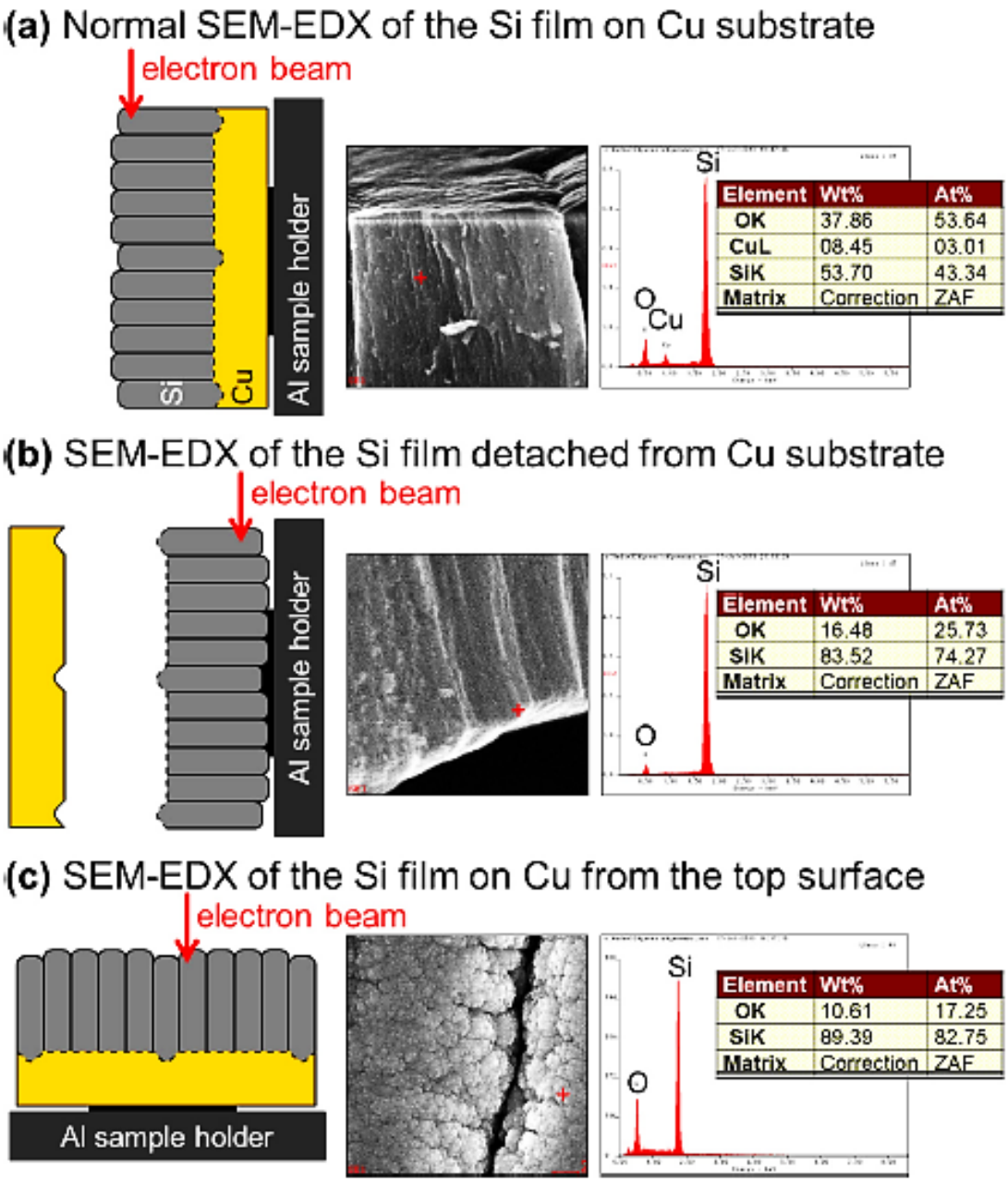

Figure 3-5 SEM-EDX measurements examining the background signal from the Cu substrate. The sample was a pure Si film deposited at T_{sub} = 100 °C without post-annealing. The point measurement detected Cu at ~3 at% for the top position of the cross-section of the Si film on the Cu substrate. Whereas no Cu was detected for the top position of the cross-section of the Si film detached from the Cu substrate and for the top surface of the Si film on the Cu substrate.

film that was deposited at T_{sub} = 300 °C showed a thin intermixed layer of 0.1–0.2 μm, which is consistent with the results of our previous report [116]. A higher deposition temperature (T_{sub} = 500 °C) can yield a thicker intermixed layer but containing a mixed amorphous-microcrystalline phase with small porosity, which resulted in poor cycle performance [116]. In contrast, the co-deposited Si–Cu films showed a much thicker compositional gradient layer; ≥ 5 at% for ≤2 μm from the interface and 2–3 at% for the entire thickness range of 4.5-μm-thick films without the need to increase T_{sub}. The Cu content of the gradient layer can also easily be increased to ~40 at% by increasing the Cu content of the source.

3.4 Crystallinity and lithiation behavior of porous Si–Cu films

To enhance the adhesion of the Si and Si–Cu films with the Cu substrate, post-annealing was performed at T_{an} = 600 °C. The high-magnification cross-sectional SEM images of the films at the interface with the Cu substrates clearly show the significant improvements in the adhesion compared with the as-deposited films (Figure 3-3); the gap was very small for the pure Si film (Figure 3-6a) and was eliminated for the Si–Cu films (figure 3-6b–d). Nitrogen adsorption measurement was also performed for the Si–Cu film deposited using a 5 wt% Cu source. It showed that the Si–Cu film had a specific surface area as high as 95.8 $m^2\ g_{film}^{-1}$ (Figure 3-6f) and pore volume as high as 0.237 $cm^3\ g_{film}^{-1}$ (Figure 3-6g). When we use the mass density of Si (2.33 g cm^{-3}), 1 g of the Si–Cu film has 0.429 cm^3 solid with 0.237 cm3 pore, resulting in porosity of 0.356, which is closed to the porosity value (0.31) estimated using the mass density of the film (1.60 g cm^{-3}) for the as-deposited film.

The crystallinity of the Si-base films is one of the most significant factors to affect the electrochemical performance, and causes different lithiation behaviour at the initial cycle. We previously reported a

change in the crystallinity of pure Si films with T_{sub} [116]; deposition at low T_{sub} values of 100 and 300 °C yielded Si films with a purely amorphous phase that did not crystallize upon post-annealing

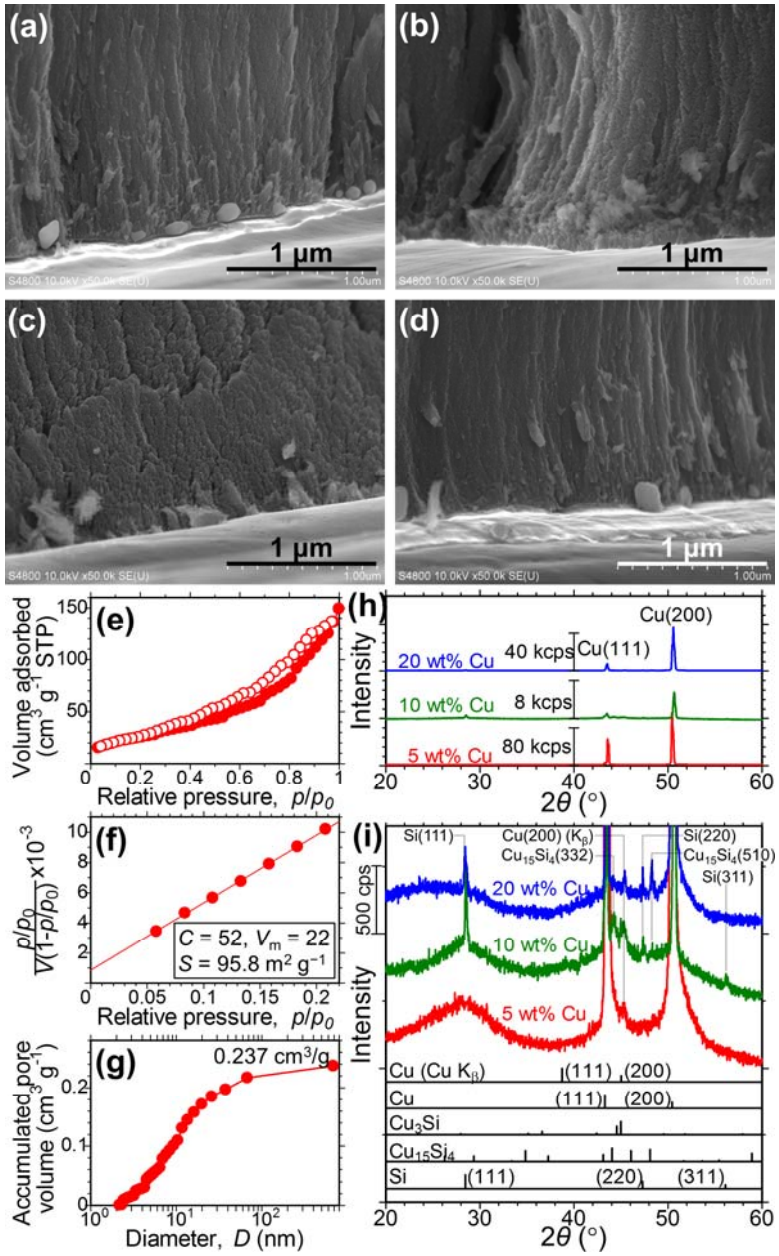

Figure 3-6 Structure analysis of the Si–Cu films deposited on cu substrates at T_{sub} = 100 °C and post-annealed at T_{an} = 600 °C. Cross-sectional SEM images at the interface between the Cu substrates and Si–Cu films made with (a) pure Si source, (b) 5 wt% Cu source, (c) 10 wt% Cu source, and (d) 20 wt% cu source. BET analysis of the Si–Cu films deposited on a 10 μm-thick Cu foil at T_{sub} = 100 °C and post-annealed at T_{an} = 600 °C; (e) N_2 adsorption isotherm, (f) BET plot, and (g) pore size distribution. XRD patterns of Si–Cu films deposited at T_{sub} = 100 °C and post-annealed at T_{an} = 600 °C; in full intensity scales (h) and a magnified intensity scale (i).

at T_{an} = 600 °C, while deposition at the high T_{sub} of 500 °C yielded Si films with a mixed amorphous and microcrystalline phase. The solid phase crystallization of amorphous Si (a-Si) is known to occur upon annealing at temperatures ≥700 °C for 10 min or more [100], but it does so more easily in coexistence with a metal, which is known as metal-induced crystallization [119-123]. I therefore analysed Si–Cu samples that had been post-annealed at T_{an} = 600 °C by XRD (Figure 3-6h and i). From the spectra for full y-axis range (Figure 3-6h), we can see that the Cu substrates had (200) out-of-plane orientation. The film from 5 wt% cu source showed a broad peak of a-Si at ~29° [124], in addition to the intense Cu (111) and (200) peaks at 43.3° and 50.4°, respectively. Because of the strong (200) orientation of the cu substrate, we can also see its diffraction at 45.0° due to the weak Cu K_β line. The film from 10 wt% cu source showed the sharpened peak of a-Si at ~29° with a strong Si (111) peak, showing the partial crystallization of a-Si. In addition to the above-mentioned peaks from the Cu substrate at 43.3°, 45.0° and 50.4°, the film had peaks of $Cu_{15}Si_4$ (332) at 44.1° [123, 125], Si (220) at 47.3° and Si (311) at 56.1° [124]. The film from 20 wt% Cu source showed similar spectrum with that from 10 wt% cu source with some differences; the broad peak of a-Si at ~29° got weakened, the $Cu_{15}Si_4$ (510) peak at 48.1° got pronounced, and the Si (311) peak at 56.1° got less obvious. In the standard powder pattern, Cu_3Si has intense diffractions by the (012) and (300) planes at 44.6° and 45.0° with relative intensities of 64 and 100, respectively [123, 125]. We attribute the peak at 45.0° to the Cu (200) diffraction of the Cu K_β line for the film from 5 wt% Cu source, which show no other diffraction except for those from the Cu substrate, but the Cu_3Si (012) and (300) peaks may overlap with it for the films from 10 to 20 wt% Cu sources. From these analysis, we can conclude that the film from 5 wt% cu source was fully amorphous and that the films from 10 wt% and 20 wt% cu sources were partially crystallized with c-Si and crystalline copper silicide phases (with c-$Cu_{15}Si_4$ phase, at least). Next, I examined the electrochemical performances of the Si–Cu films via galvanostatic charge–discharge measurements using three-electrode beaker cells. First, the

performance was evaluated using an electrolyte of 1 M $LiPF_6$ in EC/diethyl carbonate (1:1 v/v); however, all the Si and Si–Cu films showed poor cycle performances (Figure 3-7). Hydrofluoric acid possibly formed because of insufficient removal of oxygen/water and the excess amounts of the electrolyte used in the beaker cells, which resulted in the etching and delamination of the films. Therefore, I subsequently used 1 M $LiClO_4$ in EC/PC (1:1 v/v) as the electrolyte.

Figure 3-8 shows the lithiation/delithiation behaviour of these films over the first two cycles measured at a rate of 0.1*C*. Note that the rate is calculated by assuming 100% Si content, and thus the actual rate is higher than 0.1*C* for the Si–Cu films. In the case of the Si–Cu film with the lowest Cu content (5 wt% Cu source), the first plateau appeared at ~200 mV *vs.* Li/Li^+ during lithiation, which

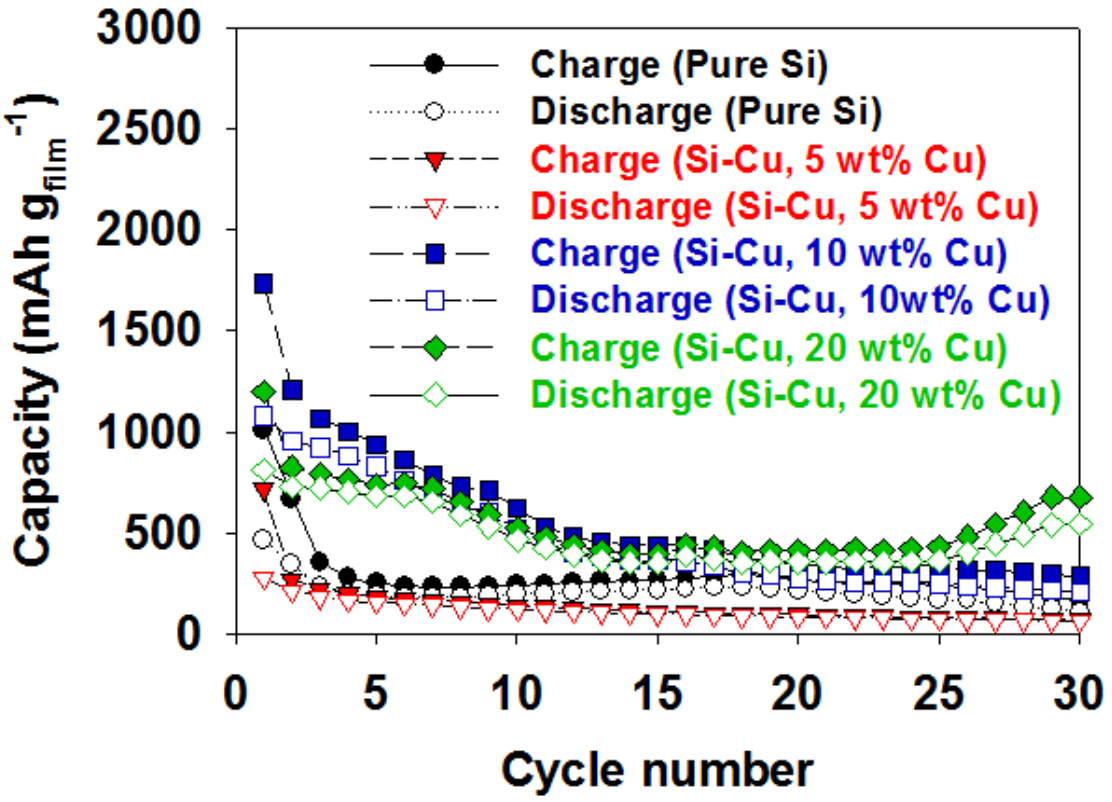

Figure 3-7 Electrochemical performance of pure Si and Si–Cu films using lithium hexafluorophosphate ($LiPF_6$, 1 M) in a 1:1 (v/v) mixture of EC and diethyl carbonate as the electrolyte with H_2O content of less than 20 ppm (Kishida Chemical, Osaka, Japan)

corresponds to the lithiation potential of a-Si (Figure 3-8a), while the Si–Cu films with higher Cu content (10 and 20 wt% Cu sources) showed plateaus at ~150 mV (Figure 3-8b) and ~100 mV (Figure 3-8c), respectively, because of partial crystallization of the Si–Cu films (Figure 3-6i). It is known that the initial lithiation of c-Si generally occurs at ~100 mV, which corresponds to the conversion of c-Si to a-Li_xSi (x~3.5) [66, 68, 126], while a-Si converts into a-Li_xSi (x=0–2.0) at ~200 mV, and then converts further into a-Li_xSi (x=2.0–3.5) at ~100 mV [66, 67, 127-130].

Figure 3-8d–g shows differential capacity curves of the Si–Cu films that were derived from the

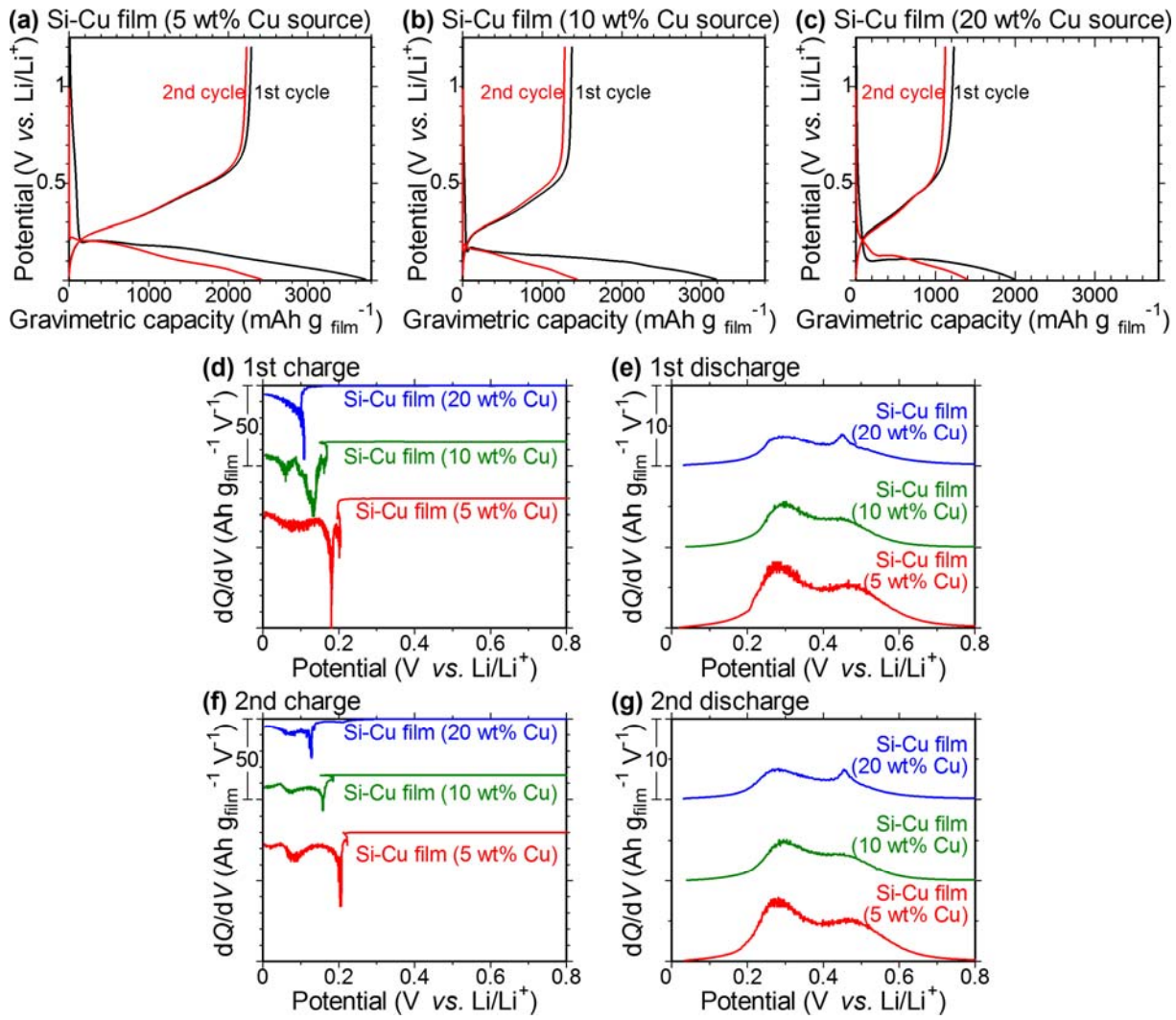

Figure 3-8 Voltage-capacity profiles of Si–Cu films with (a) 5 wt% Cu source (t_{eff} = 3.3 µm), (b) 10 wt% Cu source (t_{eff} = 3.4 µm), and (c) 20 wt% Cu source (t_{eff} = 3.1 µm) for the first and second cycles measured at a rate of 0.1*C*. (d–g) Differential capacity curves derived from the voltage-capacity profiles shown in parts (a–c).

voltage-capacity profiles (Figure 3-8a–c). During the first charging process (Figure 3-8d), the Si–Cu film with the low Cu content (5 wt% Cu source) showed three peaks; small and dominant sharp peaks at ~200 and ~180 mV, respectively, and another broad peak at ~90 mV, which correspond to potentials forming a-$Li_{2.0}Si$, a-$Li_{3.5}Si$, and a-$Li_{3.75}Si$, respectively [70, 87, 130, 131]. The Si–Cu film with moderate Cu content (10 wt% Cu source) also showed three different peaks, which shifted to lower potentials of ~160, ~130 and ~70 mV. In contrast, the Si–Cu film with the highest Cu content (20 wt% Cu source) showed one dominant peak at ~100 mV, which was similar to the lithiation behaviour of c-Si [87]. During the first discharge process (Figure 3-8e), all the Si–Cu films exhibited the same initial delithiation peak at ~270 mV, which corresponds to the transformation of a-$Li_{3.5}Si$ into a-$Li_{2.0}Si$. A difference was found at the second delithiation peak, where the Si–Cu films with the lowest and moderate Cu contents (5 and 10 wt% Cu sources) both exhibited a broad peak in the 400–500 mV range, corresponding to the transformation of a-$Li_{2.0}Si$ into a-Si [68, 70], while that with the highest Cu content (20 wt% Cu source) showed a sharp peak at ~450 mV, corresponding to the transformation of c-$Li_{3.75+\delta}Si$ into a-Li_xSi [68, 131]. In the second charging process (Figure 3-8f), the lithiation potentials shifted to higher potentials in all the Si–Cu films, which is possibly due in part to the conversion of c-Si to a-Si during the first charge–discharge process. Little change was found in the second discharge process (Figure 3-8g) when compared with the first discharge process (Figure 3-8e). The dominant first peak at ~270 mV appeared for all films, with the broad second peak at 400–500 mV for the Si–Cu films with the lowest and moderate Cu contents (5 and 10 wt% Cu sources) and the sharp second peak occurred at ~450 mV for the Si–Cu film with the highest Cu content (20 wt% Cu source). The high Cu content of the film may have inhibited complete lithiation of Si in the initial cycles, and thus c-Si content possibly remained in this film for at least the first two cycles.

3.5 Cycle performance of porous Si–Cu anodes

Figure 3-9 shows the electrochemical behaviour of the Si and Si–Cu films. The initial charge and discharge capacities of the pure Si film reached 3625 and 2520 mAh g_{film}^{-1}, respectively (Figure 3-9a). The large irreversible capacity is attributed to Si consumption during the formation of the solid electrolyte interphase (SEI), which was significant because of the large exposed surface of the porous Si film. The Coulombic efficiency increased to 98% after 20 cycles, but then dropped abruptly at the 30th cycle (Figure 3-9b). This occurs because the Si film begins to peel off the Cu substrate because of the large volume change during the charge–discharge cycles. Finally, the discharge capacity at the 50th cycle decreased to ~500 mAh g_{film}^{-1}. These performances were worse when compared with the results of our previous report [116], which were a Coulombic efficiency of ~99.5% and a discharge capacity of ~1000 mAh g_{film}^{-1} at the 50th cycle. This difference originated from the different cell structure (coin cells) and electrolyte (1 M LiPF6 in a 1:1:1 (v/v) mixture of EC, DMC, and ethyl methyl carbonate) that were used in the previous work. In contrast, the small addition of 5 wt% Cu to the Si source yielded a Si–Cu film with remarkably enhanced cycle performance. The film exhibited a high initial charge capacity of 3425 mAh g_{film}^{-1} with a discharge capacity of 2073 mAh g_{film}^{-1} (Figure 3-9a). The capacity retention of this film was the highest among all the films examined, at 73% and 60% with discharge capacities of 1518 and 1250 mAh g_{film}^{-1} at the 50th and 100th cycles, respectively. The Coulombic efficiency exceeded 98% at the 10th cycle and remained stable at ~99% for 100 cycles. These values are much higher than that of the pure Si film, possibly because of the gradient volume expansion of the Si–Cu film in the direction perpendicular to the Cu substrate. Further increases in the Cu content of the Si source to 10 and 20 wt%, however, resulted in poorer performance levels with lower initial charge and discharge capacities, Coulombic efficiencies, and capacity retention. This is because of the partial crystallization of the Si–Cu films (Figure 3-6i) and the inhibited lithiation (Figure 3-8) for those with higher Cu contents.

The volumetric capacity (mAh cm_{film}^{-3}) and the areal capacity (mAh cm_{anode}^{-2}) (shown as inset of Figure 3-9a) of the films are highly important factors for practical battery devices. The volumetric

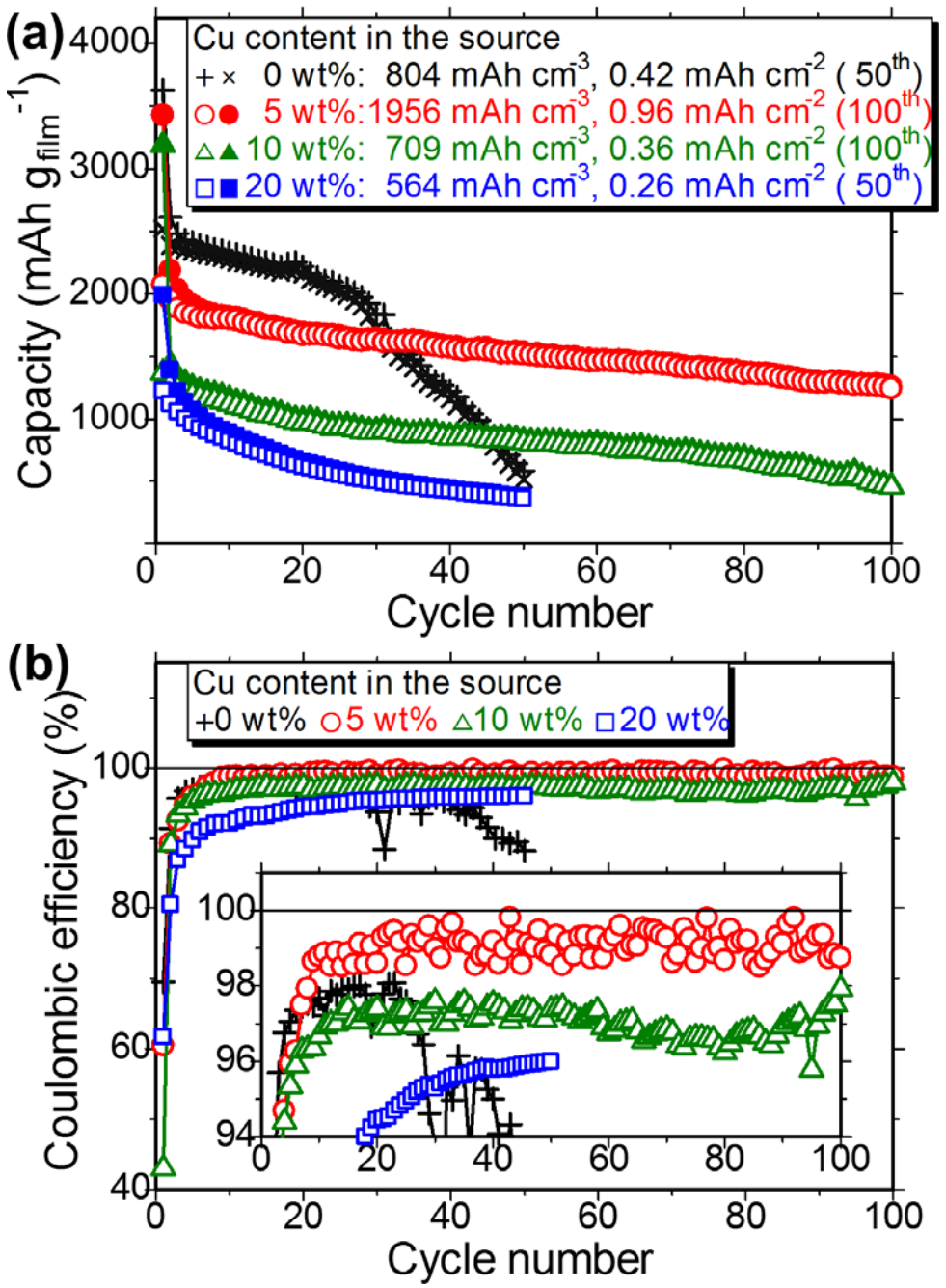

Figure 3-9 Electrochemical performance of pure Si and Si–Cu films deposited at T_{sub} = 100 °C and post-annealed at T_{an} = 600 °C. t_{eff} = 3.5, 3.3, 3.4, and 3.1 μm for films from Si sources with 0, 5, 10, and 20 wt% of Cu, respectively. The cycle performance at 0.1*C* was expressed as gravimetric capacity (a) with volumetric capacity and areal capacity values as inset. (b) Coulombic efficiency of the films. Cycle tests were performed at 0.1*C* for all cycles (1–100).

capacity of the Si–Cu film (5 wt% Cu source) was 1956 mAh cm_{film}^{-3} after 100 cycles, which is much higher than that of commercial graphite anodes. The areal capacity of the Si–Cu film (5 wt% Cu source) was 0.96 mAh cm_{anode}^{-2}, which is higher than previously reported values for Si nanomaterials (0.2–0.4 mAh cm_{anode}^{-2} [79, 88]) and porous Si films by ourselves (0.66 mAh cm_{anode}^{-2} [116]), but is still smaller than that of commercial graphite anodes (~4 mAh cm_{anode}^{-2}, 18650 Li-ion cells, Sony, Japan) [112] and Si–carbon nanotube hybrid anodes (2 mAh cm_{anode}^{-2}) [113]. The cycle performance of the pure Si film in this work is smaller than that in our previous work [116], which is possibly because of differences in the measurement method, and thus the Si–Cu film from the 5 wt% Cu source may perform better in a coin cell test and/or electrolyte of 1 M LiPF6 in a 1:1:1 (v/v) mixture of EC, DMC, and ethyl methyl carbonate. The Si–Cu film (5 wt% Cu source) showed very stable Coulombic efficiency of ~99% for 10–100 cycles, indicating the formation of stable SEI layer and/or efficient use of Si in the film from the early cycles. The Si–Cu film (10 wt% Cu source) showed lower values of 97% for the first 50 cycles, and fluctuating values in the 96%–98% range for the later cycles. The Si–Cu film (20wt% Cu source) showed a very low initial value, which increased to >94% after 20 cycles. These values lower than 100% indicate the continuous formation of SEI layer due to the incomplete formation of stable SEI layer in the early cycles. And some fraction of the Si in the films may not have reacted in the early cycles, as can be seen in the small initial charge capacity of 1992 mAh g_{film}^{-1} (Figure 3-9a) and in the low potential for lithiation (Figure 3-7), and then gradually began to react with the increasing number of cycles. High Cu contents inhibited the formation of stable SEI layer and/or the reaction of Si with Li+.

The Si–Cu film made using 5 wt% Cu in the Si source showed the best cycle performance and I therefore examined its rate performance (Figure 3-10). Beginning with the 0.1*C* rate, the Si–Cu film showed an initial discharge capacity of 2065 mAh g_{film}^{-1}, and a reduced capacity of 1755 mAh g_{film}^{-1} after 10 cycles with a Coulombic efficiency of ~97%. When the charge–discharge rate was doubled

to 0.2*C* from the beginning of the 11th cycle, the Coulombic efficiency dropped slightly to 95%, but immediately increased to ~98% at the 12th cycle, and that efficiency was maintained with a reduced discharge capacity of 1485 mAh g_{film}^{-1} at the 20th cycle. Similar changes were observed for later cycles, where the Coulombic efficiency dropped slightly upon an increase in the charge–discharge

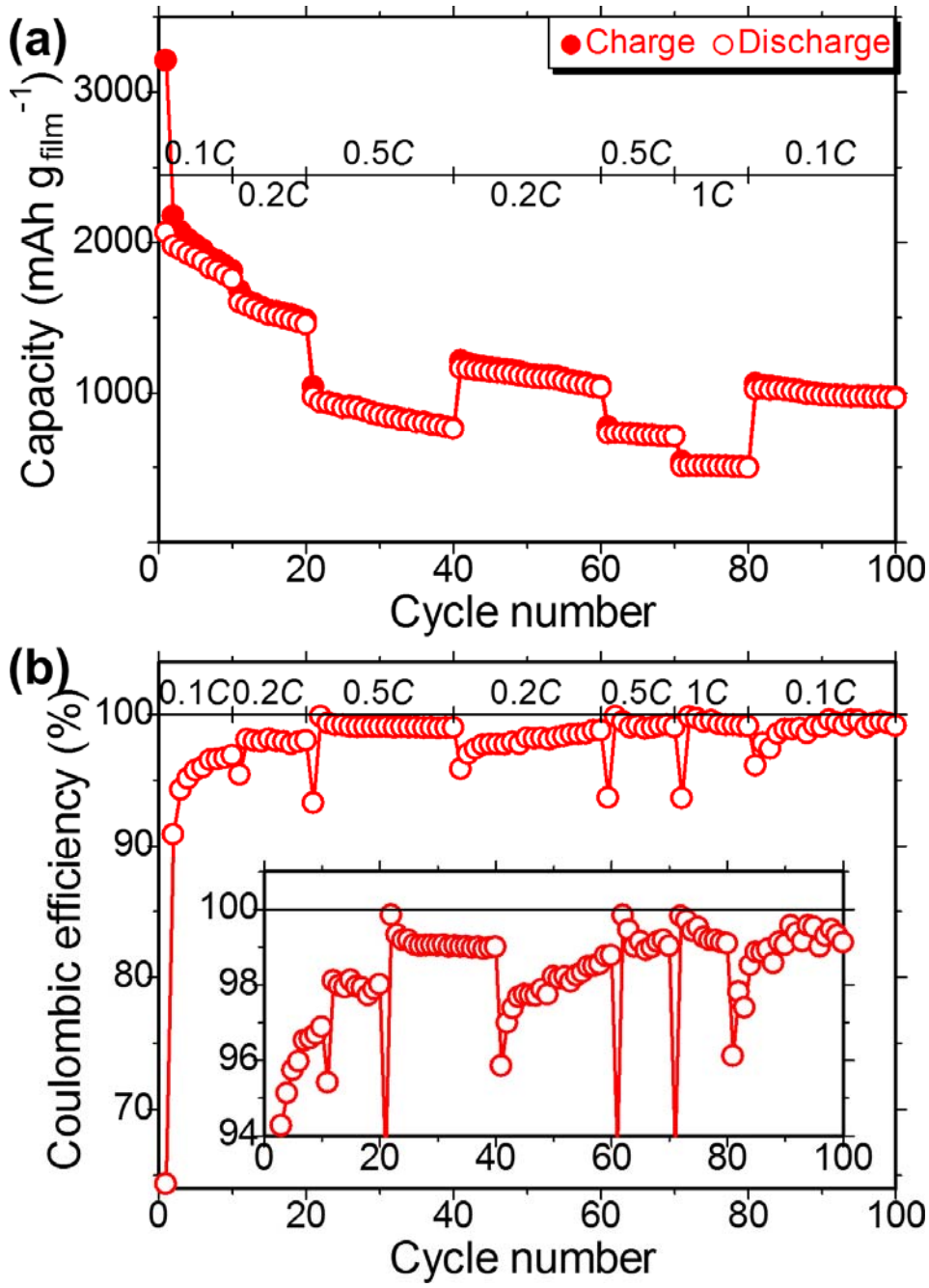

Figure 3-10 (a) Rate capability of representative Si–Cu film (t_{eff} = 3.3 µm, 5 wt% Cu source, T_{sub} = 100 °C, T_{an} = 600 °C). (b) Coulombic efficiency and (c) capacity ratio of charge at the [*n*+1]th cycle to discharge at the [*n*]th cycle as a function of cycle number *n*.

rate but immediately recovered in the next cycle, and maintained a steady value of 98–100% at 0.1*C*–1*C* rates for 100 cycles (Figure 3-10b). The discharge capacity decreased/increased upon any increase/decrease in the charge–discharge rate, with continuous gradual decay with increasing numbers of cycles. The discharge capacity decreased to 505 mAh g_{film}^{-1} at 1*C* at the 80th cycle and recovered to 964 mAh g_{film}^{-1} at 0.1*C* at the 100th cycle (Figure 3-10b). These results show that the stable SEI layer formed on this Si–Cu film and the Si in this film reacted efficiently with the Li^+ from the early cycles.

3.6 Cycle performance of porous Si–Cu anodes with different cut-off potentials for charge

Figure 3-11 shows the effects of the different cut-off potentials for charge on the electrochemical performances of the Si–Cu films at a rate of 0.1*C* for 50 cycles. When compared with the 5 mV cut-off, all films with the 100 mV cut-off showed reduced values for the initial charge capacities and reduced or similar values for the initial discharge capacities (Figure 3-11a–c, Figure 3-12a). The Si–Cu film with the lowest Cu content (5 wt% Cu source) showed little change in capacity retention, whereas the Si–Cu films with moderate and highest Cu contents (10 and 20 wt% Cu sources) showed remarkable increases in capacity retention of 6% and 28%, respectively (Figure 3-11d). These results show that the cut-off operation for charge (lithiation) helps the Si–Cu anodes that contain c-Si to increase their capacity retention during cycling, possibly by suppressing the phase transformation, while the cut-off operation does not help the a-Si–Cu anode without c-Si, possibly because of the absence of such a phase transformation, regardless of the cut-off potential. The areal capacities of the Si–Cu films (5, 10 and 20 wt% Cu sources) were 0.8, 0.7 and 0.5 mAh cm_{anode}^{-2}, respectively (Figure

3-12b), at the 50th cycle. The Coulombic efficiencies of the Si–Cu films (10 and 20 wt% Cu sources)

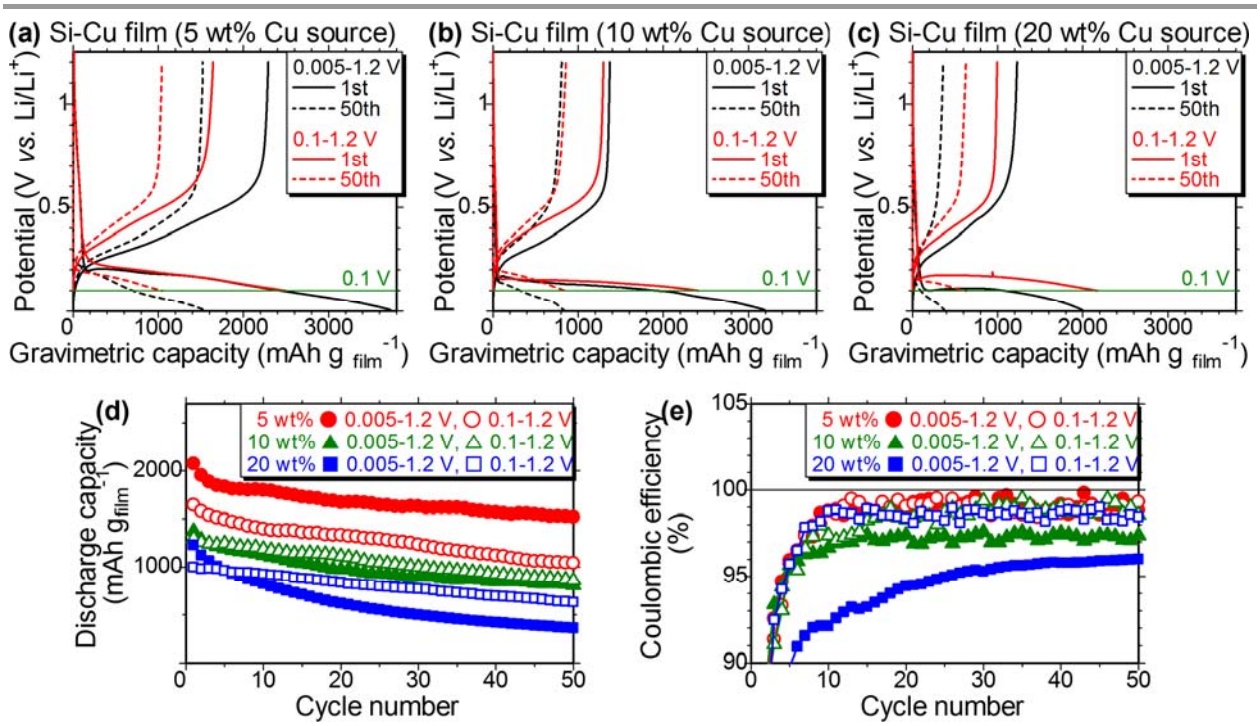

Figure 3-11 Voltage-capacity curves for the first and 50th charge/discharge cycles of Si–Cu films deposited using sources with (a) 5 wt% Cu (t_{eff} = 3.3 µm), (b) 10 wt% Cu (t_{eff} = 3.5 µm), and (c) 20 wt% Cu (t_{eff} = 3.2 µm) with different cut-off operations at 5 and 100 mV for charge. (d) Cycle performance and (e) Coulombic efficiency of the Si–Cu films. The Si–Cu films were deposited at T_{sub} = 100 °C and post-annealed at T_{an} = 600 °C.

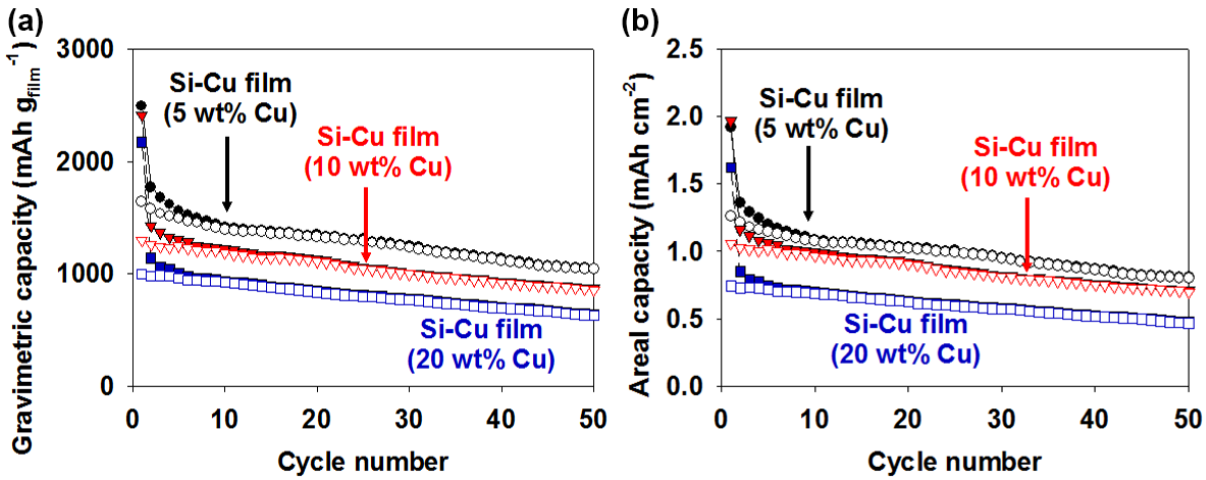

Figure 3-12 Electrochemical performance of Si–Cu films with 100 mV cut-off potential for charge. The Si–Cu films were deposited using Si sources with different Cu contents (5, 10 and 20 wt%) at T_{sub} = 100 °C, post-annealed at T_{an} = 600 °C, and had t_{eff} = 3.3, 3.5 and 3.2 µm, respectively. (a) Gravimetric capacity and (b) areal capacity of the deposited Si–Cu films.

increased to more than 95% after the fifth cycle, and remained at ~99% for 50 cycles, which are similar values to the efficiencies of the Si–Cu films with the lowest Cu content (5 wt% Cu source) with both 5 and 100 mV cut-offs (Figure 3-11e).

3.7 Failure behavior of pure Si and Si–Cu films after charge–discharge cycles

Figure 3-13 shows top-view SEM images of the pure Si and Si–Cu films before and after 100 cycles. Both films initially had similar morphologies with wall-shaped structures (Figure 3-13a and c), but the pure Si film was completely pulverized into a few μm-sized particles, and peeled off after 100 cycles. This occurred because of large-scale volume change of the pure Si film and its poor adhesion to the Cu substrate. At the region where the Si film was peeling off, SEM-EDX analysis detected Si and Cu at 1.1 and 74.4 at%, respectively, indicating the delamination at the interface between the Si film and the Cu substrate (Figure 3-13e). In contrast, the Si–Cu film (5 wt% Cu source) had square domains with ordered domain boundaries at a pitch of 10–20 μm in one direction, with random domain boundaries in a direction that was roughly perpendicular to the former direction. The ordered domain boundaries apparently originated from the wall-shaped structure found in the as-deposited film (Figure 3-1a), which in turn originated from the stripe patterns on the as-received Cu substrates. Also, the domains contained numerous small cracks. Such a structure could possibly show reversible expansion and shrinkage for 100 cycles without pulverization. The similar results were obtained for the Si–Cu films using 10 and 20 wt% cu source (Figure 3-14); the films retained mostly attached to the Cu substrate with square domains. The Si–Cu films were delaminated in some areas but mostly remained attached to the Cu substrate (Figure 3-13d), possibly because of the gradient volume expansion of the Si–Cu films with gradient composition profiles and because of stress defocusing on the diffuse interface between the Si–Cu film and the Cu substrate. In the region where the Si–Cu film

was being delaminated, SEM-EDX detected Si and Cu at 15.6 and 40.7 at%, respectively, which indicated that the delamination occurred not at the interface but in the film itself (Figure 3-13f).

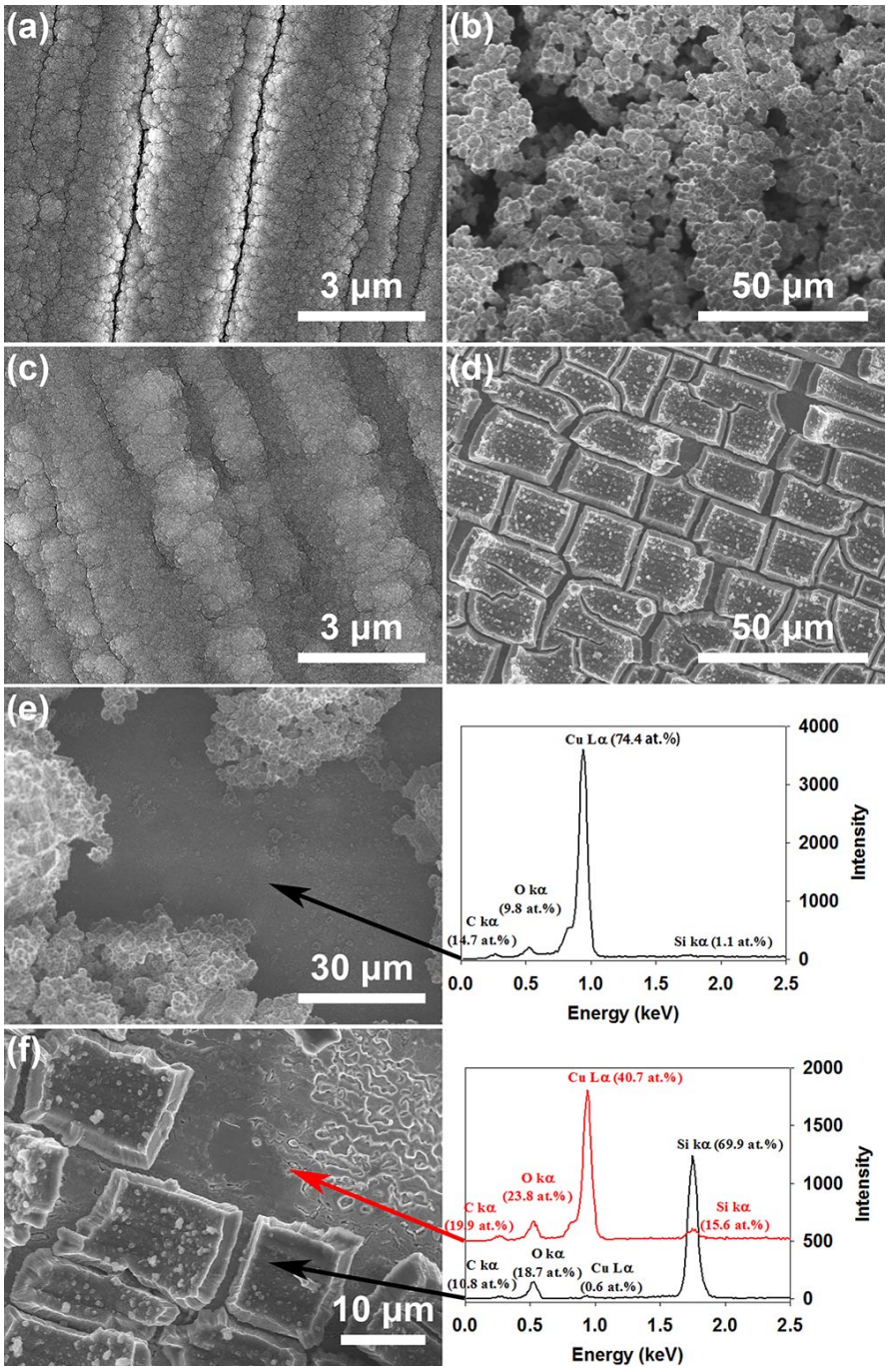

Figure 3-13 Top-view SEM images of the pure Si film (t_{eff} = 3.3 μm) (a,b) and the Si–Cu film (5 wt% Cu source, t_{eff} = 3.3 μm) (c,d) before cycles (a,c) and after (b,d) the 100th discharge. Cycles were performed at 0.1*C* charge/discharge rates. Both films were deposited at T_{sub} = 100 °C and post-annealed at T_{an} = 600 °C. SEM-EDX analysis results for the pure Si film (e) and the Si–Cu film (f) after the 100th discharge.

In order to understand the underlying mechanism for the cycle performances, electrochemical impedance spectroscopy was performed for a pure Si film and Si–Cu films (Figure 3-15). The very high frequency region (above 126 kHz) corresponds to the sum of the solution resistance, resistance at the film/Cu interface and external circuits [132], and the degradation of electrolyte can be neglected here due to the huge amount of electrolyte in the beaker cell. For the pure Si film, this resistance increased continuously during cycles, corresponding to the continuous detachment of the film from the Cu substrate. For the Si–Cu films (5 and 20 wt% Cu), on the other hand, this resistance showed very small increase due to the better adhesion at the film/Cu interface as shown in Figure 3-

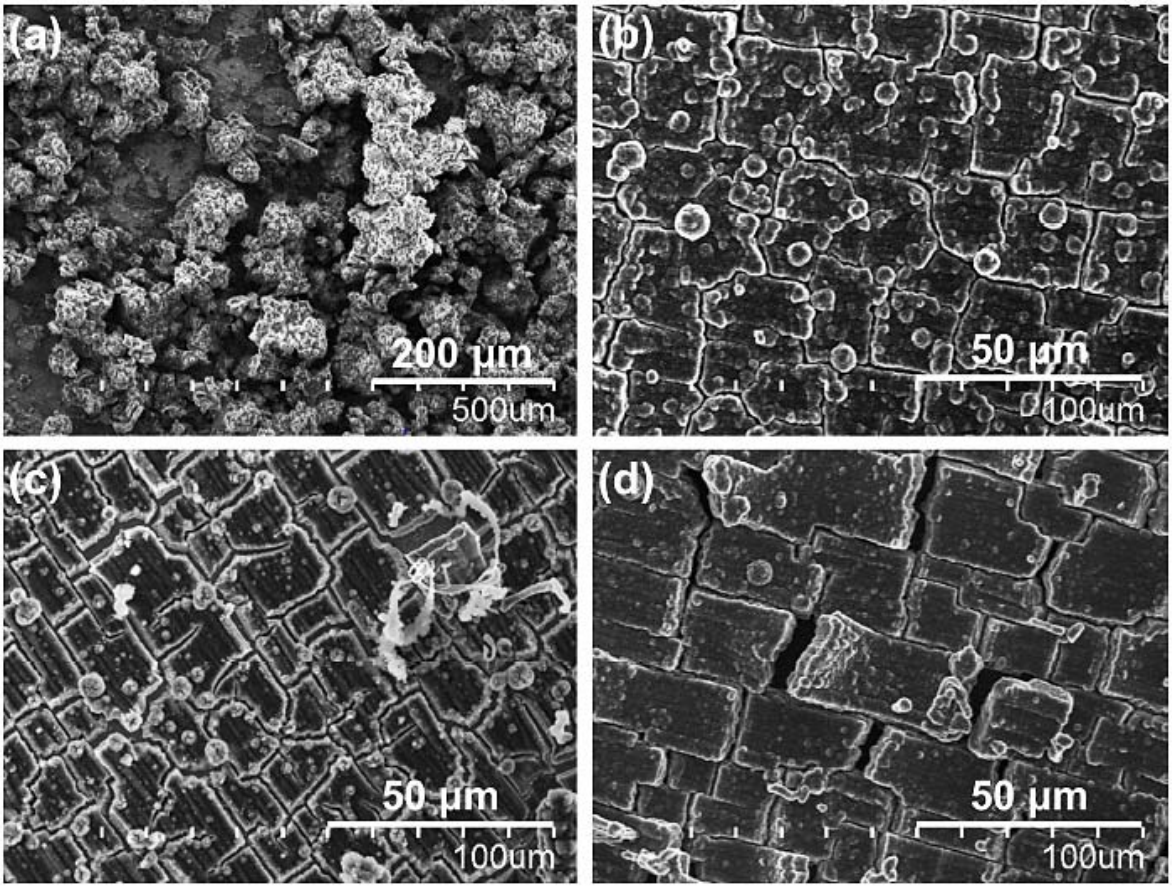

Figure 3-14 Top-view SEM images of the Si and Si–Cu films after the 100th discharge. The films were deposited at T_{sub} = 100 °C using (a) a pure Si source and (b) 5 wt%, (c) 10 wt%, and (d) 20 wt% Cu sources and post annealed at T_{an} = 600 °C. The cycles were performed at 0.3*C* except for the 1st, 25th, 75th and 100th cycles. The films (a, b, d) were charged at 0.1*C*, measured by impedance test, and discharged at 0.1*C* at the 1st, 25th, 75th and 100th cycles.

13 and Figure 3-14. Two semicircles at high and medium frequency range (126 kHz–0.5 Hz) were clearly observed. The small semicircle at high frequency and the large semicircle at middle frequency are attributed to the surface film resistance and charge transfer resistance, respectively [132]. The

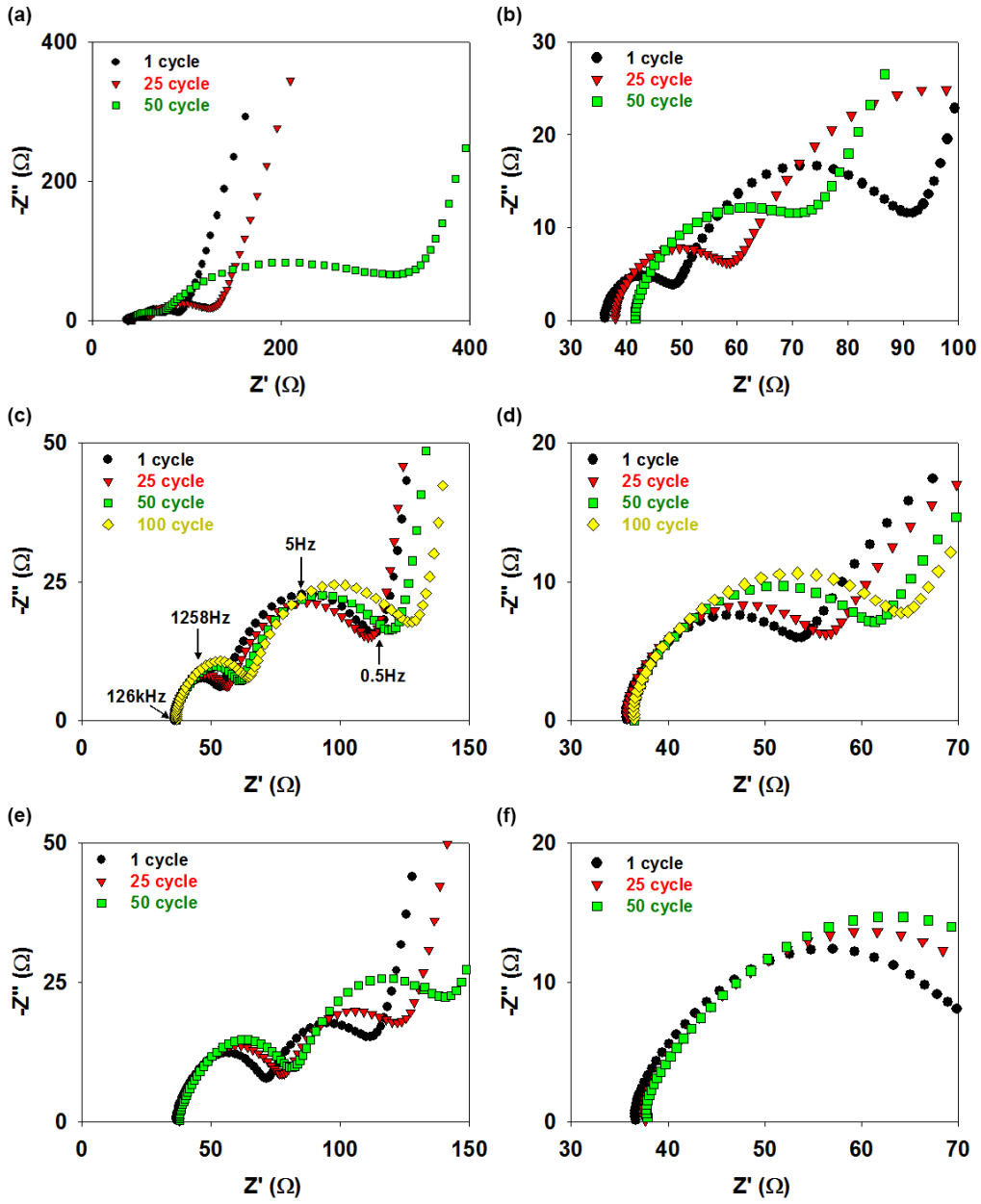

Figure 3-15 Nyquist plots of the (a, b) pure Si films (t_{eff} ~ 3.3 μm) and the Si–Cu films deposited using (c, d) 5 wt% Cu (t_{eff} ~ 3.4 μm) and (e, f) 20 wt% Cu (t_{eff} ~ 3.4 μm) at different cycles. All the films were deposited at T_{sub} = 100 °C and post-annealed at T_{an} = 600 °C. Cycles were performed at 0.3C except for the 1st, 25th, 50th, and 100th cycles. Impedance measurements were made after the 1st, 25th, 50th, and 100th charge; as soon as potential reached 5 mV during lithiation, the films were left at open circuit voltage for 30 min, and then impedance measurement was performed between 1 MHz and 5 mHz.

surface film resistance of the pure Si films increased quickly, suggesting the continuous formation of the SEI layer possibly due to its fracture (as can be seen in the pulverized Si film at the 100th cycle in Figure 3-13b) and its regeneration at the newly exposed Si surface. The surface film resistance remained smallest for the Si–Cu film (5 wt%) while somewhat larger for the Si–Cu film (20 wt%). As the dQ/dV analysis (Figure 3-8) showed, lithiation proceeded at lower potential for the Si–Cu film (20 wt%) than the Si–Cu film (5 wt%), resulting in the longer period at low potential and thus in the possible enhancement in the SEI layer formation in the former. The charge transfer resistance of the pure Si film increased significantly in 50 cycles, indicating that the Si film got more and more resistive during the cycles, which will be related with the pulverization of the pure Si film (Figure 3-13b). The Si–Cu film (20 wt%) had the smallest charge transfer resistance at the early cycles, possibly due to the highest Cu content and lowest film resistivity, but the resistance increased continuously and approached to that of the Si–Cu film (5 wt%).

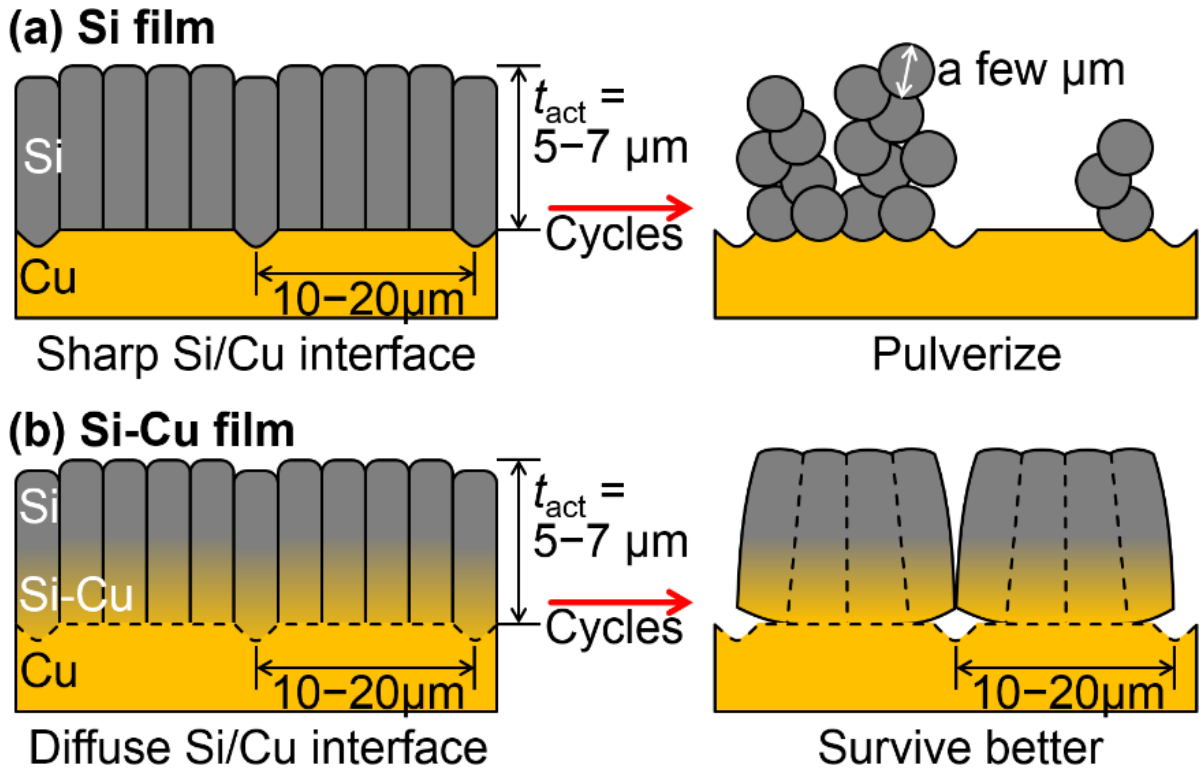

Figure 3-16 Schematic summarizing the initial structures of the porous Si and Si–Cu films and the final structures of these films after charge–discharge cycles.

Figure 3-16 schematically summarizes the initial structures of the pure Si and Si–Cu films and final structures after the charge–discharge cycles. The pure Si films showed pulverization and delamination from the Cu substrates due to the brittle nature of Si and clear difference in the volumetric change between the Si films (up to 400%) and Cu (0%) even with the porous and amorphous structure. They quickly lost electrical contact with the Cu substrates, resulting in rapid capacity fade and short lifetime. In contrast, the Si–Cu films had gradient composition profiles and diffuse interfaces with the Cu substrates, resulting in gradient volumetric expansion in the films and defocused stress at the interface. These Si–Cu films showed no pulverization and suppressed delamination, enabling them to survive for more cycles than the pure Si films. Although further improvements are needed, the gradient composition profile and the diffuse interface that formed spontaneously in the μm-thick Si–Cu film on the Cu current collector certainly enhanced the cycle performance of these Si-base anodes.

3.8 Conclusions

I have realized rapid deposition of 5–7-μm-thick porous Si–Cu films in 1 min on Cu current collectors by RVD using a mixed source of Si and Cu powders. Because of the preferential vaporization and deposition of Cu at the initial stage, which has a higher vapour pressure than Si, these films had 2–4.5-μm-thick composition gradient that changed from a Cu-rich region at the bottom to a Si-rich region at the top. The Cu content of the gradient layer was changed easily by varying the Cu content in the source. A porous structure was built into the Si–Cu films by keeping the substrate at a low temperature (T_{sub} = 100 °C), while the adhesion of the films to their substrates was improved by post-annealing at a higher temperature (T_{an} = 600 °C).

The resulting films were mostly amorphous in the low Cu content (5 wt% Cu source) case, whereas they were partially crystallized in the higher Cu content cases (10 and 20 wt% Cu source). The pure

Si film showed poor cycling performance with a discharge capacity of ~500 mAh g_{film}^{-1} at 0.1*C* at the 50th cycle, while Cu addition at even the smallest content (5 wt% Cu source) enhanced the film performance remarkably to 1518 and 1250 mAh g_{film}^{-1} at the 50th and 100th cycles, respectively. The Cu composition gradient in the film and the diffuse interface between the film and the Cu substrate possibly yielded the gradient volume expansion and the stress defocusing at the interface. The film had a 10–20-μm-sized square domain structure during cycling, which showed no pulverization and suppressed the delamination from the substrate. However, excess addition of Cu (10 and 20 wt% Cu sources) reduced the cycle performances of the Si–Cu films due to partial crystallization, inhibited Si lithiation, and inhibited formation of stable SEI layer. The increased cut-off potential for charge from 5 to 100 mV *vs.* Li/Li^+, improved the cycle performances of the Si–Cu films with higher Cu contents (10 and 20 wt% Cu sources) that contained some crystalline phases, but did not do so for the Si–Cu film with the lowest Cu content (5 wt% Cu source) that had a mostly amorphous phase.

The Si–Cu film with the lowest Cu content (5 wt% Cu source) showed a gravimetric capacity of 1250 mAh g_{film}^{-1}, a volumetric capacity of 1956 mAh cm_{film}^{-3}, and an areal capacity of 0.96 mAh cm_{anode}^{-2} at the 100th cycle. Although further improvement is required, this performance is encouraging for practical use of these Si-base anodes in lithium secondary batteries when we consider the quick and simple fabrication process for these Si–Cu films using inexpensive Si and Cu powder sources, along with the applicability of the RVD method to various substrates.

Chapter 4 – Carbon nanotubes (CNTs) and Si hybrid films as anodes in LiBs

4.1 Introduction

The micrometer-thick Si-Cu film, fabricated rapidly by Cu co-deposition with Si in RVD system, demonstrated that gradient Si–Cu layer can enhance the adhesion at the interface between Si(–Cu) layer and Cu current collector in spite of fairly large thickness (t_{eff} = 3–4 μm) with high packing density of ~1.5 g cm^{-3}. The films achieved enhanced electrochemical performance for 100 cycles compared with the pure Si film, as stated in Chapter 3. However, cycle stability for long cycles still remains a challenge because of highly dense Si-Cu films. It was reported that one-dimensional structure of Si, such as Si nanowires, on the other hand, was close to an ideal structure for improvement of electrochemical performance, but complicated process with expensive/explosive silane source used for nanowire makes the low-cost production difficult.

Since the discovery of CNTs [133], lots of efforts improving the performance of energy storage devices, such as electrochemical capacitors (ECs) and lithium ion batteries (LiBs), by using CNTs have been reported [134, 135]. Especially, CNTs have been used as an additive either in the anode or cathode for LiBs due to high theoretical conductivity over 5×10^5 S cm^{-1} at room temperature [136] and high aspect ratio, which enable CNTs to make a role of electron/hole pathway. The incorporation of CNTs as a conductive additive at a lower weight loading than conventional carbon black and

graphite presents that the use of CNTs could represent more than an order of magnitude reduction in additive mass [25, 137]. In addition, CNTs have the capability to be assembled free-standing carbon electrode in electrochemical application without any binder or current collector, or a physical support and sufficient electronic transport for high capacity anode materials like silicon or germanium [25].

Although further research is needed to solve the issues including high irreversible capacity [39, 40, 138], the use of CNTs in LiBs is attractive due to their flexibility as well as the effective diffusion of Li^+ ions into their porous matrix.

In this chapter, I designed the core-shell wall structure of CNT–Si hybrid film by depositing Si onto the standing walls of shrunk CNT arrays on Cu substrate. I designed such a hybrid film to make the best combination of rapid vapor deposition for Si fabrication and self-organized CNT structure. In Chapter 2, dense Si films deposited at higher substrate temperatures showed good initial performances due to their stability against oxidation in air and suppressed SEI formation but poor long-cycle performances due to the volumetric change during charge–discharge cycles. Thus I used the CNT walls as templates and deposited Si on them at high temperature to realize dense Si films on CNT walls while spaces for volume expansion between the walls. Moreover, in order to avoid the side reaction of CNTs against electrolyte, the vertical aligned CNTs were covered completely with Si by RVD.

4.2 Materials and methods

4.2.1 Synthesis of vertical aligned CNTs

Cu plates with 15 mm diameter and 0.5 mm thickness were used as substrates, cleaned by sonication in isopropanol for 10 min, and further exposed to UV-O_3 for 3 min to remove organic contaminants

on their surface, followed by annealing treatment under 4 vol% H_2/Ar at ambient pressure and 800 °C for 10 min. Synthesis of CNT arrays on Cu substrates were conducted by the collaborative researcher Mr. Nuri Na. The combination of 10 nm-thick Ta and 15 nm-thick TiN as diffusion barriers were deposited, followed by 4 nm-thick Fe or Co thin layers using a magnetron sputtering apparatus (MPS-2000HC2S, ULVAC, Chigasaki, Japan). Vertical-aligned CNT arrays were grown from Fe or Co catalyst particles and 0.2 Torr C_2H_2 at 700 °C for 5–10 min using chemical vapour deposition (CVD) method. The wall-shape structure of the vertical aligned CNTs was developed by a drop of ethanol (EtOH), which cause shrinkage of CNTs by surface tension during drying.

4.2.2 Fabrication of CNT–Si hybrid films

The CNT–Si hybrid films were fabricated by Si deposition on ethanol (EtOH)-treated and untreated CNTs on Cu substrates using RVD in 2 min. Si sources were prepared using the same procedures as previously stated in Chapter 2. The Si sources were heated by resistive heating of carbon boat under 0.1 Torr Ar to T_{boat} of 2000–2400 °C, while substrate was heated to T_{sub} of 400 °C. After Si deposition, the CNT–Si hybrid films were further annealed at T_{an} of 600 °C under 4 vol% H_2/Ar at ambient pressure to improve adhesion between Si and Cu substrate. Before and after Si deposition, each sample was weighed by microbalance with a precision of 1 μg.

4.2.3 Characterization

The analysis of microstructure of ethanol-treated and untreated CNTs-Si core-shell wall films was carried out using field-emission scanning electron microscopy (SEM; S-4800, Hitachi, Tokyo, Japan). To evaluate electrochemical performances of CNT-Si hybrid films, three-electrode beaker cells were

assembled in Ar glove box, which had a CNT-Si hybrid film as the anode, Li metal as the cathode and reference electrode in ~40 mL of electrolyte (1 M $LiClO_4$ in a 1:1 (v/v) mixture of EC and PC with H_2O content of less than 20 ppm, Kishida Chemical, Osaka, Japan). Charge/discharge measurements by constant–current (CC) mode were carried out in the potential range between 0.005–1.200 V vs. Li/Li^+ at the rate of 0.4 A g_{si}^{-1} (corresponding to ~0.1*C*) using galvanostatic cycling with potential limitation system (Bio-Logic VMP3, Claix, France). *C*-rate was determined using the weight of Si and a theoretical value of 4200 mAh g_{si}^{-1}. In this work, I define the Li^+ insertion to CNT–Si films as "charge" and Li^+ extraction from CNT-Si films as "discharge".

4.3 Structure change in CNT arrays by capillary action

Figure 4-1 shows photographs the Cu substrates with CNT arrays grown by Fe catalyst (deposited in a circular area of 8 mm in diameter), without and with ethanol treatment and without and with Si deposition. The untreated CNT arrays had a smooth surface, resulting in a CNT–Si hybrid film with plain surface. While ethanol-treated CNT arrays had clear patterns on the surface, resulting in a CNT–Si hybrid film with patterns after Si deposition at T_{sub} of 400 °C.

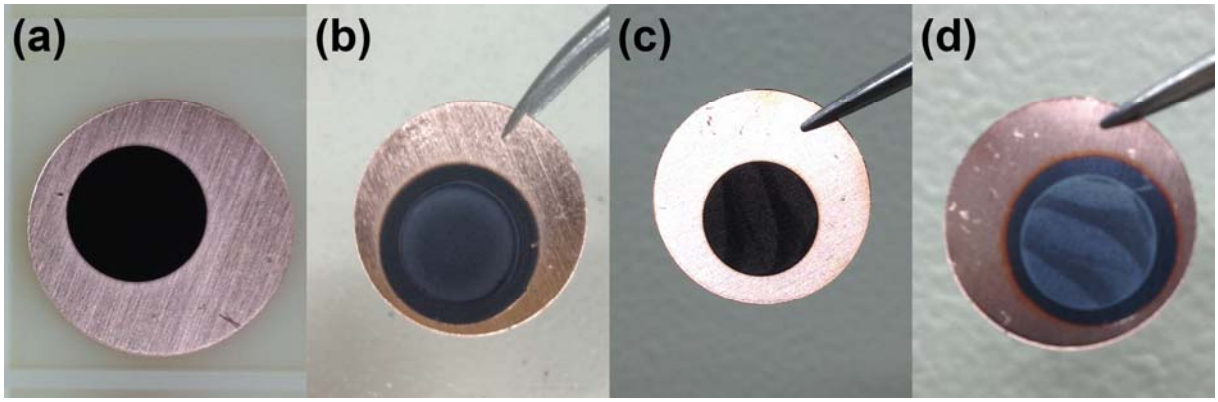

Figure 4-1 Photographs of (a) vertical aligned CNTs grown on Cu substrate, (b) CNTs-Si hybrid film deposited on as-grown CNTs, (c) ethanol-treated CNTs and (d) CNT-Si hybrid film deposited on ethanol-treated CNTs.

The thickness of as grown CNTs was characterized by SEM. For the synthesis of vertical aligned CNTs on Cu substrates, 10-nm-thick Ta was used as diffusion barrier to suppress Cu diffusion [139, 140], and 15-nm-thick TiN was also used as underlayer, which enables Fe or Co to form particles by dewetting [141-143].

Figure 4-2 shows the cross-sectional view SEM images of the vertical aligned CNTs, grown by Fe catalyst for different growth time with a partial pressure of 0.2 Torr C_2H_2 and 2 Torr H_2 at 700 °C. The heighst of CNTs varied from ~10 μm for 4.5 min, ~20 μm for 6 min, ~50 μm for 8 min, to ~110 μm for 30 min. Since the target height of CNTs was 15–20 μm, I used 6 min as the standard CVD time. Figure 4-3 shows the CNTs grown for 6 min, having a thickness of 15–20 μm and a density of

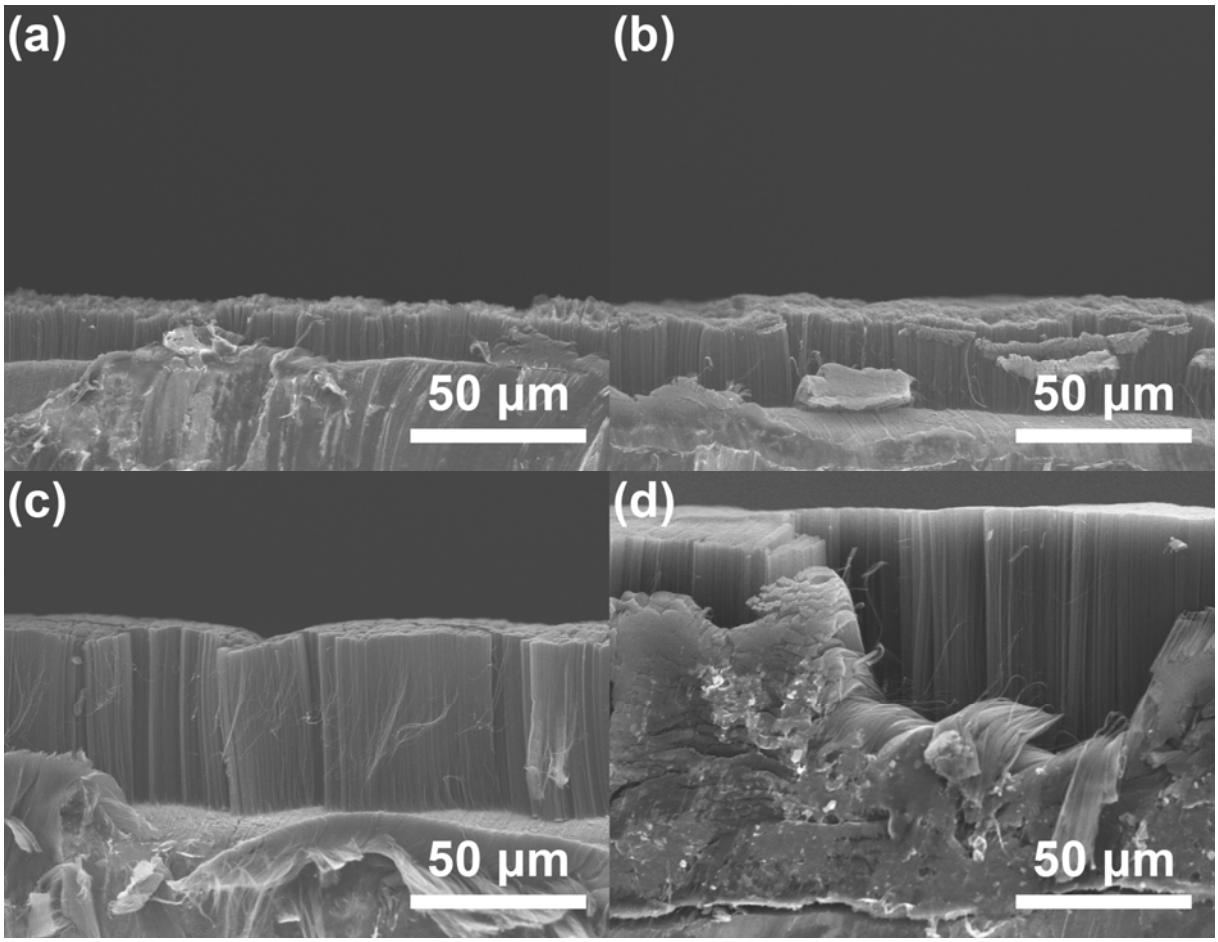

Figure 4-2 Cross-sectional view SEM images of vertical aligned CNTs grown by Fe catalyst for (a) 4.5 min, (b) 6 min, (c) 8 min and (d) 30 min.

~0.07 g cm^{-3}. All of the CNT arrays were aligned vertically to the substrate (Figure 4-3a), while CNTs were entangled with each other at the array top (Figure 4-3b–c).

In contrast, Figure 4-4 shows SEM images of self-organized CNTs as a result of capillary action. When liquid evaporates from CNT arrays, capillary force works on CNTs, which induces the CNT arrays to shrink, and finally results in such wall structure [144-148]. The wall structure also turns to

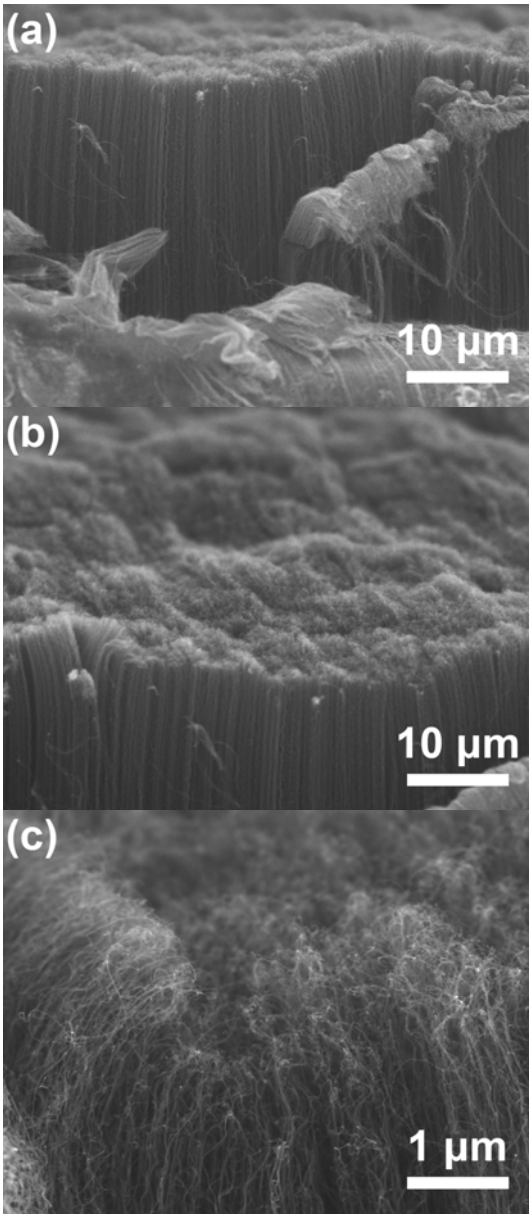

Figure 4-3 (a) Cross-sectional and (b) tilted-view SEM images of vertical aligned CNTs grown using Fe catalyst for 6 min. (c) High magnification of (b)

diverse 3-D structures by either density of CNTs or roughness of substrates. Since as-purchased Cu substrates had line-patterns of ~1 μm in depth on its surface, CNT arrays had lower density near the patterns. Therefore, when the CNT arrays were treated with ethanol, the vertical aligned CNT arrays

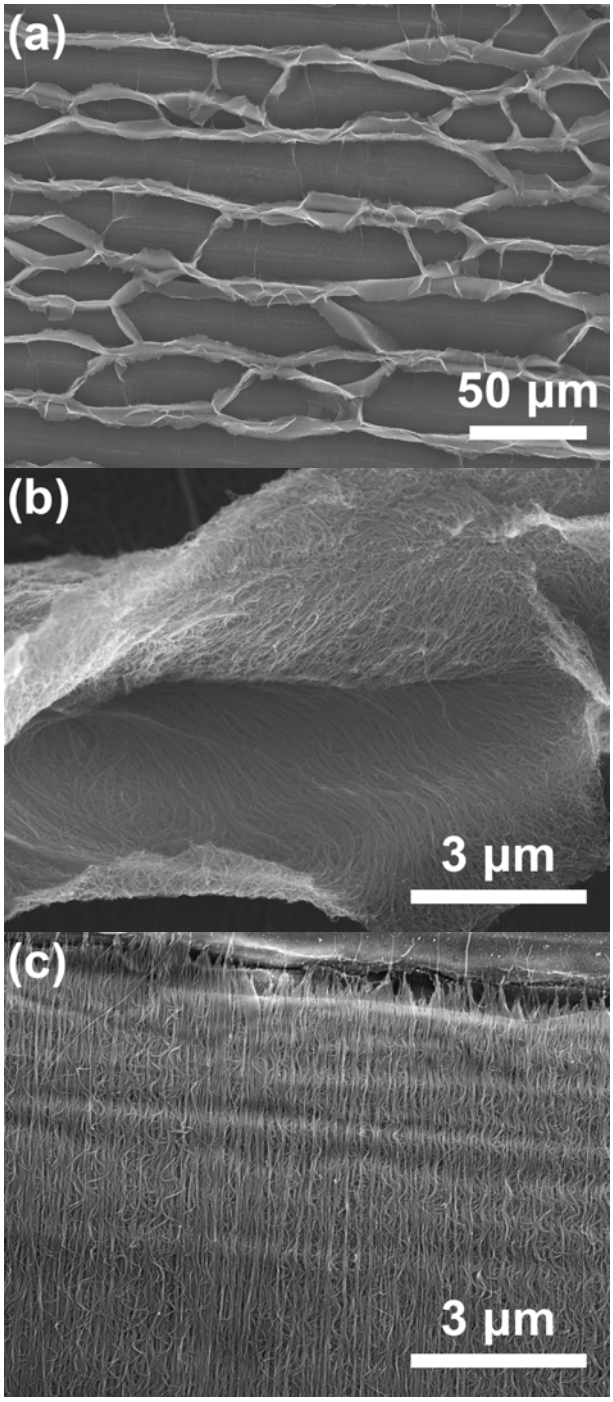

Figure 4-4 (a) A top-view SEM image of self-organized CNT arrays on Cu substrate prepared by ethanol-treatment. (b) High magnification SEM image of aligned CNT walls, and (c) cross-linked CNT walls.

aggregated by themselves to wall structures aligned parallel to the line patterns on the Cu substrate with some crosslinks at random positions.

Figure 4-5 shows the CNT–Si hybrid film deposited on as-grown CNTs by RVD in 2 min at T_{sub} of

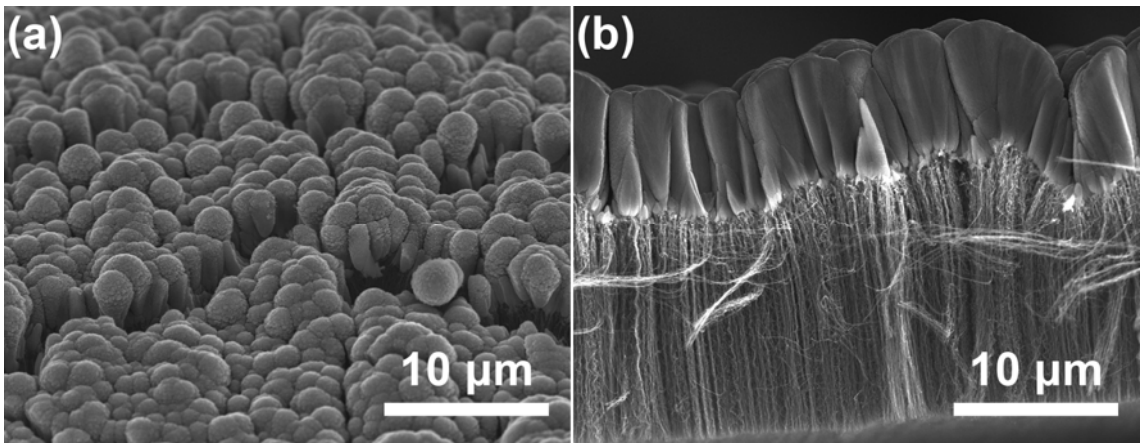

Figure 4-5 (a) Top and (b) cross-sectional view SEM images of the CNT-Si hybrid film deposited on as-grown CNTs at T_{sub} of 400 °C

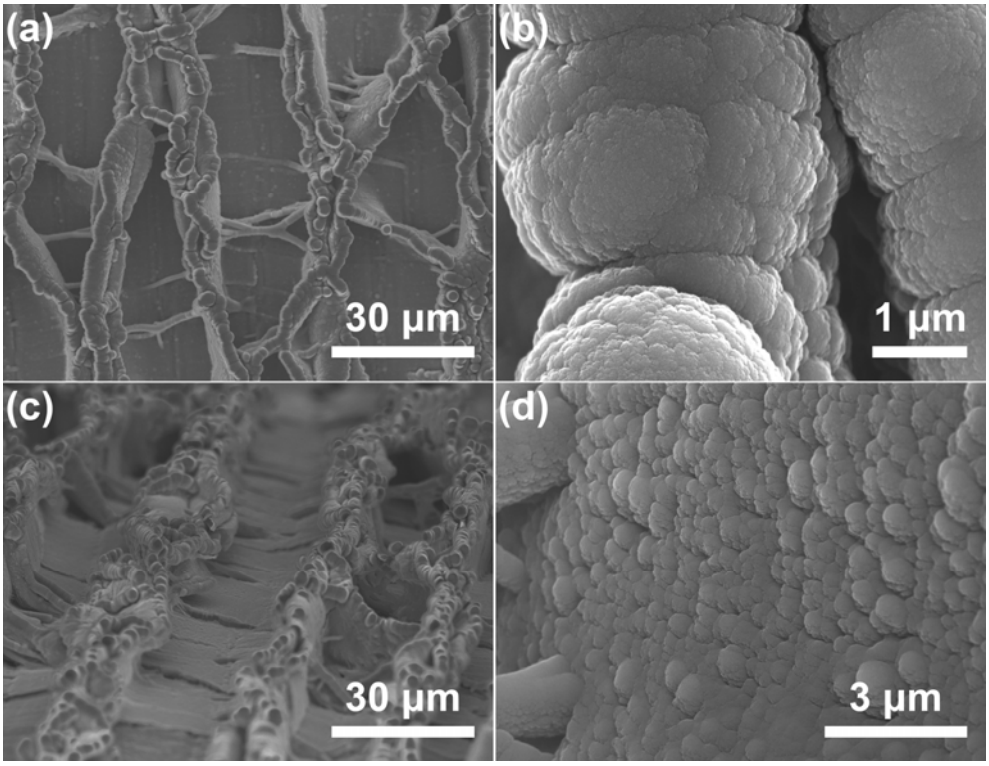

Figure 4-6 (a) A top-view SEM image of the CNT-Si core-shell wall film prepared using ethanol-treated CNT arrays by RVD at T_{sub} of 400 °C. (b) High magnification image of (a). (c) Tilted-view and (d) cross-sectional SEM images of the CNT-Si core-shell wall film.

400 °C. Si did not penetrated deep into the CNT arrays with a narrow interspace (~tens of nm) between CNT bundles, causing most Si to deposit on the array surface without covering CNTs inside the arrays. Resulting CNT–Si hybrid film looked like bean sprouts. In contrast, the Si deposition on ethanol-treated, self-organized CNT walls yielded wall-structured CNT–Si hybrid films with a wall height of ~20 μm and interspace of ~20 μm, as shown in Figure 4-6. Such 2-D microstructure of CNT–Si hybrid film supplies sufficient space for Si to change in volume during charge-discharge cycles although the interspacing should be controlled further. Furthermore, both higher areal density of 0.8–1.7 mg_{si} cm^{-2} and short-fabrication time of 2 min suggest the high potential of this Si-base film for practical use.

4.4 Cycle performance of CNT–Si hybrid film

Figure 4-7 shows the electrochemical behavior of CNT–Si hybrid films deposited at T_{sub} = 400 °C and post-annealed at T_{an} = 600 °C. The initial charge capacities of CNT-Si films with Fe or Co catalysts for CNT growth reached 3822 and 3545 mAh g_{film}^{-1}, respectively, and the initial discharge capacities were 1980 and 1232 mAh g_{film}^{-1}, respectively (Figure 4-7a). The initial charge capacities were closed to that of the pure Si film deposited at T_{sub} = 500 °C (Figure 2-10a), while the initial discharge capacities were much smaller. The large irreversible capacity is attributed to Si consumption during the formation of solid electrolyte interphase (SEI), which was significant because of the large exposed surface area of 2-D wall-shape structure of CNT–Si film formed by CNT arrays. The CNT–Si film using Fe catalyst for CNT growth showed poor cycle performance for 10 cycles (Figure 4-7, and Figure 4-8a). As shown in Figure 4-7a, capacity dropped continuously even after 2nd charge. Finally, the discharge capacity at the 10th cycle decreased to 293 mAh g_{film}^{-1}. The CNT–Si film (Fe catalyst for CNT growth) peeled off the Cu substrate had a similar morphology as initial

film, without being completely pulverized (Figure 4-8b and c). At the region where the CNT–Si film was peeling off, SEM-EDX analysis detected Ti Kα, but did not detect Fe Kα, indicating Fe catalyst layer corroded at interface between CNT and Ti underlayer during electrochemical reaction, causing CNT–Si films peeled off. It is known that Fe can easily corrode when it is exposed to moisture and also even more quickly if the moisture is salt water like electrolyte of electrochemical cell [152].

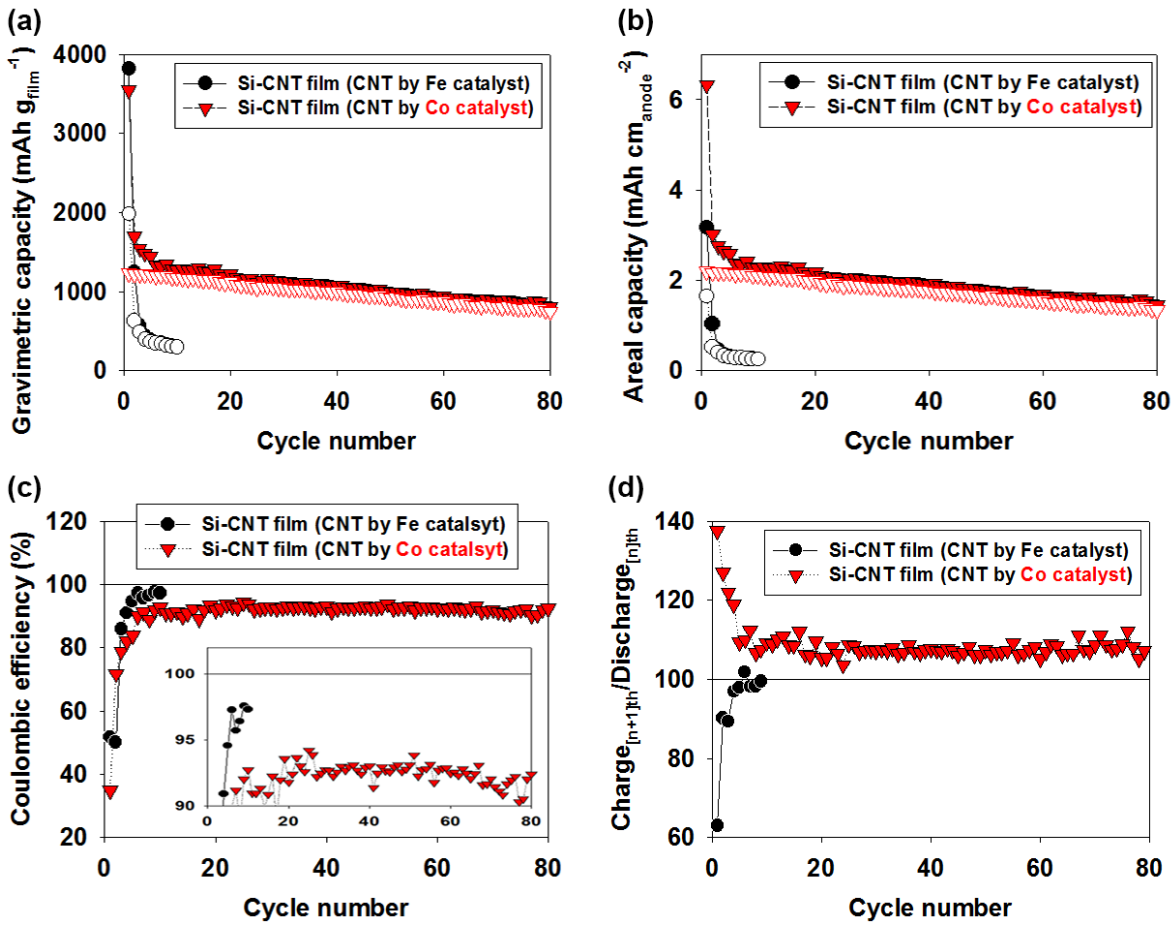

Figure 4-7 Electrochemical performance of CNT–Si films with CNT arrays grown by different catalysts (Fe and Co). Si was deposited by RVD at T_{sub} = 400 °C and post-annealed at T_{an} = 600 °C. (a) Gravimetric capacity, (b) areal capacity, (c) Coulombic efficiency, and (d) capacity ratio of charge$_{[n+1]th}$/discharge$_{[n]th}$.

In contrast, the CNT–Si hybrid film (Co catalyst for CNT growth) showed better cycle performance with a discharge capacity of 749 mAh g_{film}^{-1} and a capacity retention of 60% at the 80th cycle, indicating that the Co catalyst layer resisted against corrosion by the electrolyte of 1 M $LiClO_4$ in a

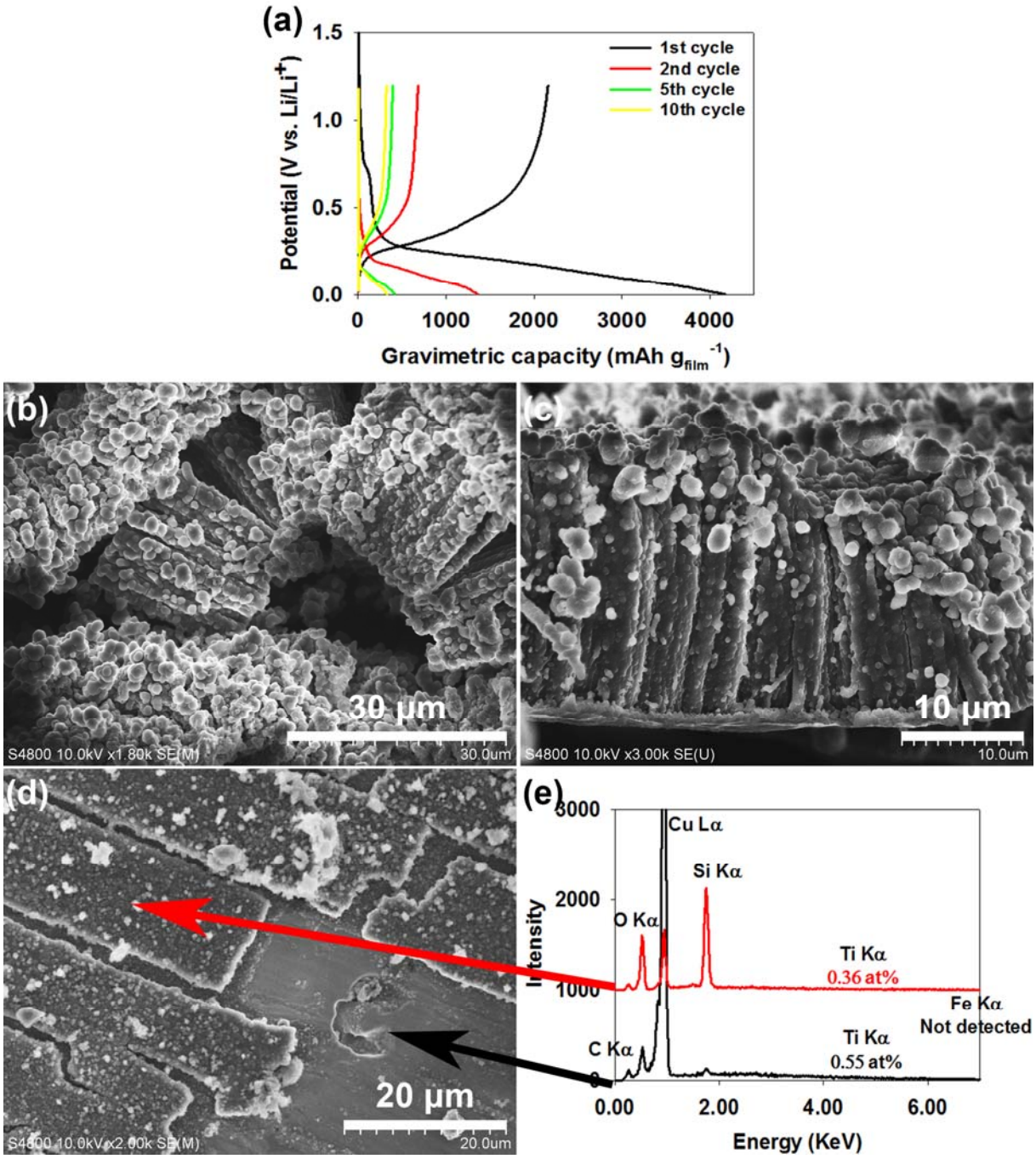

Figure 4-8 (a) Voltage-capacity profiles, (b) tilted-view, (c) cross-sectional view, and (d) top-view of SEM image of CNT–Si film with Fe catalyst for CNT growth after 80th discharge. Cycle test was performed at the rate of 0.4 A g^{-1}. (e) SEM-EDX analysis results for the CNT–Si film after 80th discharge.

1:1 (v/v) the mixture of EC and PC. It is reported that the use of PC causes exfoliation of graphene layers in graphitic carbons via solvent co-intercalation, resulting in its reduction and release of propylene gas [153, 154]. The Coulombic efficiency of CNT–Si film (Co catalyst for CNT growth) was ~92% at the 10th cycle, and remained at ~92% for 80 cycles, which is worse than previous our Si-base films. The capacity ratio of the [n+1]th charge over the [n]th discharge for the films was above 107% at the 80th cycle, suggesting that continuous SEI formation due to incomplete formation of stable SEI layer in the early cycles, possibly because of CNTs. The areal capacity (mAh cm_{anode}^{-2}) of the CNT–Si film is highly important factor for practical battery device. The areal capacity of the CNT–Si film (Co catalyst for CNT growth) was 1.33 mAh cm_{anode}^{-2} at the 80th cycle, which is higher than previously reported values for Si nanomaterials (0.2–0.4 mAh cm_{anode}^{-2} [79, 88]) and porous Si–Cu films by ourselves (0.96 mAh cm_{anode}^{-2} [155]).

4.5 Conclusions

I successfully fabricated wall-shaped CNT–Si core-shell hybrid films by Si deposition on capillary force-assisted CNT arrays. In case of Si deposition on as-grown CNT arrays, the arrays held Si mostly on their top. Whereas ethanol-treated CNT arrays, they were well covered with Si. The areal density of CNT–Si hybrid film was 0.8–1.7 mg cm^{-2}. The CNT–Si hybrid film by Fe catalyst for CNT growth suffered from the corrosion of Fe during electrochemical reaction, resulting in delamination of film at the interface between the CNT–Si film and Ti underlayer. On the other hand, the CNT–Si hybrid film by Co catalyst for CNT growth were more stable with a gravimetric capacity of 749 mAh g_{film}^{-1} and an areal capacity of 1.33 mAh cm_{anode}^{-2} at the 80th cycle. Although further improvement such by controlling the wall distance, and by optimization of electrolyte and electrolyte additives is required, the CNT–Si films by RVD within 2 min are attractive for practical use in lithium secondary batteries when we consider their quick and simple fabrication using inexpensive source materials.

Chapter 5 – Conclusions and perspectives

Targeting at lithium secondary battery anodes, porous Si-base films were fabricated on Cu current collectors through a simple process, called RVD, without using any binder and conductive additives. The RVD process, making 3–14-micrometer-thick Si-base films, features rapid Si deposition in 1 min, which is proper to large-scale, low-cost production for practical battery devices. The porous Si-base films had wall-shaped structure along the line patterns on Cu substrate surface, and the porosity was simply controlled by changing substrate temperature, T_{sub}. The adhesion between Si-base films and Cu substrates was improved by pretreatment of Cu substrate surface through UV-O_3 exposure followed by annealing under H_2 flow and by development of gradient Si-Cu layers with sub-μm thickness by post-annealing and with several-μm thickness (entire film) by co-deposition of Si with Cu. Especially, the co-deposition methods proposed in this study remarkably enhanced the adhesion at the interface between the Si-Cu films and Cu substrates without crystallizing and densifying the Si-base films. The films deposited using a Si source with 5 wt% Cu at T_{sub} of 100 °C exhibited the highest electrochemical performance of fairly high initial charge and discharge capacities of 3425 mAh g_{film}^{-1} and 2073 mAh g_{film}^{-1}, respectively, and capacity retention of 60% with a discharge capacity of 1250 mAh g_{film}^{-1} at the 100th cycle. The amorphous phase with micrometer-thick Si/Cu gradient and high porosity of ~30% built in the Si-Cu film realized such high capacities for fairly thick Si–Cu films. Furthermore, the volumetric capacity of ~1900 mAh cm_{film}^{-3} and areal capacity of

~0.95 mAh cm_{anode}^{-2} at the 100th cycle approaches to the value of practical lithium ion battery anodes. In addition, when the RVD method is applied to the capillary force-assisted self-organized CNT arrays, RVD yielded wall-structured CNT-Si hybrid films with an areal capacity of 1.33 mAh cm_{anode}^{-2} at the 80th cycle, which suggests an alternative method for making practically thick 3-dimensional Si-base films.

Rapid vapour deposition will be compatible with practical production of Si-base anodes in terms of its high deposition rate, simple process, and inexpensive and safe source materials, but further research is needed to improve the anode performance of Si-base films such as optimum cut-off potential during lithation/delithiation and electrolyte additives like vinylene carbonate for more stable SEI layer to meet the requirements for practical devices.

References

[1] A. Sieminski. International energy outlook 2013. *US Energy Information Administration (EIA) Report Number: DOE/EIA-0484* 2013.

[2] I. B. Fridleifsson. Geothermal energy for the benefit of the people. *Renewable and Sustainable Energy Reviews 5(3),* pp. 299-312. 2001.

[3] M. Asif and T. Muneer. Energy supply, its demand and security issues for developed and emerging economies. *Renewable and Sustainable Energy Reviews 11(7),* pp. 1388-1413. 2007.

[4] Q. Zhang, C. S. Dandeneau, X. Zhou and G. Cao. ZnO nanostructures for Dye‐Sensitized solar cells. *Adv Mater 21(41),* pp. 4087-4108. 2009.

[5] M. M. Thackeray, C. Wolverton and E. D. Isaacs. Electrical energy storage for transportation—approaching the limits of, and going beyond, lithium-ion batteries. *Energy & Environmental Science 5(7),* pp. 7854-7863. 2012.

[6] A. J. Markel and A. Simpson. *Plug-in Hybrid Electric Vehicle Energy Storage System Design* 2006.

[7] S. B. Peterson, J. Whitacre and J. Apt. The economics of using plug-in hybrid electric vehicle battery packs for grid storage. *J. Power Sources 195(8),* pp. 2377-2384. 2010.

[8] K. Parks, P. Denholm and A. J. Markel. *Costs and Emissions Associated with Plug-in Hybrid Electric Vehicle Charging in the Xcel Energy Colorado Service Territory* 2007.

[9] P. F. Ribeiro, B. K. Johnson, M. L. Crow, A. Arsoy and Y. Liu. Energy storage systems for advanced power applications. *Proc IEEE 89(12),* pp. 1744-1756. 2001.

[10] G. Petrone, G. Spagnuolo, R. Teodorescu, M. Veerachary and M. Vitelli. Reliability issues in photovoltaic power processing systems. *Industrial Electronics, IEEE Transactions on 55(7),* pp. 2569-2580. 2008.

[11] Y. Qin, X. Wang and Z. L. Wang. Microfibre–nanowire hybrid structure for energy scavenging. *Nature 451(7180),* pp. 809-813. 2008.

[12] J. Linnemann and R. Steinberger-Wilckens. Realistic costs of wind-hydrogen vehicle fuel production. *Int J Hydrogen Energy 32(10),* pp. 1492-1499. 2007.

[13] Y. Zhang, H. Feng, X. Wu, L. Wang, A. Zhang, T. Xia, H. Dong, X. Li and L. Zhang. Progress of electrochemical capacitor electrode materials: A review. *Int J Hydrogen Energy 34(11),* pp. 4889-4899. 2009.

[14] B. B. Garcia, A. M. Feaver, Q. Zhang, R. D. Champion, G. Cao, T. T. Fister, K. P. Nagle and G. T. Seidler. Effect of pore morphology on the electrochemical properties of electric double layer carbon cryogel supercapacitors. *J. Appl. Phys. 104(1),* pp. 014305. 2008.

[15] P. Simon and Y. Gogotsi. Materials for electrochemical capacitors. *Nature Materials 7(11),* pp. 845-854. 2008.

[16] M. S. Whittingham. Lithium batteries and cathode materials. *Chem. Rev. 104(10),* pp. 4271-4302. 2004.

[17] R. J. Brodd, K. R. Bullock, R. A. Leising, R. L. Middaugh, J. R. Miller and E. Takeuchi. Batteries, 1977 to 2002. *J. Electrochem. Soc. 151(3),* pp. K1-K11. 2004.

[18] J. F. Keithley. *The Story of Electrical and Magnetic Measurements: From 500 BC to the 1940s* 1999.

[19] F. R. Bryan. *Henry's Lieutenants* 2003.

[20] B. Kramer, S. Chakraborty and B. Kroposki. A review of plug-in vehicles and vehicle-to-grid capability. Presented at Industrial Electronics, 2008. IECON 2008. 34th Annual Conference of IEEE. 2008, .

[21] J. Sudworth and A. Tiley. *Sodium Sulphur Battery* 1985.

[22] J. Sudworth. The sodium/nickel chloride (ZEBRA) battery. *J. Power Sources 100(1),* pp. 149-163. 2001.

[23] T. Nagaura and K. Tozawa. Lithium ion rechargeable battery. *Prog.Batteries Solar Cells 9*pp. 209. 1990.

[24] J. Tarascon and M. Armand. Issues and challenges facing rechargeable lithium batteries. *Nature 414(6861),* pp. 359-367. 2001.

[25] B. J. Landi, M. J. Ganter, C. D. Cress, R. A. DiLeo and R. P. Raffaelle. Carbon nanotubes for lithium ion batteries. *Energy & Environmental Science 2(6),* pp. 638-654. 2009.

[26] D. Linden and T. Reddy. Handbook of batteries, 2002.

[27] S. Ahn, Y. Kim, K. J. Kim, T. H. Kim, H. Lee and M. H. Kim. Development of high capacity, high rate lithium ion batteries utilizing metal fiber conductive additives. *J. Power Sources 81*pp. 896-901. 1999.

[28] L. Fu, T. Zhang, Q. Cao, H. Zhang and Y. Wu. Preparation and characterization of three-dimensionally ordered mesoporous titania microparticles as anode material for lithium ion battery. *Electrochemistry Communications 9(8),* pp. 2140-2144. 2007.

[29] K. Mizushima, P. Jones, P. Wiseman and J. Goodenough. Li< sub> x</sub> CoO< sub> 2</sub>(0< x<-1): A new cathode material for batteries of high energy density. *Mater. Res. Bull. 15(6),* pp. 783-789. 1980.

[30] M. Zou, M. Yoshio, S. Gopukumar and J. Yamaki. Synthesis of high-voltage (4.5 V) cycling doped LiCoO2 for use in lithium rechargeable cells. *Chemistry of Materials 15(25),* pp. 4699-4702. 2003.

[31] N. Yabuuchi and T. Ohzuku. Novel lithium insertion material of LiCo< sub> 1/3</sub> ni< sub> 1/3</sub> mn< sub> 1/3</sub> O< sub> 2</sub> for advanced lithium-ion batteries. *J. Power Sources 119*pp. 171-174. 2003.

[32] R. Gummow, A. De Kock and M. Thackeray. Improved capacity retention in rechargeable 4 V lithium/lithium-manganese oxide (spinel) cells. *Solid State Ionics 69(1),* pp. 59-67. 1994.

[33] A. _. K. Padhi, K. Nanjundaswamy and J. B. d. Goodenough. Phospho‐olivines as positive‐electrode materials for rechargeable lithium batteries. *J. Electrochem. Soc. 144(4),* pp. 1188-1194. 1997.

[34] M. Nishizawa and I. Uchida. Microelectrode-based characterization systems for advanced materials in battery and sensor applications. *Electrochim. Acta 44(21),* pp. 3629-3637. 1999.

[35] W. W. Lee and J. Lee. Novel synthesis of high performance anode materials for lithium-ion batteries (LIBs). *Journal of Materials Chemistry A 2(6),* pp. 1589-1626. 2014.

[36] R. Kanno, Y. Takeda, T. Ichikawa, K. Nakanishi and O. Yamamoto. Carbon as negative electrodes in lithium secondary cells. *J. Power Sources 26(3),* pp. 535-543. 1989.

[37] M. Mohri, N. Yanagisawa, Y. Tajima, H. Tanaka, T. Mitate, S. Nakajima, M. Yoshida, Y. Yoshimoto, T. Suzuki and H. Wada. Rechargeable lithium battery based on pyrolytic carbon as a negative electrode. *J. Power Sources 26(3),* pp. 545-551. 1989.

[38] L. Ji, Z. Lin, M. Alcoutlabi and X. Zhang. Recent developments in nanostructured anode materials for rechargeable lithium-ion batteries. *Energy & Environmental Science 4(8),* pp. 2682-2699. 2011.

[39] H. Shimoda, B. Gao, X. Tang, A. Kleinhammes, L. Fleming, Y. Wu and O. Zhou. Lithium intercalation into opened single-wall carbon nanotubes: Storage capacity and electronic properties. *Phys. Rev. Lett. 88(1),* pp. 015502. 2001.

[40] X. X. Wang, J. N. Wang, H. Chang and Y. F. Zhang. Preparation of short carbon nanotubes and application as an electrode material in Li‐Ion batteries. *Advanced Functional Materials 17(17),* pp. 3613-3618. 2007.

[41] L. Ji, Z. Lin, A. J. Medford and X. Zhang. Porous carbon nanofibers from electrospun polyacrylonitrile/SiO< sub> 2</sub> composites as an energy storage material. *Carbon 47(14),* pp. 3346-3354. 2009.

[42] L. Ji and X. Zhang. Fabrication of porous carbon nanofibers and their application as anode materials for rechargeable lithium-ion batteries. *Nanotechnology 20(15),* pp. 155705. 2009.

[43] L. Ji, Y. Yao, O. Toprakci, Z. Lin, Y. Liang, Q. Shi, A. J. Medford, C. R. Millns and X. Zhang. Fabrication of carbon nanofiber-driven electrodes from electrospun polyacrylonitrile/polypyrrole

bicomponents for high-performance rechargeable lithium-ion batteries. *J. Power Sources 195(7),* pp. 2050-2056. 2010.

[44] G. Wang, B. Wang, X. Wang, J. Park, S. Dou, H. Ahn and K. Kim. Sn/graphene nanocomposite with 3D architecture for enhanced reversible lithium storage in lithium ion batteries. *Journal of Materials Chemistry 19(44),* pp. 8378-8384. 2009.

[45] S. Chen, P. Chen, M. Wu, D. Pan and Y. Wang. Graphene supported Sn–Sb@ carbon core-shell particles as a superior anode for lithium ion batteries. *Electrochemistry Communications 12(10),* pp. 1302-1306. 2010.

[46] S. Chou, J. Wang, M. Choucair, H. Liu, J. A. Stride and S. Dou. Enhanced reversible lithium storage in a nanosize silicon/graphene composite. *Electrochemistry Communications 12(2),* pp. 303-306. 2010.

[47] S. Yang, G. Cui, S. Pang, Q. Cao, U. Kolb, X. Feng, J. Maier and K. Müllen. Fabrication of cobalt and cobalt Oxide/Graphene composites: Towards High‐Performance anode materials for lithium ion batteries. *ChemSusChem 3(2),* pp. 236-239. 2010.

[48] Z. Wu, W. Ren, L. Wen, L. Gao, J. Zhao, Z. Chen, G. Zhou, F. Li and H. Cheng. Graphene anchored with Co3O4 nanoparticles as anode of lithium ion batteries with enhanced reversible capacity and cyclic performance. *ACS Nano 4(6),* pp. 3187-3194. 2010.

[49] D. Wang, D. Choi, J. Li, Z. Yang, Z. Nie, R. Kou, D. Hu, C. Wang, L. V. Saraf and J. Zhang. Self-assembled TiO2–graphene hybrid nanostructures for enhanced li-ion insertion. *ACS Nano 3(4),* pp. 907-914. 2009.

[50] M. Zhang, D. Lei, X. Yin, L. Chen, Q. Li, Y. Wang and T. Wang. Magnetite/graphene composites: Microwave irradiation synthesis and enhanced cycling and rate performances for lithium ion batteries. *J.Mater.Chem. 20(26),* pp. 5538-5543. 2010.

[51] G. Zhou, D. Wang, F. Li, L. Zhang, N. Li, Z. Wu, L. Wen, G. Q. Lu and H. Cheng. Graphene-wrapped Fe3O4 anode material with improved reversible capacity and cyclic stability for lithium ion batteries. *Chemistry of Materials 22(18),* pp. 5306-5313. 2010.

[52] H. Wang, L. Cui, Y. Yang, H. Sanchez Casalongue, J. T. Robinson, Y. Liang, Y. Cui and H. Dai. Mn3O4− graphene hybrid as a high-capacity anode material for lithium ion batteries. *J. Am. Chem. Soc. 132(40),* pp. 13978-13980. 2010.

[53] B. Wang, X. Wu, C. Shu, Y. Guo and C. Wang. Synthesis of CuO/graphene nanocomposite as a high-performance anode material for lithium-ion batteries. *Journal of Materials Chemistry 20(47),* pp. 10661-10664. 2010.

[54] X. Wang, X. Zhou, K. Yao, J. Zhang and Z. Liu. A SnO< sub> 2</sub>/graphene composite as a high stability electrode for lithium ion batteries. *Carbon 49(1),* pp. 133-139. 2011.

[55] S. Ding, D. Luan, F. Y. C. Boey, J. S. Chen and X. W. D. Lou. SnO 2 nanosheets grown on graphene sheets with enhanced lithium storage properties. *Chemical Communications 47(25),* pp. 7155-7157. 2011.

[56] P. Guo, H. Song and X. Chen. Electrochemical performance of graphene nanosheets as anode material for lithium-ion batteries. *Electrochemistry Communications 11(6),* pp. 1320-1324. 2009.

[57] S. Paek, E. Yoo and I. Honma. Enhanced cyclic performance and lithium storage capacity of SnO2/graphene nanoporous electrodes with three-dimensionally delaminated flexible structure. *Nano Letters 9(1),* pp. 72-75. 2008.

[58] F. Cheng, Z. Tao, J. Liang and J. Chen. Template-directed materials for rechargeable lithium-ion batteries†. *Chemistry of Materials 20(3),* pp. 667-681. 2007.

[59] H. Zhou, S. Zhu, M. Hibino, I. Honma and M. Ichihara. Lithium storage in ordered mesoporous carbon (CMK‐3) with high reversible specific energy capacity and good cycling performance. *Adv Mater 15(24),* pp. 2107-2111. 2003.

[60] H. Wolf, Z. Pajkic, T. Gerdes and M. Willert-Porada. Carbon–fiber–silicon-nanocomposites for lithium-ion battery anodes by microwave plasma chemical vapor deposition. *J. Power Sources 190(1),* pp. 157-161. 2009.

[61] B. Boukamp, G. Lesh and R. Huggins. All‐solid lithium electrodes with mixed‐conductor matrix. *J. Electrochem. Soc. 128(4),* pp. 725-729. 1981.

[62] J. Wang, I. Raistrick and R. Huggins. Behavior of some binary lithium alloys as negative electrodes in organic Solvent‐Based electrolytes. *J. Electrochem. Soc. 133(3),* pp. 457-460. 1986.

[63] W. Wang, M. K. Datta and P. N. Kumta. Silicon-based composite anodes for li-ion rechargeable batteries. *Journal of Materials Chemistry 17(30),* pp. 3229-3237. 2007.

[64] H. Wu and Y. Cui. Designing nanostructured si anodes for high energy lithium ion batteries. *Nano Today 7(5),* pp. 414-429. 2012.

[65] R. A. Huggins. Lithium alloy negative electrodes. *J. Power Sources 81*pp. 13-19. 1999.

[66] T. Hatchard and J. Dahn. In situ XRD and electrochemical study of the reaction of lithium with amorphous silicon. *J. Electrochem. Soc. 151(6),* pp. A838-A842. 2004.

[67] M. Obrovac and L. Christensen. Structural changes in silicon anodes during lithium insertion/extraction. *Electrochemical and Solid-State Letters 7(5),* pp. A93-A96. 2004.

[68] K. Ogata, E. Salager, C. Kerr, A. Fraser, C. Ducati, A. Morris, S. Hofmann and C. Grey. Revealing lithium–silicide phase transformations in nano-structured silicon-based lithium ion batteries via in situ NMR spectroscopy. *Nature Communications 5*2014.

[69] I. Kim, P. Kumta and G. Blomgren. Si/TiN nanocomposites novel anode materials for Li‐Ion batteries. *Electrochemical and Solid-State Letters 3(11),* pp. 493-496. 2000.

[70] S. Bourderau, T. Brousse and D. Schleich. Amorphous silicon as a possible anode material for li-ion batteries. *J. Power Sources 81*pp. 233-236. 1999.

[71] J. Maranchi, A. Hepp, A. Evans, N. Nuhfer and P. Kumta. Interfacial properties of the a-si/cu: Active–Inactive thin-film anode system for lithium-ion batteries. *J. Electrochem. Soc. 153(6),* pp. A1246-A1253. 2006.

[72] X. Zhang, R. Kostecki, T. J. Richardson, J. K. Pugh and P. N. Ross. Electrochemical and infrared studies of the reduction of organic carbonates. *J. Electrochem. Soc. 148(12),* pp. A1341-A1345. 2001.

[73] D. Aurbach, M. Daroux, P. Faguy and E. Yeager. Identification of surface films formed on lithium in propylene carbonate solutions. *J. Electrochem. Soc. 134(7),* pp. 1611-1620. 1987.

[74] E. Peled, D. Golodnitsky and G. Ardel. Advanced model for solid electrolyte interphase electrodes in liquid and polymer electrolytes. *J. Electrochem. Soc. 144(8),* pp. L208-L210. 1997.

[75] D. Aurbach, B. Markovsky, I. Weissman, E. Levi and Y. Ein-Eli. On the correlation between surface chemistry and performance of graphite negative electrodes for li ion batteries. *Electrochim. Acta 45(1),* pp. 67-86. 1999.

[76] D. Aurbach. Review of selected electrode–solution interactions which determine the performance of li and li ion batteries. *J. Power Sources 89(2),* pp. 206-218. 2000.

[77] P. Verma, P. Maire and P. Novák. A review of the features and analyses of the solid electrolyte interphase in li-ion batteries. *Electrochim. Acta 55(22),* pp. 6332-6341. 2010.

[78] R. Ruffo, S. S. Hong, C. K. Chan, R. A. Huggins and Y. Cui. Impedance analysis of silicon nanowire lithium ion battery anodes. *The Journal of Physical Chemistry C 113(26),* pp. 11390-11398. 2009.

[79] C. K. Chan, H. Peng, G. Liu, K. McIlwrath, X. F. Zhang, R. A. Huggins and Y. Cui. High-performance lithium battery anodes using silicon nanowires. *Nature Nanotechnology 3(1),* pp. 31-35. 2007.

[80] H. Wu, G. Chan, J. W. Choi, Y. Yao, M. T. McDowell, S. W. Lee, A. Jackson, Y. Yang, L. Hu and Y. Cui. Stable cycling of double-walled silicon nanotube battery anodes through solid-electrolyte interphase control. *Nature Nanotechnology 7(5),* pp. 310-315. 2012.

[81] T. Osaka, H. Nara, T. Momma and T. Yokoshima. New Si–O–C composite film anode materials for LIB by electrodeposition. *Journal of Materials Chemistry A 2(4),* pp. 883-896. 2014.

[82] H. Nara, T. Yokoshima, T. Momma and T. Osaka. Highly durable SiOC composite anode prepared by electrodeposition for lithium secondary batteries. *Energy & Environmental Science 5(4),* pp. 6500-6505. 2012.

[83] H. T. Nguyen, M. R. Zamfir, L. D. Duong, Y. H. Lee, P. Bondavalli and D. Pribat. Alumina-coated silicon-based nanowire arrays for high quality li-ion battery anodes. *Journal of Materials Chemistry 22(47),* pp. 24618-24626. 2012.

[84] W. Zhang. A review of the electrochemical performance of alloy anodes for lithium-ion batteries. *J. Power Sources 196(1),* pp. 13-24. 2011.

[85] T. Takamura, S. Ohara, M. Uehara, J. Suzuki and K. Sekine. A vacuum deposited si film having a li extraction capacity over 2000 mAh/g with a long cycle life. *J. Power Sources 129(1),* pp. 96-100. 2004.

[86] J. Yin, M. Wada, K. Yamamoto, Y. Kitano, S. Tanase and T. Sakai. Micrometer-scale amorphous si thin-film electrodes fabricated by electron-beam deposition for li-ion batteries. *J. Electrochem. Soc. 153(3),* pp. A472-A477. 2006.

[87] M. Obrovac and L. Krause. Reversible cycling of crystalline silicon powder. *J. Electrochem. Soc. 154(2),* pp. A103-A108. 2007.

[88] C. K. Chan, R. N. Patel, M. J. O'Connell, B. A. Korgel and Y. Cui. Solution-grown silicon nanowires for lithium-ion battery anodes. *ACS Nano 4(3),* pp. 1443-1450. 2010.

[89] X. H. Liu, H. Zheng, L. Zhong, S. Huang, K. Karki, L. Q. Zhang, Y. Liu, A. Kushima, W. T. Liang and J. W. Wang. Anisotropic swelling and fracture of silicon nanowires during lithiation. *Nano Letters 11(8),* pp. 3312-3318. 2011.

[90] M. Ge, J. Rong, X. Fang and C. Zhou. Porous doped silicon nanowires for lithium ion battery anode with long cycle life. *Nano Letters 12(5),* pp. 2318-2323. 2012.

[91] H. Chen, J. Xu, P. Chen, X. Fang, J. Qiu, Y. Fu and C. Zhou. Bulk synthesis of crystalline and crystalline core/amorphous shell silicon nanowires and their application for energy storage. *ACS Nano 5(10),* pp. 8383-8390. 2011.

[92] H. Kim, M. Seo, M. Park and J. Cho. A critical size of silicon Nano‐Anodes for lithium rechargeable batteries. *Angewandte Chemie International Edition 49(12),* pp. 2146-2149. 2010.

[93] N. Dimov, S. Kugino and M. Yoshio. Carbon-coated silicon as anode material for lithium ion batteries: Advantages and limitations. *Electrochim. Acta 48(11),* pp. 1579-1587. 2003.

[94] R. Krishnan, T. Lu and N. Koratkar. Functionally strain-graded nanoscoops for high power li-ion battery anodes. *Nano Letters 11(2),* pp. 377-384. 2010.

[95] M. Park, M. G. Kim, J. Joo, K. Kim, J. Kim, S. Ahn, Y. Cui and J. Cho. Silicon nanotube battery anodes. *Nano Letters 9(11),* pp. 3844-3847. 2009.

[96] T. Song, J. Xia, J. Lee, D. H. Lee, M. Kwon, J. Choi, J. Wu, S. K. Doo, H. Chang and W. I. Park. Arrays of sealed silicon nanotubes as anodes for lithium ion batteries. *Nano Letters 10(5),* pp. 1710-1716. 2010.

[97] L. Cui, Y. Yang, C. Hsu and Y. Cui. Carbon− silicon core− shell nanowires as high capacity electrode for lithium ion batteries. *Nano Letters 9(9),* pp. 3370-3374. 2009.

[98] W. W. Mullins. Theory of thermal grooving. *J. Appl. Phys. 28(3),* pp. 333-339. 1957.

[99] G. S. Bales, R. Bruinsma, E. A. Eklund, R. P. Karunasiri, J. Rudnick and A. Zangwill. Growth and erosion of thin solid films. *Science 249(4966),* pp. 264-268. 1990. . DOI: 249/4966/264 [pii].

[100] C. Spinella, S. Lombardo and F. Priolo. Crystal grain nucleation in amorphous silicon. *J. Appl. Phys. 84(10),* pp. 5383-5414. 1998.

[101] L. Fiermans, R. Hoogewijs and J. Vennik. Electron spectroscopy of transition metal oxide surfaces. *Surf. Sci. 47(1),* pp. 1-40. 1975.

[102] G. Schön. Auger and direct electron spectra in X-ray photoelectron studies of zinc, zinc oxide, gallium and gallium oxide. *Journal of Electron Spectroscopy and Related Phenomena 2(1),* pp. 75-86. 1973.

[103] B. R. Strohmeier, D. E. Levden, R. S. Field and D. M. Hercules. Surface spectroscopic characterization of CuAl2O3 catalysts. *Journal of Catalysis 94(2),* pp. 514-530. 1985.

[104] K. H. Schulz and D. F. Cox. Surface reactions of acrolein and propionaldehyde on cuprous oxide (100): Nonselective oxidation and enolate-mediated side reactions to C3 products. *J. Phys. Chem. 97(14),* pp. 3555-3564. 1993.

[105] H. Ago, T. Kugler, F. Cacialli, W. R. Salaneck, M. S. Shaffer, A. H. Windle and R. H. Friend. Work functions and surface functional groups of multiwall carbon nanotubes. *The Journal of Physical Chemistry B 103(38),* pp. 8116-8121. 1999.

[106] J. L. Goldman, B. R. Long, A. A. Gewirth and R. G. Nuzzo. Strain anisotropies and Self‐Limiting capacities in Single‐Crystalline 3D silicon microstructures: Models for high energy density Lithium‐Ion battery anodes. *Advanced Functional Materials 21(13),* pp. 2412-2422. 2011.

[107] A. S. Fedorov, Z. I. Popov, A. A. Kuzubov and S. G. Ovchinnikov. Theoretical study of the diffusion of lithium in crystalline and amorphous silicon. *JETP Letters 95(3),* pp. 143-147. 2012.

[108] E. Peled. The electrochemical behavior of alkali and alkaline earth metals in nonaqueous battery systems—the solid electrolyte interphase model. *J. Electrochem. Soc. 126(12),* pp. 2047-2051. 1979.

[109] J. Kim, H. Kim and H. Sohn. Addition of cu for carbon coated si-based composites as anode materials for lithium-ion batteries. *Electrochemistry Communications 7(5),* pp. 557-561. 2005.

[110] Y. S. Jung, K. T. Lee, J. H. Kim, J. Y. Kwon and S. M. Oh. Thermo‐electrochemical activation of an In–Cu intermetallic electrode for the anode in lithium secondary batteries. *Advanced Functional Materials 18(19),* pp. 3010-3017. 2008.

[111] S. Jeong, J. Lee, M. Ko, G. Kim, S. Park and J. Cho. Etched graphite with internally grown si nanowires from pores as an anode for high density li-ion batteries. *Nano Letters 13(7),* pp. 3403-3407. 2013.

[112] P. Ramadass, B. Haran, R. White and B. N. Popov. Capacity fade of sony 18650 cells cycled at elevated temperatures: Part I. cycling performance. *J. Power Sources 112(2),* pp. 606-613. 2002.

[113] L. Cui, L. Hu, J. W. Choi and Y. Cui. Light-weight free-standing carbon nanotube-silicon films for anodes of lithium ion batteries. *Acs Nano 4(7),* pp. 3671-3678. 2010.

[114] X. Chen, K. Gerasopoulos, J. Guo, A. Brown, C. Wang, R. Ghodssi and J. N. Culver. Virus-enabled silicon anode for lithium-ion batteries. *ACS Nano 4(9),* pp. 5366-5372. 2010.

[115] G. Wang, J. Ahn, J. Yao, S. Bewlay and H. Liu. Nanostructured Si–C composite anodes for lithium-ion batteries. *Electrochemistry Communications 6(7),* pp. 689-692. 2004.

[116] J. Lee and S. Noda. One-minute deposition of micrometre-thick porous si anodes for lithium ion batteries. *RSC Advances 5(4),* pp. 2938-2946. 2015.

[117] Y. He, B. Yang, K. Yang, C. Brown, R. Ramasamy, H. Wang, C. Lundgren and Y. Zhao. Designing si-based nanowall arrays by dynamic shadowing growth to tailor the performance of li-ion battery anodes. *Journal of Materials Chemistry 22(17),* pp. 8294-8303. 2012.

[118] Y. He, J. Fan and Y. Zhao. Engineering a well-aligned composition-graded CuSi nanorod array by an oblique angle codeposition technique. *Crystal Growth & Design 10(11),* pp. 4954-4958. 2010.

[119] D. Tassis, C. Mitsas, T. Zorba, C. Dimitriadis, O. Valassiades, D. Siapkas, M. Angelakeris, P. Poulopoulos, N. Flevaris and G. Kiriakidis. Infrared spectroscopic and electronic transport properties of polycrystalline semiconducting FeSi2 thin films. *J. Appl. Phys. 80(2),* pp. 962-968. 1996.

[120] D. Tassis, C. Dimitriadis, S. Boultadakis, J. Arvanitidis, S. Ves, S. Kokkou, S. Logothetidis, O. Valassiades, P. Poulopoulos and N. Flevaris. Influence of conventional furnace and rapid thermal annealing on the quality of polycrystalline< i> β</i>-FeSi< sub> 2</sub> thin films grown from vapor-deposited Fe/Si multilayers. *Thin Solid Films 310(1),* pp. 115-122. 1997.

[121] E. Pihan, A. Slaoui, P. Roca i Cabarrocas and A. Focsa. Polycrystalline silicon films by aluminium-induced crystallisation: Growth process vs. silicon deposition method. *Thin Solid Films 451*pp. 328-333. 2004.

[122] L. Pereira, R. Martins, N. Schell, E. Fortunato and R. Martins. Nickel-assisted metal-induced crystallization of silicon: Effect of native silicon oxide layer. *Thin Solid Films 511*pp. 275-279. 2006.

[123] S. Grammatikopoulos, S. Pappas, D. Trachylis, V. Kapaklis, P. Poulopoulos, N. Yahya, C. Politis and M. Velgakis. Cu-induced crystallization of si in CuSi alloyed films and the formation of natural multilayers by oxidation. *Journal of Surfaces and Interfaces of Materials 1(2),* pp. 136-142. 2013.

[124] Y. Zhao, J. Wang, Q. Hu, D. Zhu and D. Li. Copper-induced crystallization of sputtered silicon on ZnO: Al substrate and the textured interface for light trapping. *Appl. Surf. Sci. 257(22),* pp. 9626-9630. 2011.

[125] T. Moustakas, D. Anderson and W. Paul. Preparation of highly photoconductive amorphous silicon by rf sputtering. *Solid State Commun. 23(3),* pp. 155-158. 1977.

[126] J. Li and J. Dahn. An in situ X-ray diffraction study of the reaction of li with crystalline si. *J. Electrochem. Soc. 154(3),* pp. A156-A161. 2007.

[127] X. H. Liu, L. Zhong, S. Huang, S. X. Mao, T. Zhu and J. Y. Huang. Size-dependent fracture of silicon nanoparticles during lithiation. *Acs Nano 6(2),* pp. 1522-1531. 2012.

[128] M. T. McDowell, S. W. Lee, C. Wang, W. D. Nix and Y. Cui. Studying the kinetics of crystalline silicon nanoparticle lithiation with in situ transmission electron microscopy. *Adv Mater 24(45),* pp. 6034-6041. 2012.

[129] H. Ghassemi, M. Au, N. Chen, P. A. Heiden and R. S. Yassar. In situ electrochemical lithiation/delithiation observation of individual amorphous si nanorods. *ACS Nano 5(10),* pp. 7805-7811. 2011.

[130] S. Misra, N. Liu, J. Nelson, S. S. Hong, Y. Cui and M. F. Toney. In situ x-ray diffraction studies of (de) lithiation mechanism in silicon nanowire anodes. *Acs Nano 6(6),* pp. 5465-5473. 2012.

[131] B. Key, M. Morcrette, J. Tarascon and C. P. Grey. Pair distribution function analysis and solid state NMR studies of silicon electrodes for lithium ion batteries: Understanding the (de) lithiation mechanisms. *J. Am. Chem. Soc. 133(3),* pp. 503-512. 2010.

[132] T. Hang, D. Mukoyama, H. Nara, T. Yokoshima, T. Momma, M. Li and T. Osaka. Electrochemical impedance analysis of electrodeposited Si–O–C composite thick film on cu microcones-arrayed current collector for lithium ion battery anode. *J. Power Sources 256*pp. 226-232. 2014.

[133] S. Iijima. Helical microtubules of graphitic carbon. *Nature 354(6348),* pp. 56-58. 1991.

[134] E. Frackowiak, S. Gautier, H. Gaucher, S. Bonnamy and F. Beguin. Electrochemical storage of lithium in multiwalled carbon nanotubes. *Carbon 37(1),* pp. 61-69. 1999.

[135] W. X. Chen, J. Y. Lee and Z. Liu. The nanocomposites of carbon nanotube with sb and SnSb< sub> 0.5</sub> as li-ion battery anodes. *Carbon 41(5),* pp. 959-966. 2003.

[136] Z. Zhang, J. Peng and H. Zhang. Low-temperature resistance of individual single-walled carbon nanotubes: A theoretical estimation. *Appl. Phys. Lett. 79(21),* pp. 3515-3517. 2001.

[137] B. J. Landi, R. P. Raffaelle, M. J. Heben, J. L. Alleman, W. VanDerveer and T. Gennett. Single wall carbon nanotube-nafion composite actuators. *Nano Letters 2(11),* pp. 1329-1332. 2002.

[138] J. Eom, H. Kwon, J. Liu and O. Zhou. Lithium insertion into purified and etched multi-walled carbon nanotubes synthesized on supported catalysts by thermal CVD. *Carbon 42(12),* pp. 2589-2596. 2004.

[139] E. Kolawa, J. Chen, J. Reid, P. Pokela and M. Nicolet. Tantalum‐based diffusion barriers in Si/Cu VLSI metallizations. *J. Appl. Phys. 70(3),* pp. 1369-1373. 1991.

[140] K. Holloway, P. M. Fryer, C. Cabral Jr, J. Harper, P. Bailey and K. Kelleher. Tantalum as a diffusion barrier between copper and silicon: Failure mechanism and effect of nitrogen additions. *J. Appl. Phys. 71(11),* pp. 5433-5444. 1992.

[141] Y. Yamazaki, M. Katagiri, N. Sakuma, M. Suzuki, S. Sato, M. Nihei, M. Wada, N. Matsunaga, T. Sakai and Y. Awano. Synthesis of a closely packed carbon nanotube forest by a multi-step growth method using plasma-based chemical vapor deposition. *Applied Physics Express 3(5),* pp. 055002. 2010.

[142] S. Esconjauregui, M. Fouquet, B. C. Bayer, C. Ducati, R. Smajda, S. Hofmann and J. Robertson. Growth of ultrahigh density vertically aligned carbon nanotube forests for interconnects. *ACS Nano 4(12),* pp. 7431-7436. 2010.

[143] G. Zhong, J. H. Warner, M. Fouquet, A. W. Robertson, B. Chen and J. Robertson. Growth of ultrahigh density single-walled carbon nanotube forests by improved catalyst design. *ACS Nano 6(4),* pp. 2893-2903. 2012.

[144] H. Liu, S. Li, J. Zhai, H. Li, Q. Zheng, L. Jiang and D. Zhu. Self‐Assembly of Large‐Scale micropatterns on aligned carbon nanotube films. *Angewandte Chemie International Edition 43(9),* pp. 1146-1149. 2004.

[145] N. Chakrapani, B. Wei, A. Carrillo, P. M. Ajayan and R. S. Kane. Capillarity-driven assembly of two-dimensional cellular carbon nanotube foams. *Proc. Natl. Acad. Sci. U. S. A. 101(12),* pp. 4009-4012. 2004. . DOI: 10.1073/pnas.0400734101 [doi].

[146] M. De Volder, S. H. Tawfick, S. J. Park, D. Copic, Z. Zhao, W. Lu and A. J. Hart. Diverse 3D microarchitectures made by capillary forming of carbon nanotubes. *Adv Mater 22(39),* pp. 4384-4389. 2010.

[147] X. Lim, H. W. G. Foo, G. H. Chia and C. Sow. Capillarity-assisted assembly of carbon nanotube microstructures with organized initiations. *ACS Nano 4(2),* pp. 1067-1075. 2010.

[148] K. Cui, T. Chiba, S. Omiya, T. Thurakitseree, P. Zhao, S. Fujii, H. Kataura, E. Einarsson, S. Chiashi and S. Maruyama. Self-assembled microhoneycomb network of single-walled carbon nanotubes for solar cells. *The Journal of Physical Chemistry Letters 4(15),* pp. 2571-2576. 2013.

[149] S. Y. Chew, S. H. Ng, J. Wang, P. Novák, F. Krumeich, S. L. Chou, J. Chen and H. K. Liu. Flexible free-standing carbon nanotube films for model lithium-ion batteries. *Carbon 47(13),* pp. 2976-2983. 2009.

[150] G. Wu, C. Wang, X. Zhang, H. Yang, Z. Qi, P. He and W. Li. Structure and lithium insertion properties of carbon nanotubes. *J. Electrochem. Soc. 146(5),* pp. 1696-1701. 1999.

[151] M. E. Spahr, T. Palladino, H. Wilhelm, A. Würsig, D. Goers, H. Buqa, M. Holzapfel and P. Novák. Exfoliation of graphite during electrochemical lithium insertion in ethylene carbonate-containing electrolytes. *J. Electrochem. Soc. 151(9),* pp. A1383-A1395. 2004.

[152] J. W. Hill, D. K. Kolb and S. W. Keller. *Chemistry for Changing Times* 2004.

[153] S. Flandrois and B. Simon. Carbon materials for lithium-ion rechargeable batteries. *Carbon 37(2),* pp. 165-180. 1999.

[154] Y. Wu, E. Rahm and R. Holze. Carbon anode materials for lithium ion batteries. *J. Power Sources 114(2),* pp. 228-236. 2003.

[155] J. Lee, K. Hasegawa, T. Momma, T. Osaka and S. Noda. One-minute deposition of micrometre-thick porous Si–Cu anodes with compositional gradients on cu current collectors for lithium secondary batteries. *J. Power Sources 286*pp. 540-550. 2015.

Acknowledgements

I would like to express my deepest gratitude to my advisor Professor Suguru Noda for providing me with the opportunity of conducting research under his guidance. His expertise, understanding, generous guidance and support made it possible for me to work on a topic that was of great interest to me. Thanks to his hard work, vision and attitudes toward research, it was a great honor for me to learn and grow as a research scientist. I would also like to thank Professor Yukio Yamaguchi for his supporting and valuable advices.

I am also very grateful to all the committee members of my dissertation evaluation, Professors Atsuo Yamada, Kazunari Domen, Yoshiko Tsuji, and Masashi Okubo at the University of Tokyo, and Toshiyuki Momma at the Waseda University for their constructive discussion and valuable opinions.

I would also like to thank Mr. Kenji Nakane and Mr. Singo Matsumoto at Sumitomo Chemical Co. Ltd., for measurement of and valuable discussion about the electrochemical performance of the Si films and contributions in the early stages of Si–Cu films, Professor Yoshiko Tsuji at the University of Tokyo for her support in performing the UV-O_3 treatment, and Professor Kazuyuki Kuroda, Professor Atsushi Shimojima and Mr. Kohei Suzuki at Waseda University for their support with BET measurements. I also thank Mr. Shingo Morokuma at the University of Tokyo and Dr. Taketsugu Yamamoto at Sumitomo Chemical Co. Ltd., for their contributions during the early stage of Si films, and Mr. Nuri Na at the University of Tokyo for his efforts of synthesis of carbon nanotubes on Cu current collector.

I would like to give very special thanks to Toshio Osawa for his technical expertise, which helps me to conduct all experiments smoothly at the laboratory under any circumstances. I am very thankful to Nuri Na for his encouragement and help in several situations. I also want to thank former and present

members of the Yamaguchi-Noda laboratory at the University of Tokyo and Noda laboratory at the Waseda University.

Last, but definitely not least, I want to thank my dearly beloved wife, Ju-Ram Park for her endless love and support, and also thank to my father, mother, brother, and my parents-in-law for all their generous supports and encouragement.

Appendix

NATURE PUBLISHING GROUP LICENSE TERMS AND CONDITIONS

Feb 17, 2015

This is a License Agreement between Jungho Lee ("You") and Nature Publishing Group ("Nature Publishing Group") provided by Copyright Clearance Center ("CCC"). The license consists of your order details, the terms and conditions provided by Nature Publishing Group, and the payment terms and conditions.

All payments must be made in full to CCC. For payment instructions, please see information listed at the bottom of this form.

License Number	3561810190839
License date	Feb 04, 2015
Order Content Publisher	Nature Publishing Group
Order Content Publication	Nature
Order Content Title	Issues and challenges facing rechargeable lithium batteries
Order Content Author	J.-M. Tarascon and M. Armand
Order Content Date	Nov 15, 2001
Volume number	414
Issue number	6861
Type of Use	reuse in a dissertation / thesis
Requestor type	academic/educational
Format	print and electronic
Portion	figures/tables/illustrations
Number of figures/tables/illustrations	1
Figures	Figure 1. Comparison of the different battery technologies in terms of volumetric and gravimetric energy density
Author of this NPG article	no
Your reference number	None
Title of your thesis / dissertation	Rapid vapor deposition of micrometer-thick silicon-base porous anodes for lithium secondary batteries

Expected completion date	Mar 2015
Estimated size (number of pages)	110
Total	**0 JPY**

Terms and Conditions

Terms and Conditions for Permissions

Nature Publishing Group hereby grants you a non-exclusive license to reproduce this material for this purpose, and for no other use,subject to the conditions below:

1. NPG warrants that it has, to the best of its knowledge, the rights to license reuse of this material. However, you should ensure that the material you are requesting is original to Nature Publishing Group and does not carry the copyright of another entity (as credited in the published version). If the credit line on any part of the material you have requested indicates that it was reprinted or adapted by NPG with permission from another source, then you should also seek permission from that source to reuse the material.

2. Permission granted free of charge for material in print is also usually granted for any electronic version of that work, provided that the material is incidental to the work as a whole and that the electronic version is essentially equivalent to, or substitutes for, the print version.Where print permission has been granted for a fee, separate permission must be obtained for any additional, electronic re-use (unless, as in the case of a full paper, this has already been accounted for during your initial request in the calculation of a print run).NB: In all cases, web-based use of full-text articles must be authorized separately through the 'Use on a Web Site' option when requesting permission.

3. Permission granted for a first edition does not apply to second and subsequent editions and for editions in other languages (except for signatories to the STM Permissions Guidelines, or where the first edition permission was granted for free).

4. Nature Publishing Group's permission must be acknowledged next to the figure, table or abstract in print. In electronic form, this acknowledgement must be visible at the same time as the figure/table/abstract, and must be hyperlinked to the journal's homepage.

5. The credit line should read:
   Reprinted by permission from Macmillan Publishers Ltd: [JOURNAL NAME] (reference citation), copyright (year of publication)
   For AOP papers, the credit line should read:
   Reprinted by permission from Macmillan Publishers Ltd: [JOURNAL NAME], advance online publication, day month year (doi: 10.1038/sj.[JOURNAL ACRONYM].XXXXX)

   Note: For republication from the *British Journal of Cancer*, the following credit lines apply.
   Reprinted by permission from Macmillan Publishers Ltd on behalf of Cancer Research UK: [JOURNAL NAME] (reference citation), copyright (year of publication)For AOP papers, the credit line should read:
   Reprinted by permission from Macmillan Publishers Ltd on behalf of Cancer Research UK: [JOURNAL NAME], advance online publication, day month year (doi: 10.1038/sj.[JOURNAL ACRONYM].XXXXX)

6. Adaptations of single figures do not require NPG approval. However, the adaptation should be credited as follows:

   Adapted by permission from Macmillan Publishers Ltd: [JOURNAL NAME] (reference citation), copyright (year of publication)

   Note: For adaptation from the *British Journal of Cancer*, the following credit line applies.
   Adapted by permission from Macmillan Publishers Ltd on behalf of Cancer Research UK: [JOURNAL NAME] (reference citation), copyright (year of publication)

7. Translations of 401 words up to a whole article require NPG approval. Please visithttp://www.macmillanmedicalcommunications.com for more information.Translations of up to a 400 words do not require NPG approval. The translation should be credited as follows:

   Translated by permission from Macmillan Publishers Ltd: [JOURNAL NAME] (reference citation), copyright (year of publication).

   Note: For translation from the *British Journal of Cancer*, the following credit line applies.
   Translated by permission from Macmillan Publishers Ltd on behalf of Cancer Research UK: [JOURNAL NAME] (reference citation), copyright (year of publication)

We are certain that all parties will benefit from this agreement and wish you the best in the use of this material. Thank you.

Special Terms:

v1.1

Questions? customercare@copyright.com or +1-855-239-3415 (toll free in the US) or +1-978-646-2777.

Gratis licenses (referencing $0 in the Total field) are free. Please retain this printable license for your reference. No payment is required.

ELSEVIER LICENSE
TERMS AND CONDITIONS

Feb 17, 2015

This is a License Agreement between Jungho Lee ("You") and Elsevier ("Elsevier") provided by Copyright Clearance Center ("CCC"). The license consists of your order details, the terms and conditions provided by Elsevier, and the payment terms and conditions.

All payments must be made in full to CCC. For payment instructions, please see information listed at the bottom of this form.

Supplier	Elsevier Limited The Boulevard,Langford Lane Kidlington,Oxford,OX5 1GB,UK
Registered Company Number	1982084
Customer name	Jungho Lee
Customer address	The University of Tokyo Tokyo, None 135-0064
License number	3563490334197
License date	Feb 07, 2015
Licensed content publisher	Elsevier
Licensed content publication	Nano Today
Licensed content title	Designing nanostructured Si anodes for high energy lithium ion batteries
Licensed content author	Hui Wu,Yi Cui
Licensed content date	October 2012
Licensed content volume number	7
Licensed content issue number	5
Number of pages	16
Start Page	414
End Page	429
Type of Use	reuse in a thesis/dissertation
Intended publisher of new work	other
Portion	figures/tables/illustrations
Number of figures/tables/illustrations	3

Format	both print and electronic
Are you the author of this Elsevier article?	No
Will you be translating?	No
Original figure numbers	figures 2,3 and table 1
Title of your thesis/dissertation	Rapid vapor deposition of micrometer-thick silicon-base porous anodes for lithium secondary batteries
Expected completion date	Mar 2015
Estimated size (number of pages)	110
Elsevier VAT number	GB 494 6272 12
Price	0.00 USD
VAT/Local Sales Tax	0.00 USD / 0.00 GBP
Total	**0.00 USD**

Terms and Conditions

INTRODUCTION

1. The publisher for this copyrighted material is Elsevier. By clicking "accept" in connection with completing this licensing transaction, you agree that the following terms and conditions apply to this transaction (along with the Billing and Payment terms and conditions established by Copyright Clearance Center, Inc. ("CCC"), at the time that you opened your Rightslink account and that are available at any time at http://myaccount.copyright.com).

GENERAL TERMS

2. Elsevier hereby grants you permission to reproduce the aforementioned material subject to the terms and conditions indicated.

3. Acknowledgement: If any part of the material to be used (for example, figures) has appeared in our publication with credit or acknowledgement to another source, permission must also be sought from that source. If such permission is not obtained then that material may not be included in your publication/copies. Suitable acknowledgement to the source must be made, either as a footnote or in a reference list at the end of your publication, as follows:

“Reprinted from Publication title, Vol /edition number, Author(s), Title of article / title of chapter, Pages No., Copyright (Year), with permission from Elsevier [OR APPLICABLE SOCIETY COPYRIGHT OWNER].” Also Lancet special credit - “Reprinted from The Lancet, Vol. number, Author(s), Title of article, Pages No., Copyright (Year), with permission from Elsevier.”

4. Reproduction of this material is confined to the purpose and/or media for which permission is hereby given.

5. Altering/Modifying Material: Not Permitted. However figures and illustrations may be altered/adapted minimally to serve your work. Any other abbreviations, additions, deletions and/or any other alterations shall be made only with prior written authorization of Elsevier Ltd. (Please contact Elsevier at permissions@elsevier.com)

6. If the permission fee for the requested use of our material is waived in this instance, please be advised that your future requests for Elsevier materials may attract a fee.

7. Reservation of Rights: Publisher reserves all rights not specifically granted in the combination of (i) the license details provided by you and accepted in the course of this licensing transaction, (ii) these terms and conditions and (iii) CCC's Billing and Payment terms and conditions.

8. License Contingent Upon Payment: While you may exercise the rights licensed immediately upon issuance of the license at the end of the licensing process for the transaction, provided that you have disclosed complete and accurate details of your proposed use, no license is finally effective unless and until full payment is received from you (either by publisher or by CCC) as provided in CCC's Billing and Payment terms and conditions. If full payment is not received on a timely basis, then any license preliminarily granted shall be deemed automatically revoked and shall be void as if never granted. Further, in the event that you breach any of these terms and conditions or any of CCC's Billing and Payment terms and conditions, the license is automatically revoked and shall be void as if never granted. Use of materials as described in a revoked license, as well as any use of the materials beyond the scope of an unrevoked license, may constitute copyright infringement and publisher reserves the right to take any and all action to protect its copyright in the materials.

9. Warranties: Publisher makes no representations or warranties with respect to the licensed material.

10. Indemnity: You hereby indemnify and agree to hold harmless publisher and CCC, and their respective officers, directors, employees and agents, from and against any and all claims arising out of your use of the licensed material other than as specifically authorized pursuant to this license.

11. No Transfer of License: This license is personal to you and may not be sublicensed, assigned, or transferred by you to any other person without publisher's written permission.

12. No Amendment Except in Writing: This license may not be amended except in a writing signed by both parties (or, in the case of publisher, by CCC on publisher's behalf).

13. Objection to Contrary Terms: Publisher hereby objects to any terms contained in any purchase order, acknowledgment, check endorsement or other writing prepared by you, which terms are inconsistent with these terms and conditions or CCC's Billing and Payment terms and conditions. These terms and conditions, together with CCC's Billing and Payment terms and conditions (which are incorporated herein), comprise the entire agreement between you and publisher (and CCC) concerning this licensing transaction. In the event of any conflict between your obligations established by these terms and conditions and those established by CCC's Billing and Payment terms and conditions, these terms and conditions shall control.

14. Revocation: Elsevier or Copyright Clearance Center may deny the permissions described in this License at their sole discretion, for any reason or no reason, with a full refund payable to you. Notice of such denial will be made using the contact information provided by you. Failure to receive such notice will not alter or invalidate the denial. In no event will Elsevier or Copyright Clearance Center be responsible or liable for any costs, expenses or damage incurred by you as a result of a denial of your permission request, other than a refund of the amount(s) paid by you to Elsevier and/or Copyright Clearance Center for denied permissions.

LIMITED LICENSE

The following terms and conditions apply only to specific license types:

15. **Translation**: This permission is granted for non-exclusive world **English** rights only unless your license was granted for translation rights. If you licensed translation rights you may only translate this content into the languages you requested. A professional translator must perform all translations and reproduce the content word for word preserving the integrity of the article. If this license is to re-use 1 or 2 figures then permission is granted for non-exclusive world rights in all languages.

16. **Posting licensed content on any Website**: The following terms and conditions apply as follows: Licensing material from an Elsevier journal: All content posted to the web site must maintain the copyright information line on the bottom of each image; A hyper-text must be included to the Homepage of the journal from which you are licensing at http://www.sciencedirect.com/science/journal/xxxxx or the Elsevier homepage for books at http://www.elsevier.com; Central Storage: This license does not include permission for a scanned version of the material to be stored in a central repository such as that provided by Heron/XanEdu.

Licensing material from an Elsevier book: A hyper-text link must be included to the Elsevier homepage athttp://www.elsevier.com . All content posted to the web site must maintain the copyright information line on the bottom of each image.

Posting licensed content on Electronic reserve: In addition to the above the following clauses are applicable: The web site must be password-protected and made available only to bona fide students registered on a relevant course. This permission is granted for 1 year only. You may obtain a new license for future website posting.

17.**For journal authors:** the following clauses are applicable in addition to the above: Permission granted is limited to the author accepted manuscript version* of your paper.

***Accepted Author Manuscript (AAM) Definition:** An accepted author manuscript (AAM) is the author's version of the manuscript of an article that has been accepted for publication and which may include any author-incorporated changes suggested through the processes of submission processing, peer review, and editor-author communications. AAMs do not include other publisher value-added contributions such as copy-editing, formatting, technical enhancements and (if relevant) pagination.

You are not allowed to download and post the published journal article (whether PDF or HTML, proof or final version), nor may you scan the printed edition to create an electronic version. A hyper-text must be included to the Homepage of the journal from which you are licensing athttp://www.sciencedirect.com/science/journal/xxxxx. As part of our normal production process, you will receive an e-mail notice when your article appears on Elsevier's online service ScienceDirect (www.sciencedirect.com). That e-mail will include the article's Digital Object Identifier (DOI). This number provides the electronic link to the published article and should be included in the posting of your personal version. We ask that you wait until you receive this e-mail and have the DOI to do any posting.

18.**Posting to a repository:** Authors may post their AAM immediately to their employer's institutional repository for internal use only and may make their manuscript publically available after the journal-specific embargo period has ended.

Please also refer to Elsevier's Article Posting Policy for further information.

19. **For book authors** the following clauses are applicable in addition to the above: Authors are permitted to place a brief summary of their work online only.. You are not allowed to download and post the published electronic version of your chapter, nor may you scan the printed edition to create an electronic version. **Posting to a repository:** Authors are permitted to post a summary of their chapter only in their institution's repository.

20. **Thesis/Dissertation**: If your license is for use in a thesis/dissertation your thesis may be submitted to your institution in either print or electronic form. Should your thesis be published commercially, please reapply for permission. These requirements include permission for the Library and Archives of Canada to supply single copies, on demand, of the complete thesis and include permission for Proquest/UMI to supply single copies, on demand, of the complete thesis. Should your thesis be published commercially, please reapply for permission.

Elsevier Open Access Terms and Conditions

Elsevier publishes Open Access articles in both its Open Access journals and via its Open Access articles option in subscription journals.

Authors publishing in an Open Access journal or who choose to make their article Open Access in an Elsevier subscription journal select one of the following Creative Commons user licenses, which define how a reader may reuse their work: Creative Commons Attribution License (CC BY), Creative Commons Attribution – Non Commercial - ShareAlike (CC BY NC SA) and Creative Commons Attribution – Non Commercial – No Derivatives (CC BY NC ND)

Terms & Conditions applicable to all Elsevier Open Access articles:

Any reuse of the article must not represent the author as endorsing the adaptation of the article nor should the article be modified in such a way as to damage the author's honour or reputation.

The author(s) must be appropriately credited.

If any part of the material to be used (for example, figures) has appeared in our publication with credit or acknowledgement to another source it is the responsibility of the user to ensure their reuse complies with the terms and conditions determined by the rights holder.

Additional Terms & Conditions applicable to each Creative Commons user license:

CC BY: You may distribute and copy the article, create extracts, abstracts, and other revised versions, adaptations or derivative works of or from an article (such as a translation), to include in a collective work (such as an anthology), to text or data mine the article, including for commercial purposes without permission from Elsevier

CC BY NC SA: For non-commercial purposes you may distribute and copy the article, create extracts, abstracts and other revised versions, adaptations or derivative works of or from an article (such as a translation), to include in a collective work (such as an anthology), to text and data mine the article and license new adaptations or creations under identical terms without permission from Elsevier

CC BY NC ND: For non-commercial purposes you may distribute and copy the article and include it in a collective work (such as an anthology), provided you do not alter or modify the article, without permission from Elsevier

Any commercial reuse of Open Access articles published with a CC BY NC SA or CC BY NC ND license requires permission from Elsevier and will be subject to a fee.

Commercial reuse includes:

- Promotional purposes (advertising or marketing)
- Commercial exploitation (e.g. a product for sale or loan)
- Systematic distribution (for a fee or free of charge)

Please refer to Elsevier's Open Access Policy for further information.

21. **Other Conditions**:

v1.7

Questions? customercare@copyright.com or +1-855-239-3415 (toll free in the US) or +1-978-646-2777.

Gratis licenses (referencing $0 in the Total field) are free. Please retain this printable license for your reference. No payment is required.

ROYAL SOCIETY OF CHEMISTRY LICENSE TERMS AND CONDITIONS

Feb 17, 2015

This is a License Agreement between Jungho Lee ("You") and Royal Society of Chemistry ("Royal Society of Chemistry") provided by Copyright Clearance Center ("CCC"). The license consists of your order details, the terms and conditions provided by Royal Society of Chemistry, and the payment terms and conditions.

All payments must be made in full to CCC. For payment instructions, please see information listed at the bottom of this form.

License Number	3563510359550
License date	Feb 07, 2015
Order Content Publisher	Royal Society of Chemistry
Order Content Publication	Energy & Environmental Science
Order Content Title	Carbon nanotubes for lithium ion batteries
Order Content Author	Brian J. Landi,Matthew J. Ganter,Cory D. Cress,Roberta A. DiLeo,Ryne P. Raffaelle
Order Content Date	Apr 9, 2009
Volume number	2
Issue number	6
Type of Use	Thesis/Dissertation
Requestor type	academic/educational
Portion	figures/tables/images
Number of figures/tables/images	2
Format	print and electronic
Distribution quantity	1
Will you be translating?	no
Order reference number	None
Title of the thesis/dissertation	Rapid vapor deposition of micrometer-thick silicon-base porous anodes for lithium secondary batteries
Expected completion date	Mar 2015
Estimated size	110
Total	**0.00 USD**

Terms and Conditions

This License Agreement is between {Requestor Name} (“You”) and The Royal Society of Chemistry (“RSC”) provided by the Copyright Clearance Center (“CCC”). The license consists of your order details, the terms and conditions provided by the Royal Society of Chemistry, and the payment terms and conditions.

RSC / TERMS AND CONDITIONS

INTRODUCTION
The publisher for this copyrighted material is The Royal Society of Chemistry. By clicking “accept” in connection with completing this licensing transaction, you agree that the following terms and conditions apply to this transaction (along with the Billing and Payment terms and conditions established by CCC, at the time that you opened your RightsLink account and that are available at any time at .

LICENSE GRANTED
The RSC hereby grants you a non-exclusive license to use the aforementioned material anywhere in the world subject to the terms and conditions indicated herein. Reproduction of the material is confined to the purpose and/or media for which permission is hereby given.

RESERVATION OF RIGHTS
The RSC reserves all rights not specifically granted in the combination of (i) the license details provided by your and accepted in the course of this licensing transaction; (ii) these terms and conditions; and (iii) CCC’s Billing and Payment terms and conditions.

REVOCATION
The RSC reserves the right to revoke this license for any reason, including, but not limited to, advertising and promotional uses of RSC content, third party usage, and incorrect source figure attribution.

THIRD-PARTY MATERIAL DISCLAIMER
If part of the material to be used (for example, a figure) has appeared in the RSC publication with credit to another source, permission must also be sought from that source. If the other source is another RSC publication these details should be included in your RightsLink request. If the other source is a third party, permission must be obtained from the third party. The RSC disclaims any responsibility for the reproduction you make of items owned by a third party.

PAYMENT OF FEE
If the permission fee for the requested material is waived in this instance, please be advised that any future requests for the reproduction of RSC materials may attract a fee.

ACKNOWLEDGEMENT
The reproduction of the licensed material must be accompanied by the following acknowledgement:

Reproduced (“Adapted” or “in part”) from {Reference Citation} (or Ref XX) with permission of The Royal Society of Chemistry.

If the licensed material is being reproduced from New Journal of Chemistry (NJC), Photochemical & Photobiological Sciences (PPS) or Physical Chemistry Chemical Physics (PCCP) you must include one of the following acknowledgements:

For figures originally published in NJC:

Reproduced (“Adapted” or “in part”) from {Reference Citation} (or Ref XX) with permission of The Royal Society of Chemistry (RSC) on behalf of the European Society for Photobiology, the European Photochemistry Association and the RSC.

For figures originally published in PPS:

Reproduced (“Adapted” or “in part”) from {Reference Citation} (or Ref XX) with permission of The Royal Society of Chemistry (RSC) on behalf of the Centre National de la Recherche Scientifique (CNRS) and the RSC.

For figures originally published in PCCP:

Reproduced (“Adapted” or “in part”) from {Reference Citation} (or Ref XX) with permission of the PCCP Owner Societies.

HYPERTEXT LINKS
With any material which is being reproduced in electronic form, you must include a hypertext link to the original RSC article on the RSC’s website. The recommended form for the hyperlink is http://dx.doi.org/10.1039/DOI suffix, for example in the link http://dx.doi.org/10.1039/b110420a the DOI suffix is ‘b110420a’. To find the relevant DOI suffix for the RSC article in question, go to the Journals section of the website and locate the article in the list of papers for the volume and issue of your specific journal. You will find the DOI suffix quoted there.

LICENSE CONTINGENT ON PAYMENT
While you may exercise the rights licensed immediately upon issuance of the license at the end of the licensing process for the transaction, provided that you have disclosed complete and accurate details of your proposed use, no license is finally effective unless and until full payment is received from you (by CCC) as provided in CCC's Billing and Payment terms and conditions. If full payment is not received on a timely basis, then any license preliminarily granted shall be deemed automatically revoked and shall be void as if never granted. Further, in the event that you breach any of these terms and conditions or any of CCC's Billing and Payment terms and conditions, the license is automatically revoked and shall be void as if never granted. Use of materials as described in a revoked license, as well as any use of the materials beyond the scope of an unrevoked license, may constitute copyright infringement and the RSC reserves the right to take any and all action to protect its copyright in the materials.

WARRANTIES
The RSC makes no representations or warranties with respect to the licensed material.

INDEMNITY
You hereby indemnify and agree to hold harmless the RSC and the CCC, and their respective officers, directors, trustees, employees and agents, from and against any and all claims arising out of your use of the licensed material other than as specifically authorized pursuant to this licence.

NO TRANSFER OF LICENSE
This license is personal to you or your publisher and may not be sublicensed, assigned, or transferred by you to any other person without the RSC's written permission.

NO AMENDMENT EXCEPT IN WRITING
This license may not be amended except in a writing signed by both parties (or, in the case of “Other Conditions, v1.2”, by CCC on the RSC's behalf).

OBJECTION TO CONTRARY TERMS
You hereby acknowledge and agree that these terms and conditions, together with CCC's Billing and Payment terms and conditions (which are incorporated herein), comprise the entire agreement between you and the RSC (and CCC) concerning this licensing transaction, to the exclusion of all other terms and conditions, written or verbal, express or implied (including any terms contained in any purchase order, acknowledgment, check endorsement or other writing prepared by you). In the event of any conflict

between your obligations established by these terms and conditions and those established by CCC's Billing and Payment terms and conditions, these terms and conditions shall control.

JURISDICTION
This license transaction shall be governed by and construed in accordance with the laws of the District of Columbia. You hereby agree to submit to the jurisdiction of the courts located in the District of Columbia for purposes of resolving any disputes that may arise in connection with this licensing transaction.

LIMITED LICENSE
The following terms and conditions apply to specific license types:

Translation
This permission is granted for non-exclusive world English rights only unless your license was granted for translation rights. If you licensed translation rights you may only translate this content into the languages you requested. A professional translator must perform all translations and reproduce the content word for word preserving the integrity of the article.

Intranet
If the licensed material is being posted on an Intranet, the Intranet is to be password-protected and made available only to bona fide students or employees only. All content posted to the Intranet must maintain the copyright information line on the bottom of each image. You must also fully reference the material and include a hypertext link as specified above.

Copies of Whole Articles
All copies of whole articles must maintain, if available, the copyright information line on the bottom of each page.

Other Conditions
v1.2

Gratis licenses (referencing $0 in the Total field) are free. Please retain this printable license for your reference. No payment is required.

If you would like to pay for this license now, please remit this license along with yourpayment made payable to "COPYRIGHT CLEARANCE CENTER" otherwise you will be invoiced within 48 hours of the license date. Payment should be in the form of a check or money order referencing your account number and this invoice number {Invoice Number}.

Once you receive your invoice for this order, you may pay your invoice by credit card.

Please follow instructions provided at that time.

Make Payment To:
Copyright Clearance Center
Dept 001
P.O. Box 843006
Boston, MA 02284-3006

For suggestions or comments regarding this order, contact Rightslink Customer Support:
customercare@copyright.com or +1-855-239-3415 (toll free in the US) or +1-978-646-2777.

Gratis licenses (referencing $0 in the Total field) are free. Please retain this printable license for your reference. No payment is required.